POLITECNICO DI MILANO

School of Industrial and Information Engineering

- **MASTER THESIS** -

in ELECTRICAL ENGINEERING

DESIGN AND MODELLING OF A MULTI-WINDING TRANSFORMER FOR ELECTRIC VEHICLE DC CHARGING STATION

Author: Supervisor:
Dejan Pejovski, 10595989   Prof. Antonino di Gerlando

Milan, October 2019

Content

List of figures

List of tables

Acknowledgment

The following work represents the final chapter of the master studies in Electrical Engineering at Politecnico di Milano. It combines the knowledge acquired during the bachelor studies at Ss. "Cyril and Methodius" University in Skopje at the Faculty of Electrical Engineering and Information Technologies on the program Power Engineering, Automation and Renewable Energy Sources, the practical experience gained during the working period in "Rade Končar – Service and Repairs of Electrical Products" Skopje and of course, the master courses at Politecnico di Milano. This thesis belongs to me as much as it belongs to any other engineering student and researcher curious to develop it further or apply it in practice. As any other research project, it is the result of hard work, devotion and sleepless nights, aimed at giving a humble contribution to the engineering world.

Many thanks to my supervisor, prof. Antonino Di Gerlando, who supported me during the past months by tracing work-paths, useful suggestions and productive discussions.

Тезава е резултат и на познанството со професорот што ми ги отвори вратите во светот на трансформаторите и на електричните машини, проф. Крсте Најденкоски. Секаква почит за вештината да пренесе знаење и љубов кон науката.

Ништо од ова не ќе беше возможно без силната поддршка од моето семејство, што секогаш веруваше во моите одлуки и безусловно стоеше крај мене, за што неизмерно им благодарам.

Особена благодардност до сите мои пријатели што низ годините ми начнуваа прашања и сомнежи и ми ја мамеа љубопитноста да ги најдам одговорите. Среќен сум што ги откривавме тајните на науката и на животот заедно.

A tutti i miei amici italiani, che mi hanno aperto un nuovo mondo e hanno creduto nelle mie capacità ancora prima di me. Grazie per avermi fatto innamorare della vostra lingua, della vostra Milano.

Sincerely,
Dejan Pejovski

Abstract

Transformers are still widely used for adjusting the voltage and current levels; one of their most recent application areas is electric vehicles (EV) dc charging stations. In order to provide charging to several vehicles simultaneously, it is possible to employ a multi-winding transformer consisting of one primary and a few separate secondary windings. In the introductory chapters of the following work, a brief summary of the transformer theory and self- and mutual inductance effects is presented and the general EV charging station system is described, emphasizing the advantages of using a multi-winding transformer. Two different topologies of ac-dc power conversion are presented: one consisting of a diode bridge rectifier and step-up/down converter and the other one of a voltage source converter operating as a boost rectifier. A comparison between them is made in terms of components choice, control complexity and waveforms quality.

The core work starts with a simple, but at the same time detailed design procedure of four- and six-coil transformers for the given application. The parameters of the equivalent network of each transformer are identified by using classical analytical approach and coils geometry as input variables. The aim of this modelling procedure is to estimate the copper and core losses in ideal sinusoidal operating conditions. After having selected one of the designs proposed, based on its characteristics and modelling ease, a more detailed analysis of the transformer performances in distorted conditions is presented. Harmonic components of the secondary and primary transformer currents are determined by Fourier analysis, and total harmonic distortion, copper and core losses, as well as transformer efficiency are estimated. Waveforms are obtained by synthesis of the Fourier components. Different pulse-width modulation techniques are analyzed in terms of switching frequency and carriers' phases; unbalanced load conditions are investigated as well. A brief temperature validation of the transformer design is done according to the relevant standards.

Keywords: electric vehicle dc charging station, multiple secondary winding, leakage inductance, self- and mutual inductances, coils disposition, harmonics content.

Sintesi

I trasformatori sono ancora ampiamente utilizzati per regolare i livelli di tensione e corrente; una delle aree di applicazione più recenti sono le stazioni di ricarica in corrente continua per veicoli elettrici (EV). Al fine di fornire la ricarica a più veicoli contemporaneamente, è possibile impiegare un trasformatore a più avvolgimenti costituito da un avvolgimento primario e alcuni avvolgimenti secondari separati. Nei capitoli introduttivi del seguente lavoro, viene presentato un breve riassunto della teoria del trasformatore e degli effetti di autoinduttanza e di induttanza reciproca e viene descritto il sistema generale di stazioni di ricarica EV, sottolineando i vantaggi dell'utilizzo di un trasformatore a più avvolgimenti. Sono presentate due diverse topologie di conversione di potenza in ca-cc: una costituita da un raddrizzatore a ponte di diodi e un convertitore step-up/down e l'altra da un convertitore di sorgente di tensione che funge da raddrizzatore boost. Viene effettuato un confronto tra loro in termini di scelta dei componenti, complessità del controllo e qualità delle forme d'onda.

Il lavoro di base inizia con una procedura di progettazione semplice ma allo stesso tempo dettagliata di trasformatori a quattro e sei avvolgimenti per la specifica applicazione. I parametri della rete equivalente di ciascun trasformatore sono identificati usando l'approccio analitico classico e la geometria degli avvolgimenti come variabili di input. Lo scopo di questa procedura di modellizzazione è stimare le perdite di rame e di ferro in condizioni operative sinusoidali ideali. Dopo aver selezionato uno dei progetti proposti, in base alle sue caratteristiche e alla facilità di modellazione, viene presentata un'analisi più dettagliata delle prestazioni del trasformatore in condizioni distorte. I componenti armonici delle correnti del trasformatore secondario e primario sono determinati dall'analisi di Fourier e vengono stimate la distorsione armonica totale e le perdite di rame e di ferro, nonché l'efficienza del trasformatore. Le forme d'onda sono ottenute per sintesi dei componenti di Fourier. Vengono analizzate diverse tecniche di modulazione della larghezza di impulso in termini di frequenza di commutazione e fasi dei portatori e vengono studiate anche le condizioni di carico sbilanciato. Viene eseguita una breve convalida della temperatura del progetto del trasformatore secondo le norme pertinenti.

Parole chiave: stazione di ricarica in corrente continua per veicoli elettrici, avvolgimento secondario multiplo, induttanza di dispersione, induttanza autonoma e reciproca, disposizione degli avvolgimenti, contenuto di armoniche.

Introduction

The transformer is a mature technical product and its story is closely linked to the beginnings of the application of electrical energy in the last decades of the 19th century. It all started with the principle of induction discovered by Faraday in 1831. He basically found out that when a changing magnetic flux links a circuit, a voltage or electromotive force is induced in that circuit. Therefore, the so called inductors were the first devices based on Faraday's principle [1]. In March 1885, the three young engineers of the Hungarian Ganz factory, Karoly Zipernowsky, Otto Balathy and Miksa Deri presented the transformer as a part of a lighting system: the energy produced by a 100 Hz ac generator was transmitted to 12 pieces of 5 kVA shell-type and 4 pieces of 7.5 kVA core-type transformers which produced 60 V secondary voltage to supply more than a thousand of Edison's incandescent lamps in parallel. The main inventions were: developing a transformer with closed iron core and low drop (the terminal voltage to be almost independent of the load), separating high voltage supply network from low voltage consumer networks, and finally, connecting consumers groups in parallel to the main line [2].

The transformer basic principles remain more or less unchanged; however there were numerous improvements of the specific design characteristics and properties. Power ratings and voltage level increased several orders of magnitude (as shown in Figure 1), while its dimensions, weight and power losses decreased dramatically. These improvements have been achieved due to the materials selection and development of advanced design tools [3], [4]:

- Core material: low loss and high magnetic saturation ($\cong 2T$) are obtained with cold rolled grain oriented steel sheets. It provides reduction in lamination thickness (up to 0.18 mm), improved grain size and orientation, surface polishing, etc. Increasing the *Si* content decreases eddy current losses and magnetostriction, i.e., the noise generated by the core. For distribution transformers up to 2.5 MVA amorphous cores are widely used.

- Conductor material: continuously transposed conductors have influenced winding design in reducing additional losses. Some of the recent innovations employ different types of superconductors, which provide much lower winding content and losses, and a higher overloading capacity; however not on a commercial scale yet. A combination of semi-conductor layer insulated with cross-linked polyethylene is experimented in dry-type transformers.

- Insulating material: cellulosic material, i.e., paper, transformer board, wood and mineral oil remain as the predominating insulation materials, due to their high reliability, long lifetime and low cost. Gas insulated transformers (SF_6 insulated transformers) are produced up to 300 MVA.

- Advanced design tools and manufacturing processes: design optimizations have been achieved by using computers and mathematical methods; field plots, transient conditions and geomagnetic disturbances can be examined more easily; however the manufacturing process generally remains to be done by skilled workers, because automatic core stacking and winding processes have high parameters variety and low repetition rate.
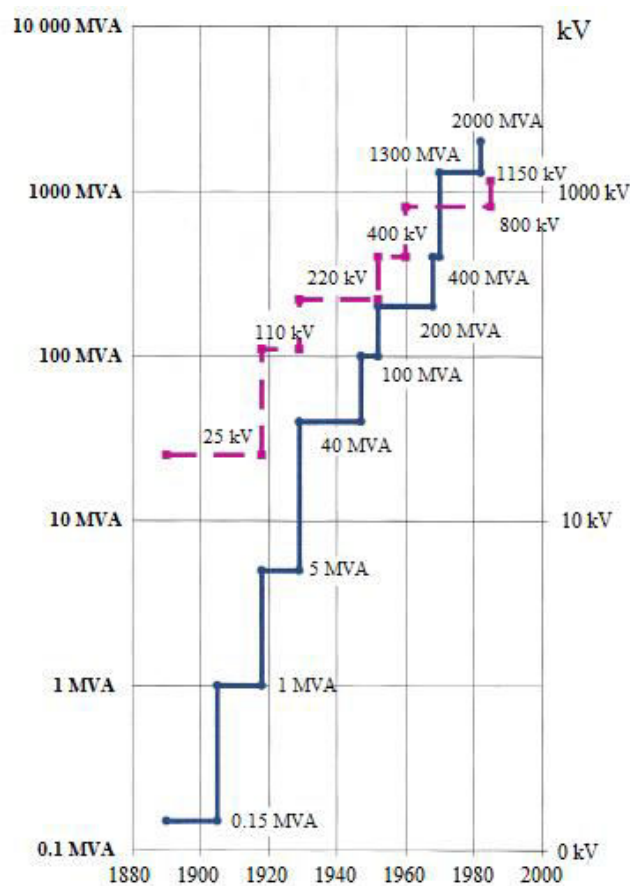
Figure 1 Development of transformer rated voltage and power [3]

Europe transformer market size in 2017 was valued 45 billion euro; more than 985 million euro of them belongs to oil filled distribution transformers. The anticipated installation of all types of transformers by 2024 in Europe is expected to exceed 6 million units annually: 2 million of them will be installed indoors; 200 thousand are estimated to be oil filled distribution transformers [5].

1 Basic transformer theory

1.1 Ideal transformer operation

A transformer is a static device which consists of two or more electric circuits (windings) coupled by a common magnetic circuit. If one of these windings, so called primary, is connected to an alternating-voltage source, an alternating flux will be produced which links the other winding, so called secondary, and will induce a voltage in it. By suitably choosing the number of primary and secondary turns which form the windings, almost any desired voltage ratio can be achieved by the transformer [6]. According to the basic law of energy conservation, the power transferred between the electric circuits remains unchanged, except for a loss in the process.

To simplify the transformer analysis, a common representation assumes separation of the primary and secondary windings, as if they were wound on separate legs of the core, as shown in Figure 2. Applying an alternating voltage v_1 to the terminals of the primary winding and assuming open secondary winding (S open), a small steady-state current i, called exciting current, flows in the primary winding and establishes an alternating flux in the magnetic circuit. This flux induces an electromotive force (emf) e_1 in the primary equal to:

$$e_1 = \frac{d\Phi_{11}}{dt} = N_1 \frac{d\varphi}{dt},$$

(1)

where Φ_{11} is the flux linkage of the primary winding, φ is the flux in the core linking both windings and N_1 is the number of turns in the primary winding.
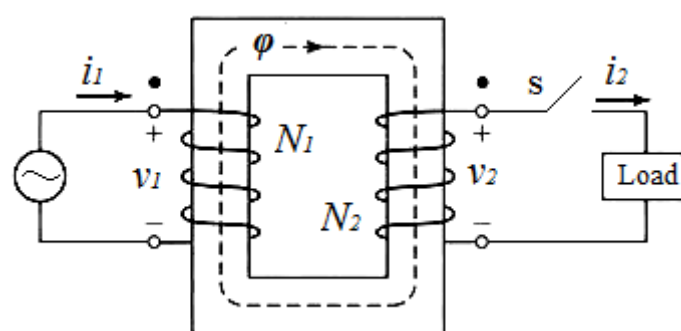
Figure 2 Ideal transformer and load

As a first approximation, the properties of the transformer can be idealized under the following assumptions [7]:

- Winding resistances are negligible, i.e., the conductors have a perfect conductivity and therefore there are no Joule losses on the windings;

- All the flux is confined to the core and links both windings, i.e., the ideal coupling exists between the windings and the leakage flux is zero;

- No losses in the core; its permeability is so high that only a negligible exciting magnetomotive force (mmf) is required to establish the flux;

- No capacitances are incorporated in the windings;

- The core exhibits linear magnetic characteristics (constant permeability).

Under these assumptions, when a time-varying voltage v_1 is applied on the primary terminals, a core flux φ must be established such that the counter emf e_1 equals the impressed voltage:

$$v_1 = e_1 = N_1 \frac{d\varphi}{dt} \ . \tag{2}$$

The core flux also links the secondary winding and produces an induced emf e_2, and an equal secondary terminal voltage v_2, given by:

$$v_2 = e_2 = N_2 \frac{d\varphi}{dt}. \tag{3}$$

From the ratio of Eq. (2) and (3), it follows that an ideal transformer is a device which transforms voltages in the direct ratio of the number of turns in its windings:

$$\frac{v_1}{v_2} = \frac{N_1}{N_2} \ . \tag{4}$$

Now let a load be connected to the secondary (S closed). A current i_2 and an mmf $N_2.i_2$ are present in the secondary. Under the hypotheses of the ideal transformer, the core flux is unchanged by the presence of the load on the secondary; the net mmf acting on the core will not change and therefore it remains negligible:

$$N_1 i_1 - N_2 i_2 = 0. \tag{5}$$

From the Eq. (5) it becomes evident that a compensating primary mmf must result in order to cancel that of the secondary. Since the net mmf remains unchanged, any change in the mmf flowing in the secondary as the result of a load must be accompanied by a corresponding change in the primary mmf. For the reference current directions shown in Figure 2, the mmfs of the primary and secondary currents compensate. The net mmf acting on the core is therefore zero, in accordance with the assumption that the exciting current of an ideal transformer is zero.

From Eq. (5) it follows that:

$$\frac{i_1}{i_2} = \frac{N_2}{N_1}.$$ (6)

Thus combining Eq. (4) and (6), it can be noted that the instantaneous power input to the primary equals the instantaneous power output from the secondary; it is a reasonable conclusion since all dissipative and energy storage mechanisms in the transformer have been neglected.

In large transformers, typically the waveforms of the voltage and flux are nearly sinusoidal. The instantaneous flux is given by:

$$\varphi(t) = \Phi_{max} \sin \omega t ,$$ (7)

where Φ_{max} is the maximum value of the flux and $\omega = 2\pi f$ is the angular frequency.

The induced primary voltage is:

$$e_1(t) = N_1 \frac{d\varphi}{dt} = \omega N_1 \Phi_{max} \cos \omega t .$$ (8)

For the current and voltage reference directions shown in Figure 2, the induced emf leads the flux by 90°. The rms value of the induced emf e_1 is:

$$E_{1,rms} = \frac{2\pi}{\sqrt{2}} f N_1 \Phi_{max} = \sqrt{2} \pi f N_1 \Phi_{max} = 4.44 f N_1 \Phi_{max} .$$ (9)

1.2   Real transformer operation

Removing the assumptions imposed on the ideal transformer, a more detailed model must take into account the effects of winding resistances, leakage fluxes, and finite exciting current due to the finite (and nonlinear) permeability of the core. In transient conditions or high frequency operation, the capacitances of the windings have to be included too. Starting from the transformer ideal behaviour, it is usually possible to establish an equivalent circuit based on physical reasoning. In this chapter, the analysis will be continued for a two-winding transformer, aimed at completing the basic transformer theory and at helping in understanding the preceding work. Multi-winding transformers and equivalent circuits will be presented in details in the following chapters.

Considering the resistance of the conductors forming the windings is significant because it generates Joule losses during transformer operation and increases the internal temperature. The voltage drops caused by windings resistances can be expressed as:

$$e_{r1} = R_1 i_1; \quad e_{r2} = R_2 i_2. \tag{10}$$

The total flux linking the primary winding consists of two components [6]:

- Resultant mutual flux, confined essentially to the iron core and produced by the combined effect of the primary and secondary currents, and

- Primary leakage flux, which links only the primary winding.

These components are identified on Figure 3. The leakage flux induces voltage in the primary winding which adds to that produced by the mutual flux. Because the leakage path is primarily in the air, this flux and the voltage induced by it vary linearly with primary current i_1. It can be therefore represented by a primary leakage inductance $L_{\sigma 1}$ and the corresponding primary leakage reactance $X_{\sigma 1}$ is given as:

$$X_{\sigma 1} = 2\pi f L_{\sigma 1}. \tag{11}$$

Voltage drops caused by the leakage inductance are expressed as:

$$e_{\sigma 1} = L_{\sigma 1} \frac{di_1}{dt}; \quad e_{\sigma 2} = L_{\sigma 2} \frac{di_2}{dt}. \tag{12}$$
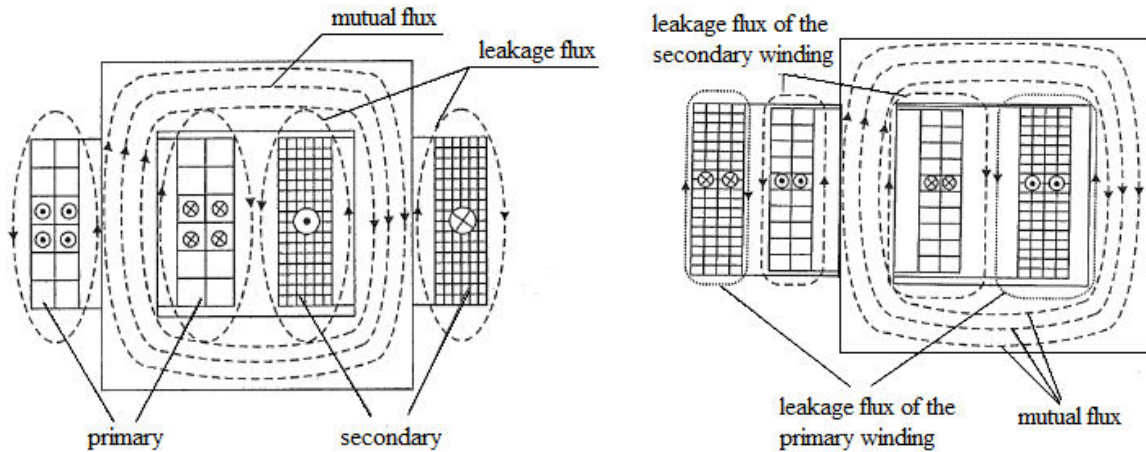
Figure 3 Transformer leakage field (simplified and realistic approach)

Now it becomes evident that the primary terminal voltage consists of three components: voltage drops on the primary resistance, voltage drop arising from primary leakage flux and the emf induced in the primary winding by the resultant mutual flux, which are shown in Figure 4. The same reasoning is valid for the secondary winding too.
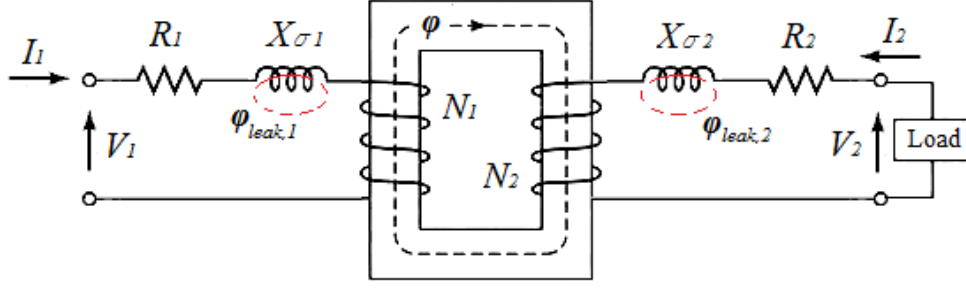
Figure 4 Non-ideal transformer and load

It should be put in evidence that adopting a secondary current direction exiting the winding towards the load, as shown in Figure 2, corresponds to the real conditions when the transformer supplies the load. On the other hand, current entering the secondary winding highlights the fact that the flux it generates opposes the one generated by the primary winding. When both windings are placed on the same column, they should be wound in opposite direction in order to cancel out the fluxes they generate in the core. In the following chapters this argument will be developed further, relating it to the self- and mutual inductances.

1.3 Two-winding transformer equivalent circuit

In order to simplify the transformer analyses it is a common practice to assume that both the windings have the same number of turns ($N_2' = N_1$). Therefore, all the parameters of one transformer side should be referred to the other one, by using the transformer ratio. Usually as a reference side is taken to be the one which is supplied by energy; however, the power balance of the original transformer and the referred one cannot be varied. The following equivalences are adopted:

- Under the condition of invariable magnetomotive force, the secondary current referred to the primary winding can be calculated as:

$$I_2 N_2 = I_2' N_2' \implies I_2' = I_2 \frac{N_2}{N_2'} = I_2 \frac{N_2}{N_1} = \frac{1}{k_{12}} I_2. \tag{13}$$

- Imposing a condition on the invariable total apparent power, the induced emf can be referred to the primary winding:

$$E_2 \cdot I_2 = E_2' \cdot I_2' \implies E_2' = E_2 \cdot \frac{I_2}{I_2'} = E_2 \cdot \frac{N_1}{N_2} = k_{12} \cdot E_2. \tag{14}$$

- From the power losses invariance, the referred impedance values can be calculated:

$$R_2 \cdot I_2^2 = R_2 \cdot I_2^{'2} \implies R_2^{'} = r_2 \left(\frac{I_2}{I_2^{'}} \right)^2 = R_2 \cdot k_{12}^2 ;$$

$$X_2^{'} = X_2 \cdot k_{12}^2 ; \quad X_{\sigma 2}^{'} = X_{\sigma 2} \cdot k_{12}^2 ; \quad Z_2^{'} = R_2^{'} + jX_2^{'}$$

(15)

It is also convenient to remove the magnetic circuit from Figure 4 and represent all the components in a single electrical circuit. This can be done by the following steps, which are also shown in Figure 5 [8]:

- Both actual windings are replaced by two partial windings: an ideal one, wound on the column and without any losses, and the other one has an impedance consisting of active and reactive components;

- The two ideal windings placed on the core legs have the same number of turns; they are therefore linked by the same flux and can be represented as an equivalent single winding in which the magnetizing current flows;

- This equivalent winding consists of a mutual inductance L_m, also known as magnetizing inductance in two-winding transformers (since it links the mutual magnetic flux) whose reactance is given by:

$$X_m = 2\pi f L_m .$$

(16)

- The magnetizing (excitation) branch is identified, which consists of active and reactive impedance components, such that the induced emf E_1 can be determined as:

$$E_1 = Z_m \cdot I_0 = (R_m + jX_m) \cdot I_0 .$$

(17)

It has to be noted that the parameters of the magnetizing branch (R_m and X_m) do not have a physical meaning; they are only representations for the phenomena occurring in the magnetic circuit, i.e., with the active component R_m the power losses in the core can be represented, and the reactive component X_m is an equivalent of the power losses due to the magnetizing of the core.

When R_m is assumed constant, the core loss is therefore assumed to vary as E_1^2 or as Φ_{max}^2. When X_m is assumed constant, the magnetizing current is thereby assumed to be independent of frequency and directly proportional to the resultant mutual flux. Both R_m and X_m are usually determined at rated voltage and frequency; they are then assumed to remain constant for the small variations of the rated values associated with normal operation.
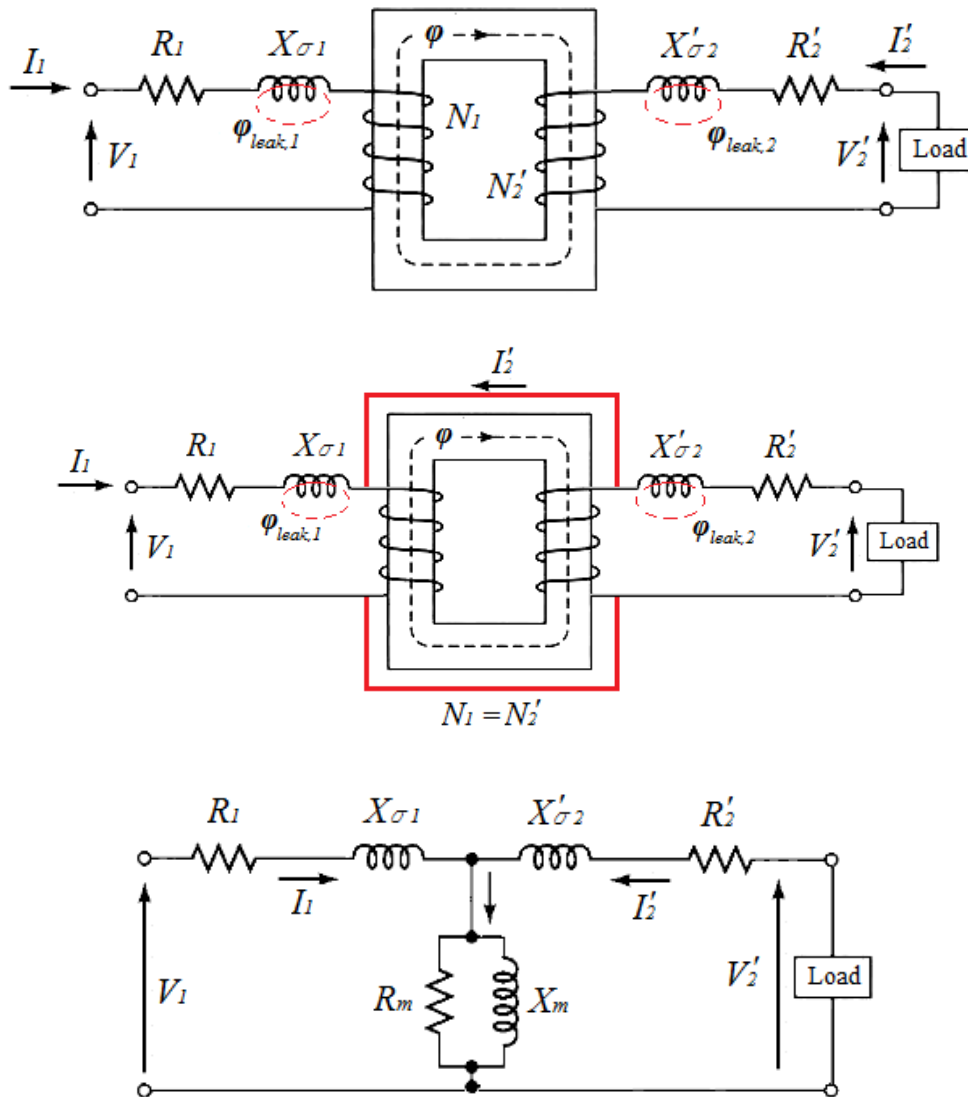
Figure 5 Derivation of the transformer equivalent circuit: a) referring the parameters to the primary side; b) transition from two ideal to one equivalent winding; c) T-equivalent circuit

1.4 Transformer leakage field: origin and effects

As a leakage field of a single winding is considered the part of the magnetic flux which is not linked with the other windings. In the presence of iron core, this definition is sometimes varied as: the flux whose lines do not follow entirely the path inside the iron core; therefore the origin of its name "leakage field". It can be claimed that the leakage fields are confined in the air hollows of the transformer, including the volume occupied by the windings, insulation etc., as shown in Figure 6 [9].

The leakage field due to the load current effectively results in impedance between the windings, known as leakage reactance. The magnitude of this reactance is a function of the number of turns in the windings, the winding currents, leakage field and the geometry of the

core and windings, as it will be shown later. Its magnitude usually ranges from 4% to 20% of the base transformer rating [10].
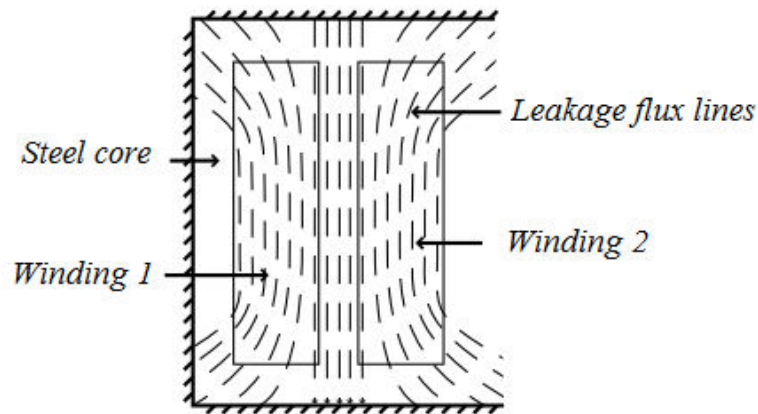
Figure 6 Leakage flux fields

The transformer's leakage field is particularly significant, because it affects primarily the following quantities [9]:

- Leakage reactance, and therefore, the short-circuit current and voltage drop, i.e., secondary voltage variation occurs in normal operation;

- Electromagnetic forces on the windings, especially in fault conditions;

- Increase in winding resistance due to skin-effect, and therefore increase in copper losses and winding temperatures;

- Inducing currents in the constructional parts which increase the additional losses in non-active components and increase in the temperature of these components.

It should be noted that since the leakage flux travels through empty space (or insulation paper, mineral oil, etc.) instead of through iron, there is no hysteresis or saturation and the permeability in this region is constant and equal to μ_o. The leakage flux is in phase with, and is directly proportional to the load current [11]:

$$\varphi_{leak} \propto B_{leak} = \mu_o H_{leak} \propto I_{load}. \tag{18}$$

As the magnitude of the leakage flux increases, the magnitude of the flux in the core decreases. The voltage drop on the secondary winding terminals is directly proportional to the rate of change of the load current [11]:

$$\Delta E_2 = E_s - E_s^{'} = \frac{d\varphi_{leak}}{dt} \propto dI_{load} \ , \tag{19}$$

where E_s is the secondary voltage assuming no leakage flux exists, $E_s^{'}$ is the secondary voltage with leakage flux.

The relationship between the load current and secondary voltage is equivalent to placing physical impedance in series with the output of an ideal transformer. This is called the leakage reactance because it is an external manifestation of the effect of the leakage flux on the secondary voltage.

1.5 Two-winding transformer leakage reactance calculation

In defining the leakage reactance it is useful to identify the total leakage field: it is the field generated by the magnetomotive forces whose sum equals zero. Although it might seem as a paradox statement, the phenomenon can be easily explained. Removing the assumption on the null magnetizing current, in the actual transformers the sum of the mmfs of the windings equals the magnetizing mmf:

$$N_1 \cdot i_1 - N_2 \cdot i_2 = N_1 \cdot i_\mu \ , \Rightarrow \ N_1 \cdot (i_1 - i_\mu) = N_2 \cdot i_2$$

$$N_1 \cdot i_1^{'} - N_2 \cdot i_2 = 0 \ , \tag{20}$$

where $i_1^{'}$ is the component of the primary current which appears as a result of the load current, i.e., it is the increase of the magnetizing current i_μ which flows in the primary winding in no load conditions, up to the value i_1 which corresponds to a load current i_2.

At no load conditions, only the current $i_1 = i_\mu$ flows in the primary windings and it generates the main core flux φ. At load conditions, this flux remains practically unchanged and it is still generated by the magnetizing current. However, the primary current increases for a value $i_1^{'}$, and leakage flux appears. It is obvious that both the currents i_1 and i_2 generate the leakage flux, and according to Eq. (20) their total mmf equals zero. It is also evident that the magnetic flux which generates this null mmf cannot have paths which link both the windings; it has to contain paths which close intersecting one winding only.

Therefore, in calculation of the leakage flux and self- and mutual inductance only the air hollow can be considered, and that in the primary and secondary windings currents are generating mmfs which are equal in amplitude and have opposite directions.

The self- and mutual inductance depend on the shape, dimensions and disposition of the transformer windings. An example will be shown for the simplest case of two concentric windings with equal heights, as shown in Figure 7. Applying the Ampere's law:

$$\oint \overline{H} \cdot d\overline{l} = \sum N \cdot i \, . \tag{21}$$

The magnetomotive force value of the winding 1 starts from zero and increases linearly until the radial dimension reaches the external edge of the winding $(D_1 + a_1)$; as the radial distance increases, the flux tubes link larger number of turns. Assuming the numbers of turns are equal, $N_1=N_2$, it means that the currents are also equal: $I_1=I_2=I_n$ and they flow in opposite directions. This implies that the magnetomotive force of the winding 2 linearly decreases from distance $(D_2 - b)$ to D_2.
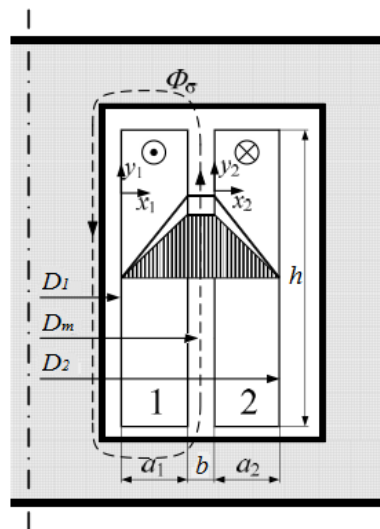
Figure 7 Two winding transformer leakage fluxes

Considering both the windings together, the total leakage field and total self-inductance can be obtained as $L_{\sigma1}+ L_{\sigma2}$: separating them may be slightly more complex. Therefore the primary and secondary winding can be viewed as a single winding with N number of turns and current I, without taking into account the core flux (as shown in Figure 8):
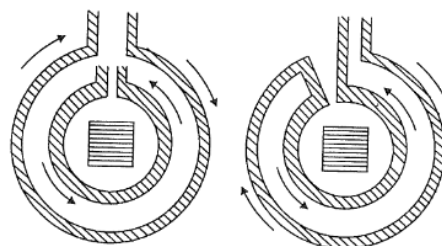
Figure 8 Equivalent winding obtained by connecting the primary and secondary windings (both referred to the same number or turns N)

According to the Figure 9, the following proportions for the left and the right branch can be established:

$$\frac{B}{x} = \frac{B_{max}}{a_1} \quad \Rightarrow \quad B = \frac{B_{max}}{a_1} x. \tag{22}$$

$$\frac{B}{a_1 + b + a_2 - x} = \frac{B_{max}}{a_2} \quad \Rightarrow \quad B = \frac{B_{max}}{a_2}\left(a_1 + b + a_2 - x\right). \tag{23}$$
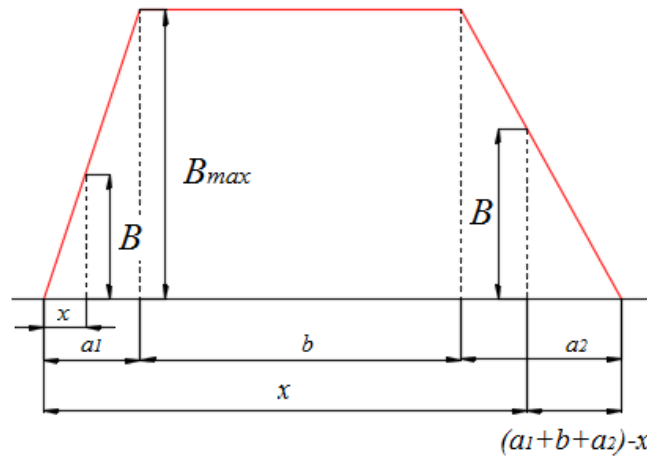
Figure 9 Flux density distribution in one half of the transformer window

The maximum flux density in the hollow can be calculated as:

$$H_{max} h^{'} = N \cdot I = \frac{B_{max}}{\mu_o} h^{'} \quad \Rightarrow \quad B_{max} = \mu_o \cdot \frac{N \cdot I}{h^{'}}. \tag{24}$$

In order to calculate the total short-circuit reactance, which is given by Eq. (25) we can start from the magnetic field energy. For an instantaneous current value i, the corresponding energy is given by Eq. (26).

$$X_k = \omega \cdot L_k = \omega \cdot \left(L_{\sigma 1} + L_{\sigma 1}\right). \tag{25}$$

$$w = \frac{1}{2} L_k i^2. \tag{26}$$

Using the root mean square value of the current, it can be written:

$$I_m = \sqrt{2} I \quad \Rightarrow \quad W_m = \frac{1}{2}\frac{X_k}{\omega} I_m^2. \tag{27}$$

$$X_k = \frac{\omega W_m}{I^2}. \tag{28}$$

The total energy of the leakage field can be calculated as:

$$W_m = \frac{1}{2} \int_V B_{\max} H_{\max} dV = \frac{1}{2\mu_o} \int_V B_m^2 dV . \tag{29}$$

This energy is stored in the volume consisting of three parts:

- In the air hollow with radial length b, the flux density is constant and equal to its maximum value, thus the volume is $V = \pi \cdot D_m \cdot b \cdot h^{'}$ and the energy stored in the leakage field is:

$$W_{gap} = \frac{1}{2\mu_o} \mu_o^2 \frac{N^2 I_m^2}{h^{'2}} \pi D_m b h^{'} = \frac{\mu_o}{h^{'}} (NI)^2 \pi D_m b . \tag{30}$$

- In the volume occupied by the winding 1 the flux density on a distance x is:

$$B_x = B_m \frac{x}{a_1} = \mu_o \frac{NI_m}{h^{'}} \frac{x}{a_1} . \tag{31}$$

Taking into account the elementary volume $dV = \pi(D_1 + 2x)h^{'} dx$, the energy stored in this part is:

$$W_{a1} = \frac{1}{2\mu_o} \int_0^{a_1} B_x^2 \pi(D_1 + 2x)h^{'} dx = \frac{\mu_o \pi}{h^{'}} (NI)^2 a_1 \left(\frac{D_1}{3} + \frac{a_1}{2} \right) \approx \frac{\mu_o}{h^{'}} (NI)^2 \pi \frac{D_m a_1}{3} . \tag{32}$$

- In the analogue way, the energy stored in the volume occupied by the winding 2 is:

$$W_{a2} \approx \frac{\mu_o}{h^{'}} (NI)^2 \pi \frac{D_m a_2}{3} . \tag{33}$$

The total energy of the leakage field is a sum of these three components:

$$W_m = W_{gap} + W_{a1} + W_{a2} = \mu_o \pi N^2 \frac{D_m}{h^{'}} \left(\frac{a_1}{3} + b + \frac{a_2}{3} \right) I^2 . \tag{34}$$

The flux lines do not cross the air hollow in straight lines, but rather shrink at the top and the bottom of each winding: an effect known as fringing which causes increase in the losses in the neighbouring conductors. This fringing of the leakage flux field is a function of the windings geometry and can be evaluated by resorting to magnetic field plotting using finite element analysis tools [12]. In practice, a useful rule of thumb can be applied: assuming the windings have equal axial lengths $h_1 = h_2 = h$, an equivalent height $h^{'}$ can be used instead, which is related to h through the Rogowski coefficient [9]:

$$k_R = 1 - \frac{a_1 + b + a_2}{\pi h} , \tag{35}$$

where $h^{'} = h/k_R$. Taking into account the Eq. (28) and (34), the leakage reactance can be expressed as:

$$X_k = \frac{\omega W_m}{I^2} = \omega\mu_o\pi\frac{D_m k_R}{h}\left(\frac{a_1}{3} + b + \frac{a_2}{3}\right)N^2 = \omega\mu_o\pi\frac{D_m k_R}{h}cN^2 , \qquad (36)$$

where c is the distance between the windings electromagnetic centres; it can be regarded as the distance at which the two windings (with assumed infinitesimal radial thickness) should be positioned in order to store the same total leakage energy as the actual windings.

The load current causes a considerable voltage drop across this reactance. The ratio between the reactance voltage drop and the winding voltage, multiplied by 100, is known as percent reactance. It can be calculated taking into account the number of turns, the magnitudes of the current and the leakage field, and the transformer geometry, or it can be measured by short-circuit test. One of the windings is short-circuited, and the voltage supplying the other winding is increased until rated current flows in the windings. This voltage divided by the rated winding voltage times 100 is the percent reactance voltage or percent reactance [10].

Leakage reactance limits short-circuit currents, and is therefore useful, but it also reduces the secondary voltage under load and consumes reactive power. Varying the winding dimensions and the spacing between them, the value of the leakage reactance can be controlled. For example, if the spaces between the windings are kept small, there will be fewer flux lines contained in these spaces and the leakage reactance will be small.

1.6   Self- and mutual inductances identification

Considering a single coil with N turns wound around a magnetic core, when current i flows through the coil it generates total magnetic flux Ψ whose lines enclose all the turns N. The ratio between total flux linked and the current in the coil is called self-inductance L:

$$L = \frac{\Psi}{i} = \frac{N\Phi}{i} = \frac{N^2}{\Re} = \frac{N^2\mu_r\mu_0 S_{fe}}{l} , \qquad (37)$$

where $\Re$ is the magnetic reluctance of the flux path, Φ is the flux per turn, l is the average length of the flux path, S_{fe} is the area of the core cross section and μ_r is the relative permeability of the material.

The value of the self-inductance is mostly dependent on the number of turns in the coil and the magnetic characteristics of the material which the magnetic field goes through. For a

constant value of the current, the higher the self-inductance, the higher the flux linked with the coil.

In linear magnetic circuits the permeability does not depend on the magnetic flux density; therefore the induced voltage can be written as:

$$e = -\frac{d\Psi}{dt} = -\frac{d(Li)}{dt} = -L\frac{di}{dt} - i\frac{dL}{dt}.$$
(38)

If the inductance can be considered constant, which means that magnetic core saturation is not taken into account, the Eq. (38) can be rewritten as:

$$e = -L\frac{di}{dt}.$$
(39)

In non-linear magnetic circuits, considering the magnetizing curve $\Psi(i)$ curve shown in Figure 10, it is suitable to write:

$$e = -\frac{d\Psi}{dt} = -\frac{d\Psi}{di} \cdot \frac{di}{dt},$$
(40)

where the first multiplier is so called differential inductance L_d, which is used for calculating the induced voltage. In linear magnetic circuits, L_d equals the self-inductance L calculated as a ratio between the total flux and the current.
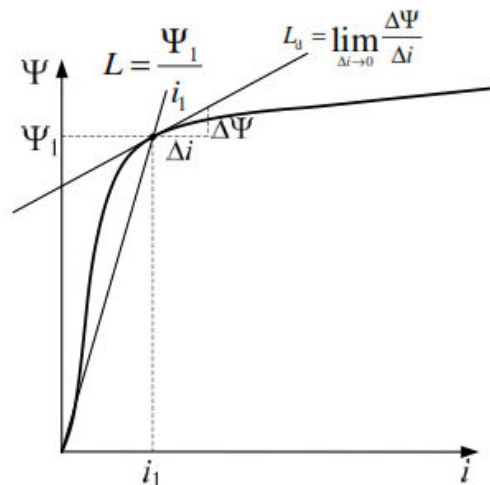
Figure 10 Magnetizing curve for non-linear magnetic material [13]

Referring the aforementioned considerations for the inductance to a two-winding transformer, the mutual inductances can be calculated: they define the relationship between the current flowing through one coil and the flux linking the other coil placed on the same magnetic core:

$$L_{21} = \frac{\Psi_{21}}{i_1} = N_2 \frac{\Phi_{21}}{i_1} = N_2 k_1 \frac{\Phi_1}{i_1} = N_2 k_1 \frac{N_1 i_1}{i_1 \mathfrak{R}_1} = k_1 \frac{N_1 N_2}{\mathfrak{R}_1} , \tag{41}$$

where Ψ_{21} is the total flux generated by i_1 and enclosed by N_2 turns, Φ_{21} is the flux per turn generated by current in coil 1 and constrained in the magnetic core, k_1 is the linking coefficient of coil 1 and $\mathfrak{R}_1$ is the magnetic reluctance of the flux path to the field generated by i_1. The flux per turn created by the current i_1 is a sum of main (Φ_{21}) and leakage component ($\Phi_{1\sigma}$):

$$\Phi_1 = \Phi_{1\sigma} + \Phi_{21} . \tag{42}$$

Similar observations are valid for the situation when coil 2 is supplied by current and coil 1 is open:

$$L_{12} = \frac{\Psi_{12}}{i_2} = N_1 \frac{\Phi_{12}}{i_2} = N_1 k_2 \frac{\Phi_2}{i_2} = N_1 k_2 \frac{N_2 i_2}{i_2 \mathfrak{R}_2} = k_2 \frac{N_1 N_2}{\mathfrak{R}_2} . \tag{43}$$

$$\Phi_2 = \Phi_{2\sigma} + \Phi_{12} . \tag{44}$$

It has to be highlighted that $L_{12} = L_{21}$ because they depend on the common (main) flux which links both the coils, regardless of which one generates the flux. In case of non-linear magnetic core, mutual inductances are equal only if they are calculated in conditions of the same magnetic saturation.

The linking coefficient of each winding is defined as the ratio between the component of the flux whose lines close inside the magnetic core only and the one which closes through air:

$$k_1 = \frac{\Phi_{21}}{\Phi_1}; \quad k_2 = \frac{\Phi_{12}}{\Phi_2} . \tag{45}$$

The coils self-inductances according to (35) are defined as:

$$L_{11} = \frac{\Psi_1}{i_1} = N_1 \frac{\Phi_1}{i_1} = \frac{N_1^2}{\mathfrak{R}_1} , \tag{46}$$

$$L_{22} = \frac{\Psi_2}{i_2} = N_2 \frac{\Phi_2}{i_2} = \frac{N_2^2}{\mathfrak{R}_2} , \tag{47}$$

Combining the previous expressions, the relationship between self- and mutual inductances can be obtained as:

$$L_{12}L_{21} = L_{12}^2 = k_1 k_2 L_{11} L_{22}.$$ (48)

$$L_{12} = \sqrt{k_1 k_2} \sqrt{L_{11} L_{22}} = k\sqrt{L_{11} L_{22}}.$$ (49)

In the case when currents flow through both the coils, the total linkage fluxes depend on the self- and mutual inductances and the currents, thus the expressions which relate them are:

$$\Psi_1 = L_{11}i_1 \pm L_{12}i_2.$$ (50)

$$\Psi_2 = L_{22}i_2 \pm L_{12}i_1.$$ (51)

The flux linked due to mutual inductance can have the same or the opposite direction of the flux due to the self-inductance. The sign of the mutual inductance depends on the current direction and the coil wounding direction, as shown in Figure 11 :

$$\Psi_1 = L_{11}i_1 + L_{12}i_2; \quad \Psi_2 = L_{22}i_2 + L_{12}i_1 \qquad \Psi_1 = L_{11}i_1 - L_{12}i_2; \quad \Psi_2 = L_{22}i_2 - L_{12}i_1$$
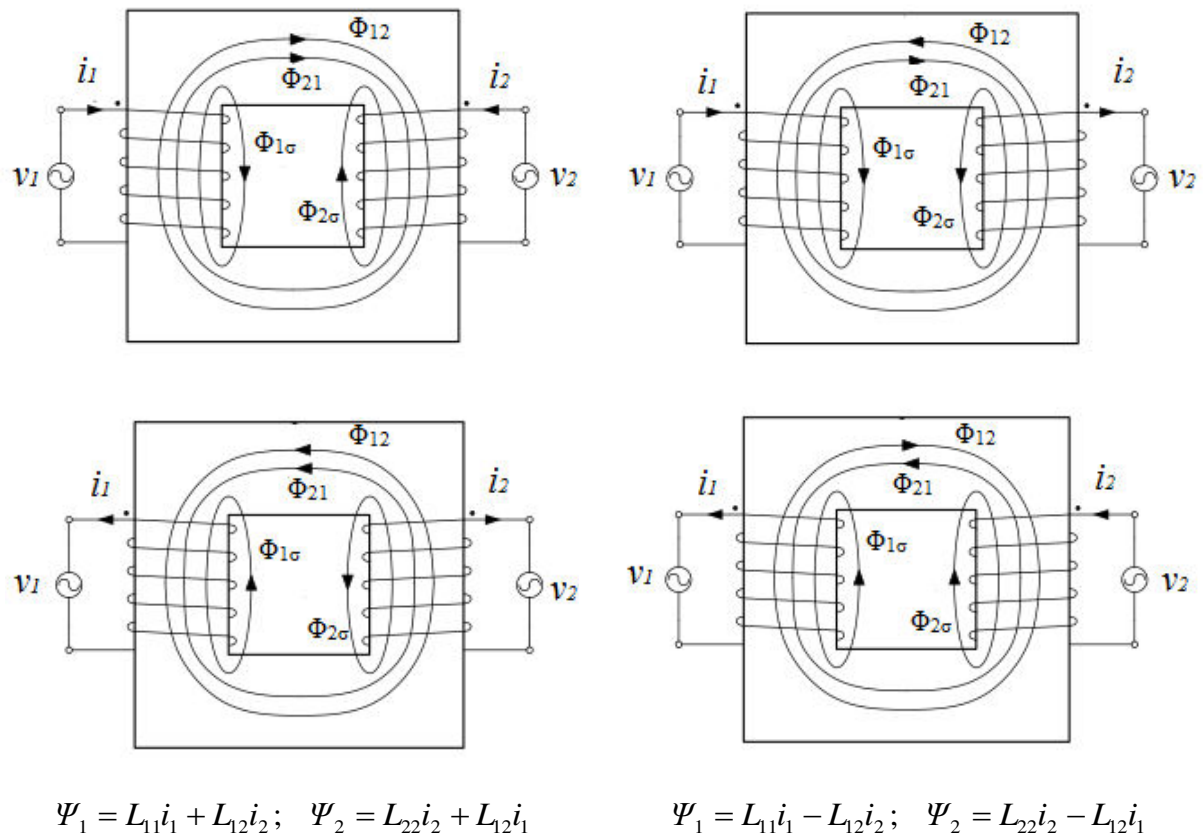
Figure 11 Convention for mutual inductance sign [13]

Considering a secondary current flowing to the load, terminal voltages can be written taking into account the active and reactive voltage drops as:

$$v_1 = R_1 i_1 + \frac{d\Psi_1}{dt} = R_1 i_1 + L_{11}\frac{di_1}{dt} - L_{12}\frac{di_2}{dt}.$$ (52)

$$-v_2 = R_2 i_2 + \frac{d\Psi_2}{dt} = R_2 i_2 + L_{22} \frac{di_2}{dt} - L_{12} \frac{di_1}{dt} . \tag{53}$$

In sinusoidal steady state and after some mathematical rearrangements, the same equations can be written as follows, emphasizing the leakage inductances $L_{\sigma 1}$ and $L_{\sigma 1}$:

$$\overline{V_1} = R_1 \overline{I_1} + j\omega\left(L_{11} - L_{12}\right)\overline{I_1} + j\omega L_{12}\left(\overline{I_1} - \overline{I_2}\right). \tag{54}$$

$$-\overline{V_2} = R_2 \overline{I_2} + j\omega\left(L_{22} - L_{12}\right)\overline{I_2} - j\omega L_{12}\left(\overline{I_1} - \overline{I_2}\right). \tag{55}$$

$$L_{\sigma 1} = L_{11} - \frac{N_1}{N_2} L_{12}; \quad L_{\sigma 2} = L_{22} - \frac{N_2}{N_1} L_{12}. \tag{56}$$

2   Multi-winding transformers: basic considerations

2.1   Introduction to multi-winding transformers and equivalent diagram

Multi-circuit transformers consist of three or more windings which interconnect different voltage ratings. The same aim can be achieved by a few two-winding transformers, at increased costs and reduced efficiency of the system. Several of the obvious situations which require a multi-circuit transformer are [14]:

- Feeding a distribution system from two or more transmission circuits of different voltages;

- Generating system which feeds two or more outgoing transmission circuits of different voltages;

- Supplying an auxiliary load at a voltage different from that of either the primary or secondary voltage;

- The need to subdivide the load into two or more separate secondary windings for the purpose of reducing the short-circuit power due to faults;

- Autotransformers with tertiary winding, etc.

Some of the advantages of multi-winding transformer applications are [10]:

- Interconnection of several power systems operating at different voltages;

- Control of voltage regulation and reactive power;

- Electrical isolation of secondary circuits.

An important aspect of the multi-winding transformers is the leakage inductance, because it has a significant effect on voltage regulation, load division between the windings, parallel operation with other transformers, short-circuit characteristics, efficiency, etc. All the windings are magnetically coupled to the main flux and are affected by the loading of the other windings. It is necessary to have a clear conception of the leakage impedance relationships; otherwise the manipulation of the parameters may be very complex [15]. Therefore, it becomes clear that windings arrangement is of crucial importance in transformer operation because it actually determines the leakage reactance between the winding pairs.

The equivalent single-line diagram of a multi-winding transformer consists of a pair or primary terminals, at which the active power is supplied to the transformer, and a set of

output windings: secondary, tertiary, etc., as shown in Figure 12. The diagram contains the magnetizing admittance element placed at the input terminals, which may be left out for simplifying purposes. Ideal transformers representing the no-load turns ratios between different windings are connected to the linear network of series impedances which for an n-winding transformer contains $n(n\text{-}1)/2$ independent elements [16].
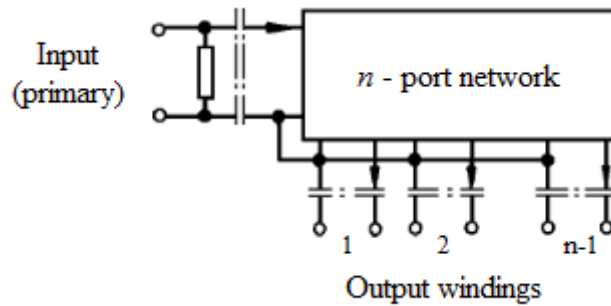
Figure 12 Single-line equivalent diagram of multi-winding transformer

2.2 Four-winding transformer equivalent network

Starting the discussion on the equivalent network of multi-circuit transformers, it has to be highlighted that only three-winding transformers may be represented both as a star and as a mesh network (Figure 13). The three-winding transformer has three independent leakage impedances among its circuits; therefore a three-terminal network in either star or mesh connection is suitable as an equivalent circuit.
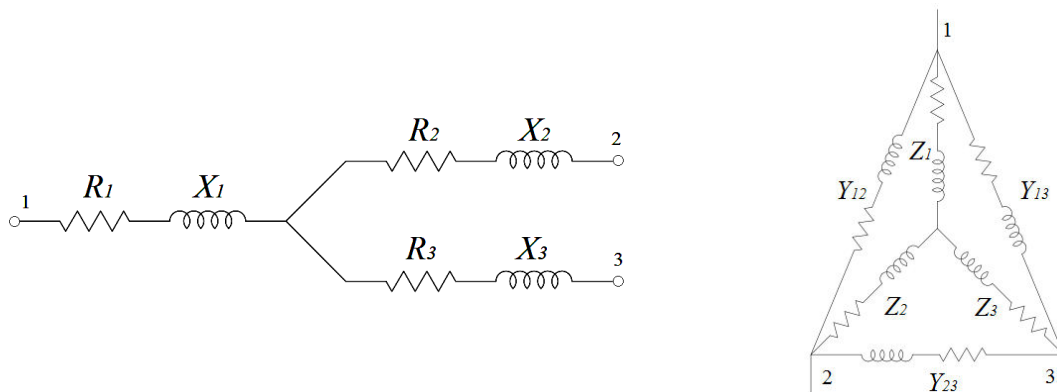
Figure 13 Equivalent networks of a three-circuit transformer: a) star (leakage impedances) network, b) mesh network superposed on its star equivalent

The reactances of the star network can be interpreted as individual reactances of each circuit or, from another point of view, as common or mutual load reactances. For example, power flowing from terminal 1 to either 2 or 3 produces a voltage drop on R_1 and X_1 and effects the voltages on terminals 2 and 3 equally, regardless of which of them connects the load. Thus one can see the impedance Z_1 as a mutual leakage impedance of circuits 2 and 3; it

30

adequately takes into account both the self- and mutual impedance drops of the three circuits for load currents.

A four-winding transformer has six independent impedances among its circuits (counting each different pair of windings). The 4 terminal star network has only four independent elements, and therefore cannot be used as an equivalent representation. Since an *n*-terminal mesh network has *n*(*n*-1)/2 independent elements, it is an excellent representation of the impedance characteristics of the *n*-circuit transformer.

Derivation of the mesh equivalent network is shown in Figure 14: starting from the four magnetically coupled independent windings, their return conductors can be joined together without modifying the impedance characteristics. Since the ampere-turns of all the windings must equal zero and no load current flows through the return conductor, it can be left out. The last step of Figure 14 shows four windings which have self- and mutual impedances or as many admittances. However, if impedances which interconnect the terminals are shown instead of the windings, the mesh network can be obtained: it is qualified as a complete equivalent because it consists of as many independent circuits and impedance elements as the real transformer.
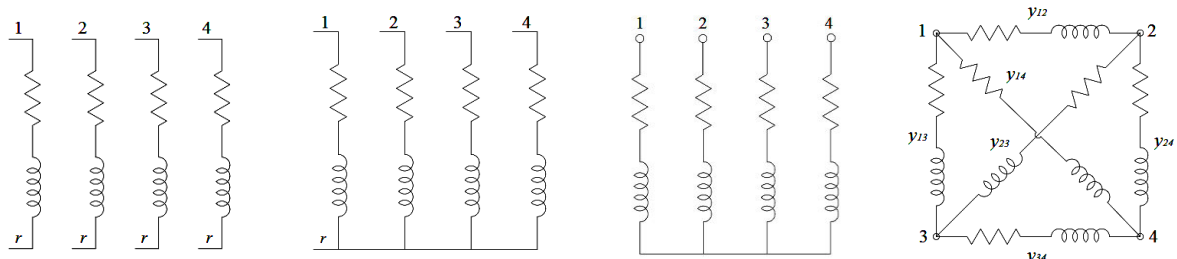
Figure 14 Derivation of mesh network of a four-circuit transformer: a) independent leads, b) four windings with common return, c) four windings with return omitted, d) mesh equivalent network [14]

The links of the mesh network are the load transfer admittances of the windings (with reversed sign), and this holds for any number of windings. Transfer admittance should be understood as a current produced in one circuit by unit voltage across the second circuit (being no voltage across any other circuit). A main disadvantage of the model presented is that some impedances may also appear negative, which cannot be explained practically. However, it is certain that these negative links will have much lower admittance (or much higher impedance) than the others. A possible solution would be to leave out (open circuit) the negative links, or modify the equivalent circuit as shown in Figure 15: it now has eight

elements, out of which only six are significantly different, and moreover, all of them have positive values [17].
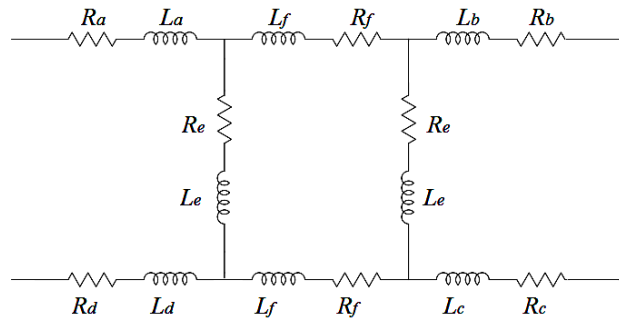
Figure 15 Alternative equivalent network of a four-winding transformer

2.3 Six-winding transformer equivalent network

A significant difficulty in analytical calculation of the equivalent circuit parameters relies in the fact that they are dependent on the main flux that links all the transformer windings, and the self- and mutual inductances between them. The properties of a six-winding transformer equivalent circuit may be adapted from [15] as follows:

- The circuit must have six points of entry, each corresponding to a particular winding;

- The circuit must have 15 independent elements which may be calculated or determined by measurement;

- The circuit should avoid excessive calculations.

As explained previously, the mesh equivalent network can be used as an equivalent representation of *n*-winding transformer. It is a pure mathematical model which does not contain any mutual inductances and can therefore be put in equations by the method of independent potentials as explained by the Kirchhoff's circuit theory. Referring the analysis to a six-winding transformer whose mesh network is shown is Figure 16, the node input currents vector and node potentials vectors can be defined as in Eq. (57) and (58) [18].
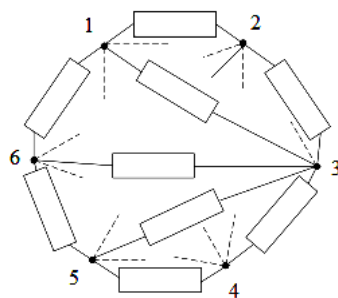
Figure 16 Equivalent mesh (polygon) network of six-winding transformer

$$I_N = \begin{bmatrix} I_{N1} = \sum_{i \neq 1}^{n} I_{1i} \\ I_{N2} = \sum_{i \neq 2}^{n} I_{2i} \\ ..... \\ I_{Nn} = \sum_{i \neq n}^{n} I_{ni} \end{bmatrix} = \begin{bmatrix} I_{12} + I_{13} + ... + I_{16} \\ I_{21} + I_{23} + ... + I_{26} \\ ..... \\ I_{61} + I_{62} + ... + I_{65} \end{bmatrix}. \tag{57}$$

$$U_N = \begin{bmatrix} U_{N1} \\ U_{N2} \\ ..... \\ U_{Nn} \end{bmatrix}. \tag{58}$$

These two vectors are linked through the bus admittance matrix Y_N, which contains the branch admittances, i.e., the reciprocals of the impedances of the polygonal scheme:

$$I_N = Y_N \cdot U_N \tag{59}$$

As the sum of the currents entering and leaving the transformer equals zero, the order of the Y_N matrix has to be reduced by one so as to make it invertible. Therefore, one line and column corresponding to the reference winding, i.e., the primary which represents the transformer supplied side should be taken out. The matrix elements can now be determined by considering the short-circuit impedances between each pair of windings.

Negative impedances (both resistances and inductances) may appear in this network: they cannot necessarily be applied or assigned to internal coils; nevertheless they reproduce faithfully the terminal characteristics of the transformer circuits.

The total copper losses, including stray impedance losses, are correctly represented by the equivalent circuit, whatever the signs of its branches may be; but the simple equivalent circuit does not provide any means of distributing the losses within the transformer windings. Some of these losses are not in the windings at all, but in the clamps, core end plates, and tank [15].

Transformers having n windings per phase have $(n-1)^2$ inductances, out of which $(n-1)$ are self-inductances and the others are mutual. The effect of these inductances on circuit performance can be critical; it is therefore desirable to evaluate them analytically in the transformer design phase [19].

Referring to the equivalent diagram of n-winding transformer shown in Figure 17, its equations can be presented in matrix form where a diagonal element L_{ii} in the inductance

matrix represents the self-inductance of winding i, element L_{ij} represents the mutual coupling from winding j to winding i (voltage induced in winding i by the current in winding j), as shown in Eq. (62) [19]. The magnetomotive force generated by the primary winding equals the sum of the mmfs generated by all the other windings which supply the load.
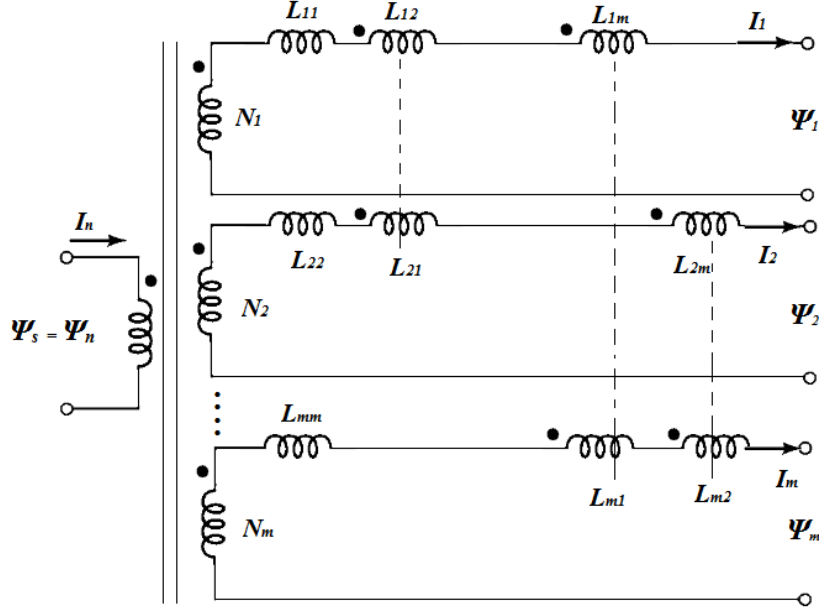
Figure 17 Equivalent diagram of *n*-winding transformer

$$\overline{V_i} = \frac{\overline{V_n}}{N_n} N_i - j\omega \sum_{k=1}^{n-1} L_{ik} \overline{I_k} .$$

(60)

$$N_n I_n = \sum_{k=1}^{m=n-1} N_k I_k .$$

(61)

$$\left[\overline{V}\right] = \frac{\overline{V_n}}{N_n}[N] - j\omega[L]\left[\overline{I}\right].$$

(62)

According to Eq. (62), for a six-winding transformer with three primary and three secondary coils, and relating the flux linkages of each circuit with the currents and the inductances, the system equations can be written in a matrix form as:

$$\left[\begin{bmatrix} \overline{\Psi_P} \\ \overline{\Psi_S} \end{bmatrix}\right] = \begin{bmatrix} [L_{PP}] & [L_{PS}] \\ [L_{SP}] & [L_{SS}] \end{bmatrix} \cdot \left[\begin{bmatrix} \overline{I_P} \\ \overline{I_S} \end{bmatrix}\right] = \begin{bmatrix} L_{11} & L_{12} & \cdots & \cdots & L_{16} \\ L_{21} & L_{22} & \cdots & \cdots & L_{26} \\ \vdots & \vdots & \ddots & & \vdots \\ L_{61} & L_{62} & \cdots & \cdots & L_{66} \end{bmatrix} \cdot \begin{bmatrix} \overline{I_1} \\ \overline{I_2} \\ \vdots \\ \overline{I_6} \end{bmatrix}.$$

(63)

In the Eq. (63), the primary supply voltages and secondary currents can be assumed to be known, due to the knowledge of the supply network and load characteristics. Therefore, the primary currents and secondary voltages can be calculated. Voltage drop is obtained as a

difference between the primary and secondary voltages, which in turn, as explained previously, depends on the leakage inductances contained in the *L* matrix.

Writing the circuit equations for six-winding transformer in terms of self- and mutual inductances is possible as explained, but their analytical calculation could be cumbersome. They are containing the combined effects of the main core flux (represented by the magnetizing inductance) and additional contribution due to the leakage fields; however it is not possible to distinguish them in the matrix of self- and mutual inductances, since Starr equivalent circuit cannot be drawn.

The main flux in the core is sustained by the magnetizing magnetomotive force, which is generally very small. In practice, transformer operation depends on the leakage inductances, but it is not clearly evident in which manner. Another observation to be highlighted is the non-linearity of the *L* matrix elements: the values of self- and mutual inductances are affected by core saturation, but it is complicated to take this effect into account by analytical approaches. The assumption on constant permeability of the core laminations can be removed: it is possible to take into account the actual magnetizing *B*(*H*) curve in Finite Element Method (FEM) software.

2.4 Multi-winding transformers application examples

Multi-winding transformers are utilized in various applications. Some of them are:

- Traction systems: typically as low frequency four-winding transformers with split windings, used beside the rectifier converters [20];
- Multi-level inverters: in both diode- and capacitor-clamped; by choosing appropriately the switching strategy, it is possible to synthesize a sinusoidal output from square wave input [21];
- Stand-alone PV systems, again as a part of the multilevel inverter topology, achieving high efficiency for low-power applications [22];
- Switched-mode power supplies: usually planar core high frequency transformer [23];
- Adjustable speed drives with isolation medium frequency transformer which shows efficiency of 99% and reduced overall size and weight by 70% [24];
- Electric vehicle charging station employing transformer with multiple secondary windings [25];

- Wind farm distribution transformers usually with two secondary windings, each with half the nominal rating of the transformer in order to keep the short-circuit power level at medium voltage down to a manageable level [26], etc.

Considering the variety of application areas, multi-winding transformers also vary in size from a few kVA for electronics applications to several MVA for large power systems. One of the leading trends nowadays is increasing the transformer operation frequency in order to reduce its size and costs.

As a practical example in this thesis a three-phase multi-winding low frequency transformer with one primary and multiple secondary windings used in electric vehicle dc charging stations will be analyzed. A block diagram of the system is shown in Figure 18; it should be noted that the primary side is chosen to be made up of three coils supplied in parallel form the mains, although there could be only one single coil. According to the European patent [25], the number of secondary windings is to be defined in each particular situation; they are however electrically and galvanically separated from one another.
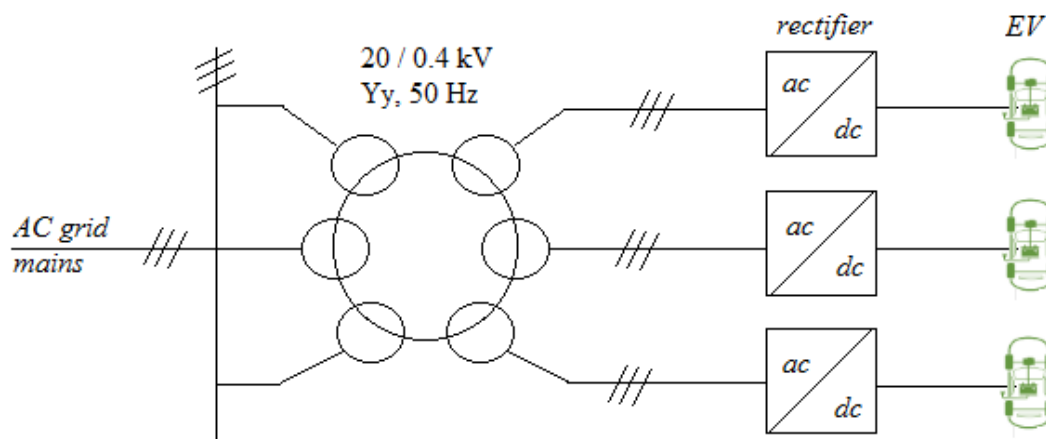
Figure 18 Block scheme of the EV dc charging station

This solution employing a multi-winding transformer facilitates scalability, so that the charging station can more easily be adapted to the required number of vehicles to be charged. It also reduces the footprint with respect to two-winding transformers which were traditionally used.

A key advantage of the overall system is the possibility to provide charging for two or more electric vehicles simultaneously, by independently controlling at least two ac-dc converters which operate in parallel. Between each secondary winding and the rectifier there is typically a circuit breaker or a fuse-switch disconnector. One or more secondary windings can be used for supplying auxiliary equipment in the substation. Another system topology

variation is made by connecting two secondary windings to the same converter (Figure 19); in this case each rectifier consists of two series connected Graetz bridges with $q = 12$ pulses in the output voltage. This configuration results in less ripple and therefore lower harmonic content in the dc current, which means a smaller filter will be required [25].
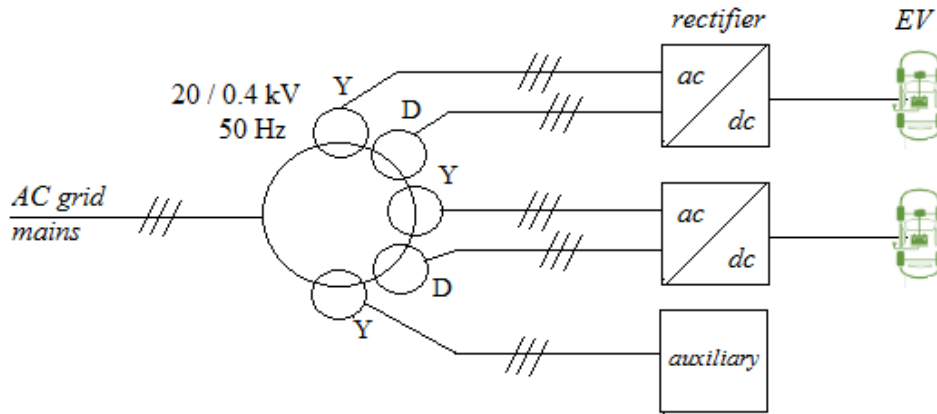
Figure 19 Block scheme of the EV dc charging station with 12 pulse rectifiers

A more profound analysis of the possible ac-dc power conversion topologies will be presented in the following chapters. The choice of these system components is fundamental in determining the transformer sizing criteria, as well as estimating its performances in non-ideal operating conditions.

3 Electric vehicle charging station components and performances

In this chapter the general system for electric vehicle dc charging station which is presented in the European patent and briefly discussed in Chapter 2, is analyzed further in details in terms of components characteristics and choice, control methods and overall system assessment. Once the topology is chosen, it is easier to determine all the requirements and limitations for designing the multi-winding transformer and to estimate its performances.

3.1 Type of EV charging station

EV charging system consists of all the equipment required to condition and transfer energy from the supply network (constant voltage and constant frequency) to EV traction battery bus (direct current and variable voltage) for the purpose of charging the battery and/or operating vehicle electrical systems while connected [27]. In general, there are three main ways of charging: conductive, inductive and by replacing the battery. Conductive charging system, which is considered in this work, uses direct contact between the EV connector and charge inlet. The cable can be plugged in a standard electrical outlet or a devoted charging station. One of the possible problems when connecting the EV to the power supply is the variety of chargers and lack of internationally established standards. An important aspect is the so called charging level, which describes the available power level of a charging outlet. The charger location and the approximate charging time depend on the charging level. Considering that usage of multi-winding transformer makes sense only in case of off-board chargers and the output of the station will be dc plug for charging each vehicle separately, the classification of power levels according to Society of Automotive Engineers (SAE) standards and the Japanese CHAdeMO Association is presented in Table 1.

Table 1 DC charging power levels according to CHAdeMo and SAE [28], [29]

DC Voltage levels [V]	Charger location	Typical use	Power level	Time for charging
Level 1 200 – 450	Off-board	Charging at home/office	≤ 36 kW 80A	PHEV: 22 min
Level 2 200 – 450	Off-board	Charging at private or public outlets	≤ 90 kW 200A	PHEV: 10 min
Level 3 200 – 600	Off-board	Commercial	≤ 240 kW 400A	Battery EV: ≤ 10 min

Off-board chargers are becoming more preferable to on-board ones, due to their capability to provide charging at high power levels for much shorter time. They also decrease the weight of the EV and allow for improved systems for managing the batteries [29].

Level 3 charging is termed as "fast dc charging", up to 50 kW according to SAE Standards, or up to 240 kW according to CHAdeMO. The battery capability to store electric charge before it is completely discharged is called battery capacity C and it is expressed in coulomb, or more often, in ampere-hour. For example, a battery of 20 Ah can supply current of 1 A for 20 h, or 2 A for 10 h. An important parameter of the electric vehicle is the battery state of charge (*SOC*). It is a measure of the residual capacity of a battery and it can be calculated as [30]:

$$SOC(t) = \frac{\int_{t_0}^{t} I_b(\tau)d\tau}{Q_0} \cdot 100 \ \ [\%],$$

(64)

where I_b is the charging current and Q_o is the total charge a battery can hold. Usually the battery *SOC* should be maintained between 20% and 95%. Dc charging is typically measured up to 80% of the battery rated capacity, because the last 20% take very long time to be completed. Level 3 means 20-30 min charging from empty to 80% full battery [31]. This type of charging is intended for commercial and public applications where it can operate as a filling station, installed in parking lots, shopping centers, hotels, rest stops, etc. [28].

The Japanese protocol known as CHAdeMO is gaining international recognition. In 2016, CHAdeMO Association modified the dc (fast) charging protocol in such a way that it responds better to market needs. Having recognized the trend towards mass market EVs with high capacity batteries, the Association established charging up to 100 kW continuous power, 150-200 kW peak power (500 V dc, 350-400 A) [32]. Further development in terms of higher power has been oriented towards 350-400 kW (1 kV x 400 A), enabled via multi-stand, power-share type of chargers; the protocol publication is expected to happen in 2020. Nowadays CHAdeMO is also aiming at 900 kW (1.5 kV x 600 A) [33], [34].

Another important aspect is the so called charging mode: it describes the safety communication protocol between the EV and the charging station. For dc connection and fast charging, mode 4 applies: the EV should be connected to the main power supply grid though an external charger. All the control and protection circuits are permanently installed in the station and therefore the charger is a part of the station, not of the vehicle [27].

There are some considerable issues associated with integration of EVs in power networks in general, such as: increase in load profile during peak hours, quick overloading of local distribution network and system components, system stability issues, etc. [29]. These are even more severe in case of high-power rapid charging stations (Level 3). Other problems created by fast charging are: voltage deviations, harmonic distortion, thermal loading, etc. These could significantly impact distribution transformer life due to increased power losses and decreased reliability, efficiency and economy of developing smart grids [28].

It is worth mentioning that in fast charging mode, preferable direction of the power flow is from the utility to the battery in the EV, i.e., unidirectional charging only. Reverse power flow opposes the basic purpose and premise of minimizing connection time and delivering substantial energy as quickly as possible. The system with capability of unidirectional power flow requires minimum hardware, enables much simpler interconnection and lowers battery degradation issues [29].

The essential requirements for fast dc charging stations to be met with respect to the supply grid can be summarized as [35]:

- Operation free form harmonic components;
- High power factor (as close to unity as possible);
- Galvanic isolation.

Additional requirements towards the EV are:
- Regulated output dc voltage for EV batteries to regulate charging power and maximize battery life;
- High efficiency of the power electronic converter (since high power is transferred).

In order to minimize the impact that EV charging station has on the power quality, the EV charger must ensure that the utility current is drawn with low total distortion. A high power factor is required to maximize the real power available from a utility outlet. IEC 1000-3-2 Standard limits the allowable harmonic and dc current injection into the grid and the EV chargers shall be designed to comply with it [28]. This standard also defines limits for testing the harmonic current emissions of electronic and electrical equipment. Compliance with IEC 1000-3-2 ensures that the tested equipment will not generate harmonic currents at levels which cause unacceptable degradation of the mains environment. According to the equipment classification in this standard, EV charging station should belong to class A. Maximum permissible harmonic currents amplitudes (odd and even) are given in Table 2 [36].

Table 2 Current harmonic limits for Class A equipment

Harmonic order h	Max. permissible harmonic current [A]	Harmonic order h	Max. permissible harmonic current [A]
3	2.30	2	1.08
5	1.44	4	0.43
7	0.77	6	0.30
9	0.40	$8 \leq h \leq 40$	0.23 x 8/h
11	0.33		
13	0.21		
$15 \leq h \leq 39$	0.15 x 15/h		

According to the IEEE Std. 519-1992, the harmonic limit for a single consumer is specified as 15% for harmonics lower that 11th order [37]. In case of light duty PHEVs, the guideline is set by the aforementioned IEC 1000-3-4, which suggests a maximum current THD of 20% and a minimum power factor of 0.95.

3.2 Battery considerations

Batteries are used as on-board storage components in EVs and are expected to meet specific criteria in terms of energy density, power density, safety and cycle life in order to be feasible for use in EVs. In Table 3 a brief comparison between some of the common batteries is shown, based on the battery chemistry.

Table 3 Characteristics of batteries for EVs [30]

Battery type	Cycle life	Efficiency [%]	Specific power [W/kg]	Specific energy [Wh/kg]
Lead acid	500 – 800	50 – 92	150 – 400	30 – 40
Li-ion	400 – 1,200	80 – 90	300 – 1,500	150 – 250
Nickel metal hydride NiMH	500 – 1,000	66	250 – 1,000	30 – 80

Lead acid batteries can last for a long time, but their energy-to-volume ratio is low and their treatment after being used is a problem; therefore they cannot meet the requirements for environmentally friendly vehicles. NiMH batteries show high specific energy and energy density, and a long cycle life; therefore they are becoming more interesting nowadays. On the other hand, the maximum capacity of Li-ion batteries does not decrease if not charged to the fullest or when charged repeatedly. They have low self-discharge rate and high power-to-volume ratio; however they require a lot more safety attention and are susceptible to

overcharging [30]. In Tesla vehicles, three-component Li-ion batteries are used; Lithium iron phosphate batteries are also widely used because of their high charge-discharge current and slow capacity attenuation.

The power level at which a battery cell can receive a charge is determined by the battery chemistry and the method used to charge it. Some of the basic battery charging methods used at present are listed below. Their aim is to prevent from or reduce damage due to large energy throughput a high power [38]:

- Constant current (CC) charging method: it is simple to be used and easy to be controlled. Typical charging profile with pulse current is shown in Figure 20. Selecting very small charging current increases significantly the charging time. On the other hand, if the charging current is too large, there is a high possibility of overcharging, which will decrease the battery life;

- Constant voltage (CV) charging method: it is easy to operate and cannot overcharge the battery at the later stage. However, due to low electromotive force at the battery terminals in the early stage, large current is required, which can lead to bending of the plates and quick temperature increase. Selecting too low charging voltage leads to insufficient charging and shortening battery life;

- Stage charging method (constant current – constant voltage): it combines the advantages of both aforementioned methods: avoids the problems of excessive charging current in the early stage and easy overcharging in the latter stage, and it has high charging efficiency (Figure 21).

At the beginning of the stage charging method (CC-CV) a constant current is applied to the battery charger, so the state of charge (SOC) of the battery increases linearly, as well as the open-circuit voltage (OCV) and battery voltage accordingly. As the battery voltage reaches the maximum cutoff voltage (typically 450 – 480 V), the charging mode is switched to CV. In this stage the SOC and the OCV keep increasing. Therefore, the voltage across the internal resistance of the battery gradually decreases, which leads to current decrease. The charging stops when the charging current is diminished to a low threshold (I_{CO}), usually of magnitude $C_{dis}/100$, where C_{dis} is a measure of the rate at which a battery is discharged relative to its maximum capacity [39]. Another possible variation of this method is to gradually increase charging current as a staircase wave at the beginning to avoid damaging

the battery until each cell voltage reaches a specified threshold level. This is known as pre-charging stage [40].
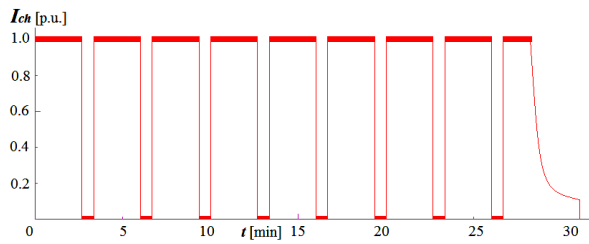
Figure 20 Typical CC charge profile of Li-ion battery [41]
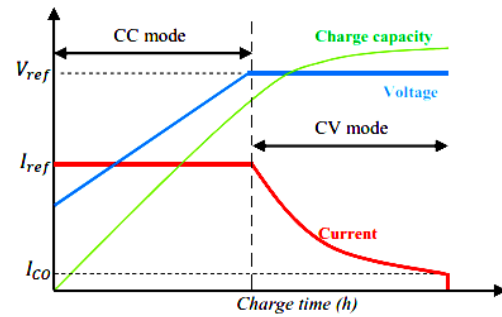
Figure 21 Typical CC- CV charge profile of Li-ion battery [42]

The time needed to charge the battery is a function of the battery capacity, charging standard (SAE J1772 vs. CHAdeMO) and starting energy level of the battery. Active power absorbed is constant and equal to the rated battery power until the *SOC* reaches 50%. Then it decreases linearly until *SOC* = 80%, when for dc charging it can be considered that the battery is fully charged (Figure 22) [43]. In Table 4 a brief summary of the battery characteristics used in different commercial vehicles is shown.
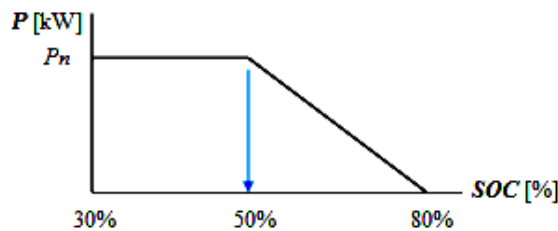
Figure 22 Power absorbed by the battery with respect to its state of charge

Table 4 Characteristics of batteries used in commercial EVs [29]

Car	Li-Ion Battery [kWh]	Distance coverage [km]	Demand [kW]	Time for charging [h]
Tesla Roadster	54	547	100	0.37
Nissan Leaf	24	257	Up to 50	0.3 – 0.4
Mitsubishi i-MiEV	16	233	Up to 50	0.26
Toyota RAV4	42	257	50	0.64

3.3 System topology reviewed

The basic topology of EV dc charging station as proposed in Figure 18 does not provide any details about the characteristics of the ac-dc converter, therefore in this section two possible solutions are presented and compared in terms of output waveforms and control strategies. Galvanic isolation from the mains is already ensured at the front-end by employing a low frequency (50 Hz) line multi-winding transformer in both cases.

3.3.1 Two-stage power conversion

The topology proposed in Figure 23 consists of two main blocks: ac-dc power converter at the front-end and dc-dc converter at the back-end which define the two stages of power transformation. Considering unidirectional charger configurations for high power level and low frequency line transformer, a combination of diode bridge and step-up/down converter is a reasonable choice.
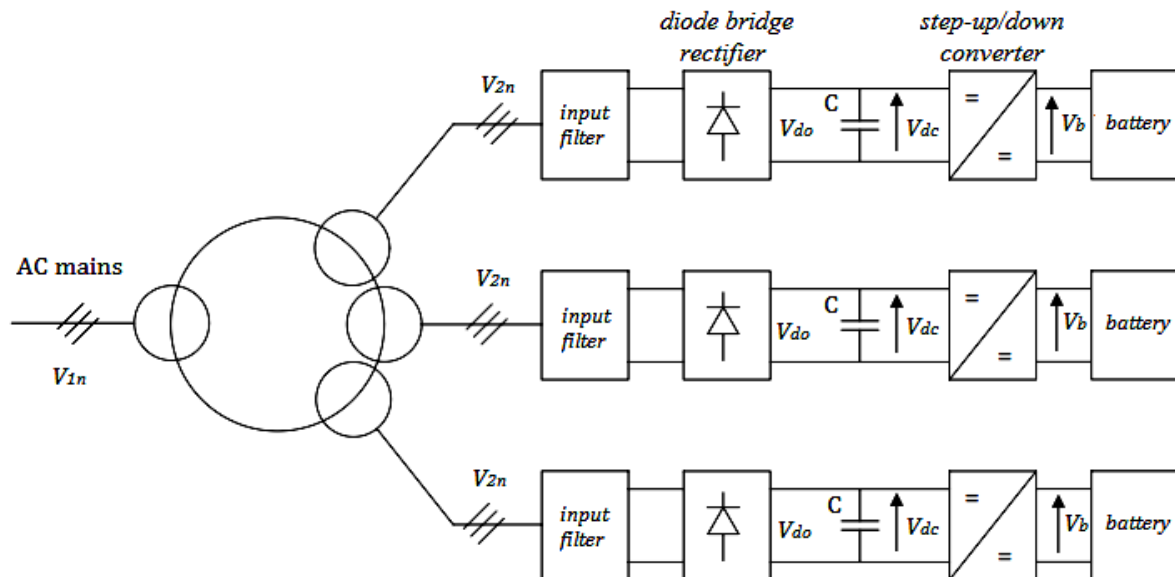
Figure 23 Two-stage EV dc charging station topology

AC-DC high-power converter: it is expected to perform rectification of the ac supply voltage, to provide operation free from harmonic distortions, to achieve high power factor (by shaping the input current) and to have low initial and maintenance costs (which means low number of active switches and reduced stress on the passive and active elements) [35], [39]. Power factor and total harmonic distortion (THD) are the major factors which influence the selection of a particular PFC rectifier topology. In this case, boost type devices and their variants can be widely used. Some of the possible choices for enhancing the system performances are: three-phase diode bridge rectifier, three-phase bridgeless boost converter, VIENNA rectifier, etc. [35]. Special attention has to be paid to heat dissipation, as the diode

bridge may experience this problem. Another important issue may be the electromagnetic interference (EMI) introduced by the boost converter type due to the voltage harmonic components. Table 5 provides a basic qualitative comparison among the possible choices for a device to be used at this stage.

Table 5 Comparison of ac-dc converters for rectification stage in fast EV charging stations [44], [45].

Topology	Advantages	Disadvantages	Components list
3-phase diode bridge rectifier	-no control required -low cost -small dimensions -high reliability	-heat dissipation might be a problem -sensitive to overvoltages -low-frequency harmonics are present	-6 diodes -3 inductors -1 capacitor
3-phase bridgeless boost converter	-easy to meet EMI requirements -small number of components -does not require neutral connection -high efficiency	-complex control -high power stress	-6 IGBTs -3 inductors -1 capacitor
3-phase Vienna rectifier	-simple control -does not require neutral connection -high efficiency -cancels output current harmonics	-large number of components -lower reliability	-3 IGBTs -3 inductors -18 diodes -2 capacitors

DC-link: the voltage of the dc-link normally varies from 600 V to 750 V (higher than the battery voltage, which ranges from 200 V to 500 V) [45]. Since the chargers are likely to supply power to a wide range of batteries with various initial *SOC*, it is therefore important to have high voltage dc-link. This will also improve the input power factor.

DC-DC converter: it is expected to adjust the voltage level appropriate for charging the EV battery. A major factor in selecting this converter is the desirable level of output power. Apart from providing regulated voltage and current to improve battery charging performances, this stage has also to ensure high power factor, wide line regulation performance and ripple-free charge current and voltage [39].

A single-phase step-down (buck) converter can be used at the back-end. Its configuration requires small number of components and the control scheme is very simple, which implies low cost. However, in order to suppress the current ripples in high-power applications, a large inductor is necessary. Since the inductor typically has large volume and weight, it is the bulkiest element in this topology; thus decreasing its size arises as a primary target in designing the system. The inductor size is inversely proportional to switching frequency,

while switching frequency is directly proportional to switching losses. Therefore, there has to be a trade-off between inductor size and switching losses [45]. Power factor correction with buck converter is poor and protection from inrush currents may be needed [29].

If there is a necessity to increase or decrease the dc voltage which supplies the vehicle's battery (depending on the battery rated parameters, which are not known in advance, therefore a wide range should be provided) a step-up/down converter can be utilized. The number of components in this configuration is still reasonably small, and the control circuits are not complex; however the input voltage ripples are high as well as the electrical stresses. The input current will be pulsating [29].

Another possibility is to use multi-phase interleaved buck converter which increases the overall system efficiency. In this case, the fundamental frequency is multiplied by the number of phases, thus resulting in a higher system frequency with decreased current ripple, reduced EMI and smaller output filter. Three-phase interleaved buck converter (Figure 24) is made up of three identical single phases which operate independently from each other. The control scheme may employ phase shifted PWM in which each pulse is shifted by $n/360^o$ (in this case it corresponds to 120° shift). Output current ripples will be generally compensated as they oppose each other [35].
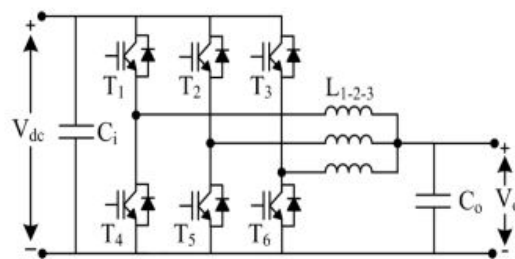
Figure 24 Three-phase interleaved buck converter [54]

In Table 6 a brief summary of the ranges and maximum allowable values for the system voltages is given. Based on the qualitative discussion presented, a simple system configuration (in terms of components and control required) consisting of three-phase diode bridge rectifier and step-up/down converter (as shown in Figure 25) is analyzed further.

Table 6 Typical rated values of the EV charging station system

V_{2n}	400 V	V_{bn}	200 – 500 V
V_{do}	540 V	P_{bn}	50 – 350 kW
V_{dc}	600 – 750 V	I_{bn}	≤ 400 A
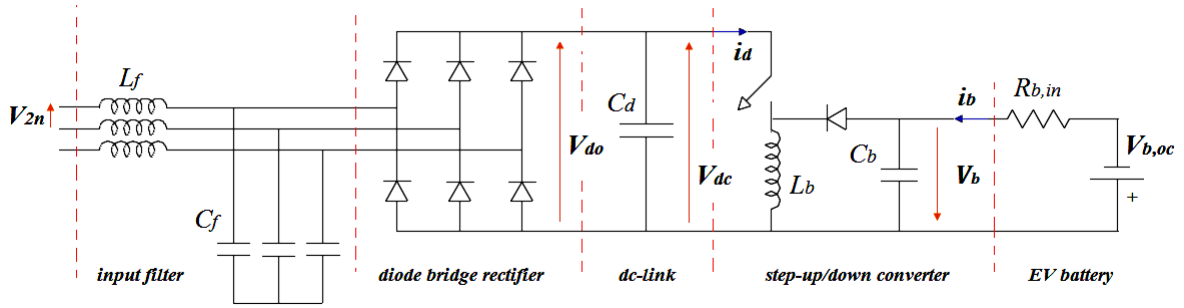
Figure 25 Detailed two-stage EV dc charging station topology (from a single secondary transformer winding to a single charging outlet)

At the first instant, the input filter capacitance can be neglected and only an input inductance can be taken into account (typically in the order of µH): it is the inductance of the transformer winding plus the one of the cable connections. Setting a condition on a constant current which charges the battery, $i_b = I_{bn} = const.$, the battery itself can be modelled as a constant current source. If the transformer secondary rated line-to-line voltage is $V_{2n} = 400$ V, neglecting the voltage drop on the input inductance, the theoretical average value of the diode bridge rectifier output voltage will be:

$$V_{do} = \frac{3\sqrt{2}}{\pi}V_{2n} = 540 \text{ V} \tag{65}$$

The maximum value of this rectified voltage is:

$$V_{do,\max} = \sqrt{2}V_{2n} = 565.7 \text{ V} \tag{66}$$

The voltage waveforms are shown in Figure 26, where T is the period of the sinusoidal input voltage $T = 20$ ms. Due to the capacitor C_d, it can be assumed that the input voltage to the step-up/down converter is constant:

$$V_{dc} = V_{do,\max} = const. = 565.7 \text{ V} \tag{67}$$
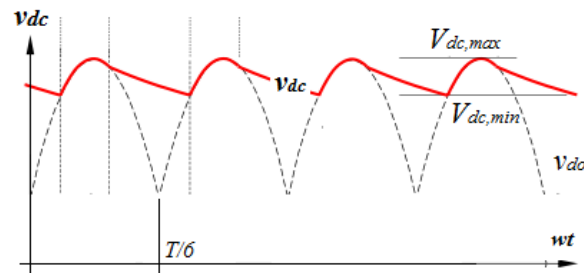
Figure 26 Intermediate dc-link voltage waveforms

47

If the battery to be charged has a rated power of $P_{bn} = 350$ kW and the charging current is limited to $I_{b,max} = 400$ A (according to the CHAdeMO protocol), the battery voltage V_b can be calculated:

$$V_b = \frac{P_{bn}}{I_{b,max}} = 875\,\text{V} \tag{68}$$

It is evident that in this case the dc-dc converter should operate as a step-up in order to increase the input voltage V_{dc} to the required value V_b. For a buck-boost converter as used in this topology, the Eq. (69) holds [44]:

$$V_b = V_{dc} \cdot \frac{D}{1-D} \tag{69}$$

Therefore, the duty cycle can be calculated (expected value is above 0.5):

$$D = \frac{V_b}{V_b + V_{dc}} = 0.607 \tag{70}$$

The average value of the input current i_d can also be calculated using the buck-boost relationship between its input and output current:

$$I_d = I_b \frac{D}{1-D} = 617.81\,\text{A} \tag{71}$$

In any other case, starting from the rated battery power (lower or equal to 350 kW) and its rated voltage V_{bn}, the duty cycle and the charging current can be determined as shown previously.

It can be assumed that the current entering the dc-dc converter i_d consists of two components: a constant current (which flows out of the bridge rectifier) and a current ripple (which flows through the capacitor C_d): $i_d = I_d + i_{dr}$.

In the next step some of the topology components will be designed briefly. Setting up a condition on the allowed voltage ripple at the intermediate dc-link (for example, 5% of V_{dc}), the value of the capacitor C_d can be determined:

$$\Delta V_{dc} = -\frac{I_d}{C_d} \cdot \Delta t \Rightarrow C_d = \frac{I_d}{0.05 \cdot V_{dc}} \cdot \frac{T}{6} = 72.8\,\text{mF} \tag{72}$$

The calculated value is obviously too high to be practically implemented. It can be decreased by increasing the allowed voltage ripple; however this is not advisable. Therefore,

a smaller value should be accepted, for example, $C_d = 1$ mF. Assuming a switching frequency of a few kHz (let's say, $f_{sw} = 4$ kHz) and a duty cycle as calculated $D = 0.607$, the value of the capacitor C_b of the dc-dc converter can be determined as:

$$\Delta V_b = \frac{I_b \cdot D}{C_b \cdot f_{sw}} \Rightarrow C_b = \frac{I_b \cdot D}{0.05 \cdot V_b \cdot f_{sw}} = 1.58 \text{ mF} \tag{73}$$

The inductance of the dc-dc converter is determined by limiting the current ripple to a reasonable value, for example, 10% as shown:

$$\Delta I_L = \frac{V_{dc} \cdot D}{L_b \cdot f_{sw}} \Rightarrow L_{b,\min} = \frac{V_{dc} \cdot D}{0.1 \cdot I_d \cdot f_{sw}} = 1.39 \text{ mH} \tag{74}$$

All the relevant current waveforms are shown in Figure 27 [44], [46]. They come in handy when identifying the current harmonic components which are injected into the grid.
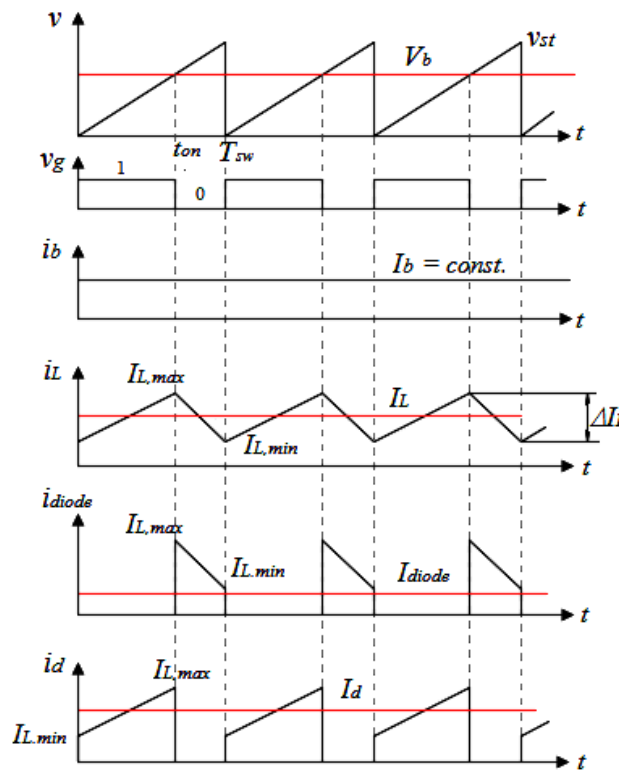
Figure 27 Two-stage conversion topology waveforms: v_{st} – sawtooth voltage, v_g – switch control signal, i_b – battery charging current, i_L – current through the step-up/down inductor L_b, i_{diode} – diode current, i_d – input current in the dc-dc converter [44], [46]

The maximum and minimum values of the current can be calculated as:

$$I_{L,\min} = I_L - \frac{\Delta I_L}{2} \text{ and } I_{L,\max} = I_L + \frac{\Delta I_L}{2}, \tag{75}$$

where I_L is the average value of the current through the inductor L_d.

In order to calculate the current harmonics injected into the grid, the equivalent circuit in Figure 28 is to be used, having in mind that only two phases of the diode bridge rectifier are conducting at each time instant.
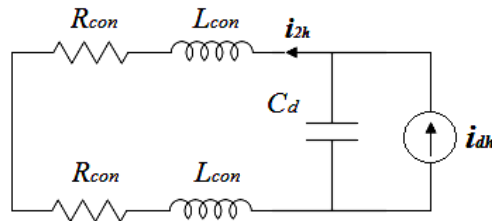
Figure 28 Current harmonic injection equivalent circuit: R_{con} and L_{con} are the connecting resistance and inductance respectively

As a first step, the current waveform i_d should be decomposed by Fourier series into an infinite number of sinusoidal components in order to calculate the amplitude of the current harmonics at the switching frequency and its multiples. Taking into account the current waveform as shown in Figure 27:

$$i_d(t) = \begin{cases} I_{L,\min} + \dfrac{V_{dc}}{L_b}t, & 0 \le t < t_{on} \\ 0, & t_{on} \le t < T_{sw} \end{cases} \tag{76}$$

The peak values of its harmonic components are calculated:

$$\hat{I}_{s(h)} = \frac{2}{T_{sw}} \int_0^{t_{on}} i_d(t) \cdot \sin\left(h\frac{2\pi}{T_{sw}}t\right) dt \tag{77}$$

$$\hat{I}_{s(h)} = -\frac{I_{L,\min}}{h\pi}\left[\cos(h2\pi D) - 1\right] - \frac{V_{dc}D}{h\pi L_b f_{sw}}\cos(h2\pi D) + \frac{V_{dc}}{2h^2\pi^2 L_b f_{sw}}\sin(h2\pi D)$$

$$\hat{I}_{c(h)} = \frac{2}{T_{sw}} \int_0^{t_{on}} i_d(t) \cdot \cos\left(h\frac{2\pi}{T_{sw}}t\right) dt \tag{78}$$

$$\hat{I}_{c(h)} = \frac{I_{L,\min}}{h\pi}\sin(h2\pi D) + \frac{V_{dc}D}{h\pi L_b f_{sw}}\sin(h2\pi D) + \frac{V_{dc}}{2h^2\pi^2 L_b f_{sw}}\left[\cos(h2\pi D) - 1\right]$$

Then the amplitude of each harmonic is:

$$I_{d(h)} = \sqrt{\hat{I}_{s(h)}^2 + \hat{I}_{c(h)}^2} \tag{79}$$

In case needed, the waveform can be expressed as:

$$i_d(t) = I_d + \sum_{h=1}^{\infty} \left(\hat{I}_{s(h)} \sin(h\omega_1 t) + \hat{I}_{c(h)} \cos(h\omega_1 t) \right)$$ (80)

Analyzing the equivalent circuit for current injection, the current entering the grid can be determined. At each harmonic frequency, in the expression (81) ω is to be multiplied by the harmonic order h.

$$I_2(j\omega) = \frac{1}{-2L_{con}C_b\omega^2 + j2R_{con}C_b\omega + 1} \cdot I_d(j\omega)$$ (81)

Another important aspect is identifying the harmonic components present in the transformer secondary currents, because they are expected to reflect on the primary side currents. As mentioned previously, the current flowing out of the diode bridge rectifier is assumed to be constant. Therefore, the waveforms of each phase current entering the diode bridge are shown in Figure 29 (each diode conducts for 120°).
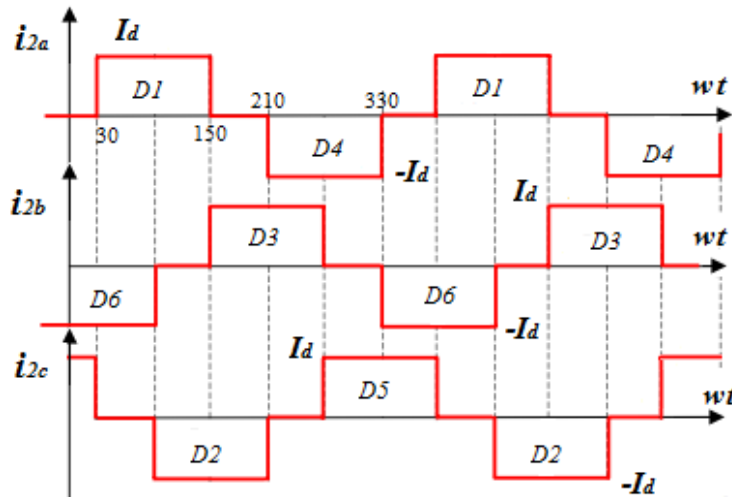
Figure 29 Transformer secondary phase current waveforms [47]

The root mean square value of the diode bridge input current is:

$$I_{2a,rms} = \sqrt{\frac{1}{T}\int_0^T i_{2a}^2(t)dt} = \sqrt{\frac{2}{3}} \cdot I_d$$ (82)

It is evident that three-phase currents absorbed by the diode bridge rectifier are not sinusoidal, but square waves phase shifted by 120°. In addition to the fundamental component, current harmonics of order $h = 6k + 1$ are present, where $k = 0, \pm 1, \pm 2, \pm 3$, etc., i.e., $h = 1, 5, 7, 11, 13, 17, 19$, etc.

The root mean square values of the fundamental primary transformer current harmonic and of each higher harmonic are:

$$I_{1,rms} = \frac{\sqrt{6}}{\pi} I_d \tag{83}$$

$$I_{h,rms} = \frac{I_{1,rms}}{h} \tag{84}$$

In Yy connection primary currents will follow the same waveforms as the secondary currents shown in Figure 29. It should be emphasized that the low-frequency harmonics present in the secondary, and therefore, also in the primary currents have particularly high values. They will cause additional voltage drop and distortion of the mains voltage. A possible solution is to employ filters in order to counteract the production of the harmonics.

It is advisable that either the primary or secondary winding are delta connected. Due to the core non-linearity, i.e., hysteresis, triplet fluxes will occur and if a delta connection is used, triplet currents can circulate in the winding, therefore suppressing the generation of triplet core fluxes.

In case when the transformer consists of several secondary windings, each of them supplying a separate diode bridge rectifier and a separate load, the primary current of each phase will be a sum of all the secondary currents of the same phase. The waveforms in Yy connection are exactly the same as in Figure 29 it is the amplitude that changes due to the sum and the transformer ratio.

3.3.2   Single-stage power conversion

In this configuration, both ac-dc and dc-dc stages explained previously are combined in and performed by one single converter, known as voltage source inverter (VSI) boost rectifier. The topology shown in Figure 30 requires inductors to shape the converter input current; these can be designed on purpose or secondary leakage inductance of the supply transformer can be used if known in advance. The output voltage V_{dc} will be higher than the input phase voltages. This rectifier is compact and can achieve smaller size, lower cost and high efficiency. However, it contains high-frequency current ripple and the output voltage range is limited [35], [39].
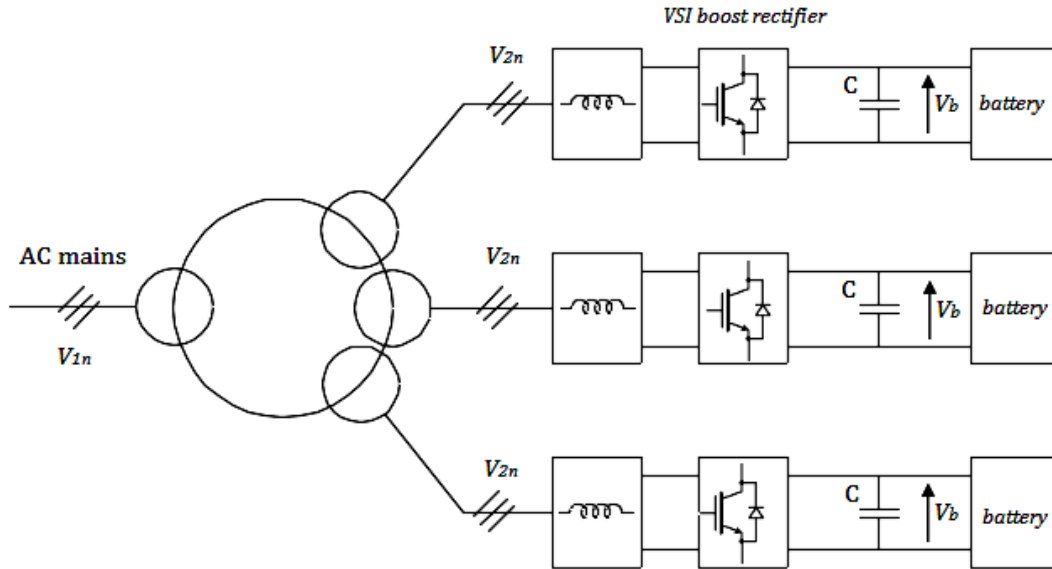
Figure 30 Single-stage EV dc charging station topology

A detailed scheme of the VSI boost rectifier is shown in Figure 31. Several control techniques can be applied to this VSI, such as: hysteresis current control, sinusoidal PWM, space vector modulation, etc. Due to the nature of step-up inductors, a high input power factor can be observed for all of these control schemes [48], [49]. In case of employing sinusoidal PWM, the amplitude of both the output voltage V_{dc} and input current can be adjusted by varying the modulation index. In order to obtain a high power factor while keeping V_{dc} at the desired value, phase angles of the reference waveforms should be shifted optimally with respect to the corresponding line voltages [35].

If a high switching frequency is chosen, the input inductance size can be minimized; therefore the voltage drop across L_S is small and the root mean square value of the converter line-to-line input voltage is approximately equal to the supply line-to-line voltage.
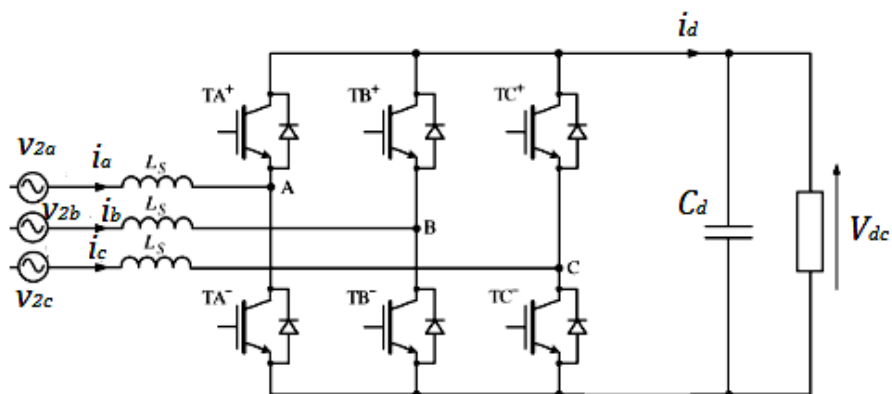
Figure 31 Three-phase six-switch voltage-source inverter (VSI boost rectifier) [50]

If this converter is to be pulse-width modulated in a linear range with amplitude modulation index $m_a \leq 1.0$ to control the input currents to be sinusoidal, then the output voltage amplitude is higher than the input line-to-line voltage [44]:

$$V_2 = \frac{\sqrt{3}}{2\sqrt{2}} m_a V_{dc} \implies V_{dc} = \frac{2\sqrt{2}}{\sqrt{3}} \frac{V_2}{m_a} \geq 1.634 \cdot V_2. \tag{85}$$

In three-phase converters as the one discussed here, the output current i_d consists of a dc component and high-switching-frequency components (the ripple at twice the line frequency does not exist as in the single-phase rectifiers) [44]. The high-frequency ripple superimposed on the sinusoidal input line current, which is caused by the switching action and has a frequency equal to f_{sw}, can be observed in Figure 32.
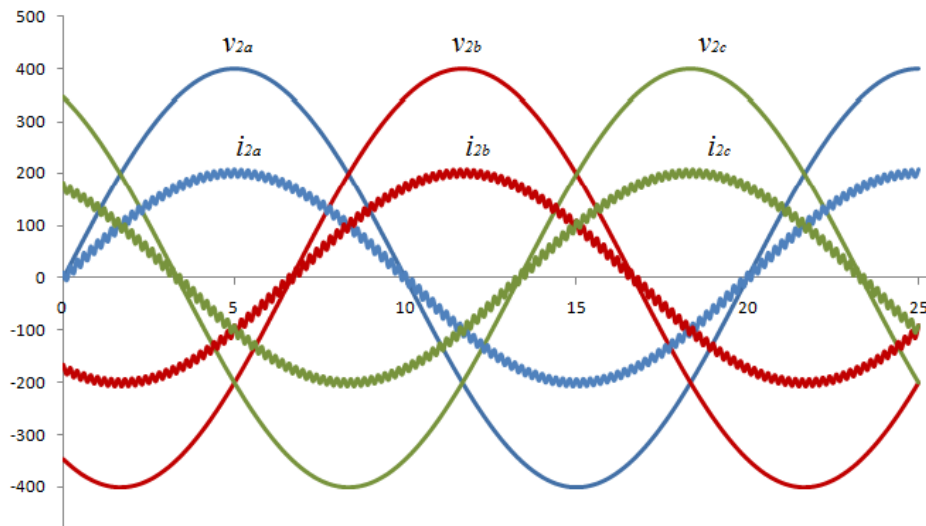
Figure 32 Input voltages and currents in a three-phase PWM rectifier

The amplitude of this ripple is defined as in Eq. (86), which makes it obvious that it will be maximum when the phase voltage v_2 takes on zero value [50].

$$\Delta I_S = \frac{V_{dc}}{2L_S f_s} \left[1 - \left(\frac{v_2}{V_{dc}} \right)^2 \right]. \tag{86}$$

The output dc voltage v_{dc} also fluctuates about its average value V_{dc} with a peak-to-peak value which depends on the capacitance C_d and has a value:

$$\Delta V_{dc} = \frac{V_2 I_2}{\omega C_d V_{dc}}. \tag{87}$$

This voltage ripple should generally be less than 1% of the value V_{dc}.

With respect to diode-bridge configuration, the ac current at the input will be almost sinusoidal, leading to a significant reduction in the dc side harmonic content. However, switch-mode VSI requires complex control to adjust the output voltage and involves greater power losses due to the high switching frequencies for the semiconductor devises [50].

If hysteresis control (HC) is used, a satisfactory power quality and fast dynamic response of the converter can be achieved; however the switching frequency depends on the source inductance and the load voltage, therefore it is not constant. Sinusoidal PWM is easy to implement and gives lower switching power losses compared to HC, nevertheless the input current THD will be slightly increased. Similar performances can be obtained by SVM but at half the switching frequency than that in SPWM, which is a significant advantage in terms of lower switching losses and stresses and increased efficiency [48].

3.3.3   System topology choice

Having in mind the description of the two system topologies presented, a final choice has to be made in order to proceed with design of the multi-winding transformer. As it has become evident, the two-stage topology consists of high number of components which will decrease system's reliability. More importantly, this topology will introduce low-order harmonics in the primary transformer currents, therefore a filter is necessary. On the other hand, the single-stage topology can improve the input power factor since only high order harmonics will be present in the transformer currents, which can be suppressed by a suitable choice of a control technique for the VSI boost converters. Considering the advantages of the two-stage configuration, it is chosen as a suggested topology for this application and it will be analyzed further in details.

4 Multi-winding transformer design

4.1 Transformer rated data

Considering the EV dc charging station shown in Figure 18, the common rated power form each single outlet should range from 150 kW to 350 kW [25]. Since the current waveforms will inevitably be distorted due to the rectifier presence, the apparent power necessary to design the transformer should be about 5% higher than the active power required by the load [44]. The transformer primary winding power rating should preferably be smaller than the sum of the power ratings of the secondary windings i.e., smaller than 1102.5 kVA in this case, considering the low probability of simultaneous rated loads on all the secondary windings. However, if all the converters are used to charge vehicles at the same time, the output power can be reduced by employing an overall system controller, which will not permit the total power requested at the secondary side to exceed the primary side rated power [25]. Therefore, considering the IEC standard ratings, the first value lower than the calculated primary apparent power is chosen, i.e., 1000 kVA.

Medium voltage level which the station will most likely be connected to is 10 kV or 20kV. Typically, the primary winding voltage is for at least a factor of 10 higher that the secondary winding voltage. Having in mind the aforementioned reasoning, the multi-winding transformer rated data are summarized in Table 7:

Table 7 Transformer main rated data

Four-winding transformer data	Symbol	Rated value	Unit
Rated active power on the primary winding	P_1	1000	kW
Rated active power on the secondary windings	$P_2=P_3=P_4$	350	kW
Rated power factor	$cos\varphi_n$	1.0	
Rated primary voltage	V_{1n}	20	kV
Rated secondary voltage	V_{2n}	0.4	kV
Rated frequency	f_n	50	Hz
Vector group		Yy	

4.2 Transformer sizing criteria

For a multi-winding transformer, half the arithmetic sum of the rated power values of all the windings (separate windings, not auto-connected) gives a rough estimate of its physical size as compared with a two-winding transformer [51]. The no-load current in percentage is referred to the winding with the highest rated power.

Load losses should be tabulated for all pairs of windings separately, where each pair consists of one primary and one secondary coil. A combined load loss figure for the complete transformer is referred to a specified winding load combination. In general, it is usually not accessible for direct measurement in testing.

Short-circuit impedances for all the different two-winding combinations should be given with the respective reference power values. The tolerance for the short-circuit impedance for a specified first pair of separate windings is ±7.5% of the declared value when the impedance value is ≥10% and ±10% otherwise. For a specified second pair of separate windings, the allowed tolerance is ±10% of the declared value for the principal tapping and ±15% of any other tapping of the pair. For any further pair of windings, the allowed tolerance is ≥15% [51].

Apart from the standard tolerance values provided by the International Electrotechnical Committee (IEC), design recommendations can be summarized based on relevant literature on transformer design, having in mind the multi-winding transformer [52] and its particular application in EV dc fast charging station:

- Low ratio of the window height and width will ensure high leakage reactances, which can limit the current ripples;

- Inter-coil distances to be large enough, i.e. higher than the minimum distances allowed, in order to provide high leakage paths. However, this means that transformer radial size, losses and copper mass will increase;

- High core cross section and high induced voltage per turn lead to low number of turns, which limits the copper losses; although the inductances will decrease;

- Subdivision of the conductors, with complete transposition of the elementary plates;

4.3 Possible coils disposition

Another very important aspect of the transformer design is the coils disposition, since it results in different performances of the transformer itself, which in turn affects the entire system. Some of the possible coil dispositions are shown in Figure 33, where *D* is the column diameter and *W* is the window width [10], [53]. Since the underlying patent for charging stations does not provide any recommendations for the coils arrangement, it seems reasonable to discuss this question further.
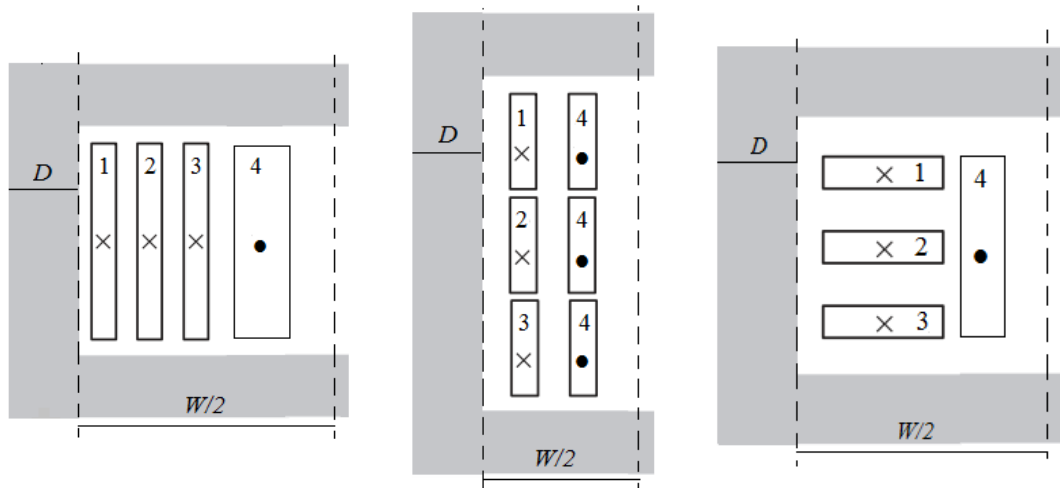
Figure 33 Coils arrangement: a) concentric coils; b) stacked-coil disposition; c) split-stacked secondary arrangement [53]

Concentric arrangement is typical for multi-winding power transformers because it provides ease from manufacturing point of view. In case of four windings, three out of which are rated at low voltage, a sensate disposition is to place the high voltage winding as the most external one due to insulation reasons.

Stacked-coil disposition is commonly found in dry-type traction transformers: the high voltage winding is split in two identical coils which are connected in parallel to the supply network. In this way, as well as with the concentric type, balance of the resultant mmf generated by the winding currents is ensured, which is not the case with split-stacked coils arrangement. Non-identical size and position of the individual coils leads to different flux couplings, which gives rise to unbalanced short-circuit impedances. This unbalance is directly reflected on the behaviuor of the converter system.

4.4 Transformer design procedure

Design procedure followed in this work is rather simple, as shown in Figure 34: starting from the rated apparent power and voltages, a choice is made for the induced voltage per turn, so the number of turns is obtained. In the first stage, high voltage coil is designed in terms of conductor and insulation choice and their arrangement; the same is done for the low voltage coils as well. In the second stage core design is performed by calculating core diameter and lamination stack dimensions. Then geometrical dimensions of the coils are calculated and copper masses. This procedure provides as output basic physical dimensions, as well as information about current densities and core flux density.

INPUT DATA

$S_{1n},\ S_{2n}$ [kVA]
$V_{1n},\ V_{2n}$ [kV]
f [Hz]; Yy

Choose E_{turn} [V] => Number of turns $N_1,\ N_2$

High voltage coil

- Assume g_1 [A/mm2] => wire diameter d_1, cross section S_{cu1}

- Conductor layers, interlayer insulation (paper and axial ducts)

- Electrical and total coil heights and width

- Distance HV coil - yoke

- Column height H

Low voltage coil

- Disposition of elementary conductors N_{rad} x N_{ax}

- Conductor layers, available winding height

- Assume g_2 [A/mm2] => rectangular conductor p_e x q_e

- Interlayer insulation and axial ducts

- Electrical and total coil heights and width

Core

- Assume flux density B_m [T]

- Core cross section coefficients => core diameter d [mm]

- Dimensions of lamination stacks

- Insulation distances: coils to core and between coils

- Core cross section, total dimensions and core mass

HV and LV coils geometry

- External and internal coil diameters

- Average turn length

- Total conductor length

- Coil mass

Figure 34 Basic transformer design flowchart

Although the flowchart in Figure 34 does not show the control points, the procedure is generally iterative: the choices of conductors and their disposition, insulation material and distances, number of core stacks, etc., are revised and adjusted until the requirements for operating current density, flux density, total dimensions, etc. are met.

An optimal design output could be obtained by employing some of the recent computer techniques and methods, such as: genetic programming, Taguchi method, stochastic optimization algorithms, Matlab pattern finder, etc. [54]. However, one should be very precautious when setting up the optimization function: commonly the aim is reducing material costs and increasing transformer efficiency. For multi-winding transformers, being considered as particular devices designed for special purposes, the aforementioned are not always final goals; transformer performances (such as high leakage inductance for improving current waveforms) might arise as design requirements.

4.5   Transformer design solutions

Two preliminary transformer design solutions are obtained following the flowchart in Figure 34 as described in details in Appendix 1 and 2, based on the relevant literature [55] - [63]. In the first solution proposed, concentric coils disposition is chosen and the transformer contains four windings, while in the second solution the high voltage winding is split in three separate coils which are connected in parallel to the supply network, thus a six winding transformer is obtained where the pairs of high and low voltage windings are placed axially on the columns. The cross sections are shown in Figure 35 and the most important basic design outputs are summarized in Table 8 - Table 12.

Table 8 Solution 1: Four coil transformer winding design summary

	Symbol	HV coil	LV coil	Unit
Winding rated apparent power	$S_{1n,\,2n}$	1,000	333.33	kVA
Type of winding		wire	helix	
Number of turns	$N_{1,2}$	693	16	
Induced voltage per turn	E_{turn}	14.0		V/turn
Number of conductor layers	N_l	9	1	
Disposition of elementary conductors	$N_{ax}\,x\,N_{rad}$	/	2 x 2	
Dimensions of elementary conductor	$d_1\,/\,p_e\,x\,q_e$	3.35	7.5 x 5.0	mm
Cross section of bare conductor	$S_{cu1,2}$	8.81	146.56	mm^2
Working current density	$g_{1,2}$	3.28	3.28	A/mm^2
Elementary conductor insulation	$i_{10,20}$	0.129 enameled	0.5 paper	mm
Insulation between conductor layers		6 layers natron paper	/	
Axial duct width	$\delta_{ad1,2}$	4	/	mm
Top / bottom insulation rings height	h_{ir}	24	11	mm
Winding electric height	$h_{1,2,el}$	271	273	mm
Total winding height	$h_{1,2}$	295	295	mm
Total winding width	$a_{1,2}$	39	11	mm
Winding mass	$m_{1,2}$	77.23	19.05; 22.52; 26.0	kg

Table 9 Solution 1: Four coil transformer core design summary

	Symbol	Value	Units
Core diameter	d	231	mm
Net cross section area	$S_{fe,net}$	380.5	cm^2
Working flux density	B_m	1.657	T
Window height	H	375	mm
Column centres distance	l_c	485	mm
Lamination stack lengths	A_i	220 / 210 / 200 / 190 / 180 / 170 / 160 / 140 / 120 / 100 / 70	mm
Lamination stack widths	bi	70.45 / 25.8 / 19.35 / 15.8 / 13.4 / 11.6 / 10.2 / 17 / 13.65 / 10.85 / 12	mm
Total core length / height	$L_c\,x\,H_c$	1190 x 815	mm
Core mass	m_c	1016	kg
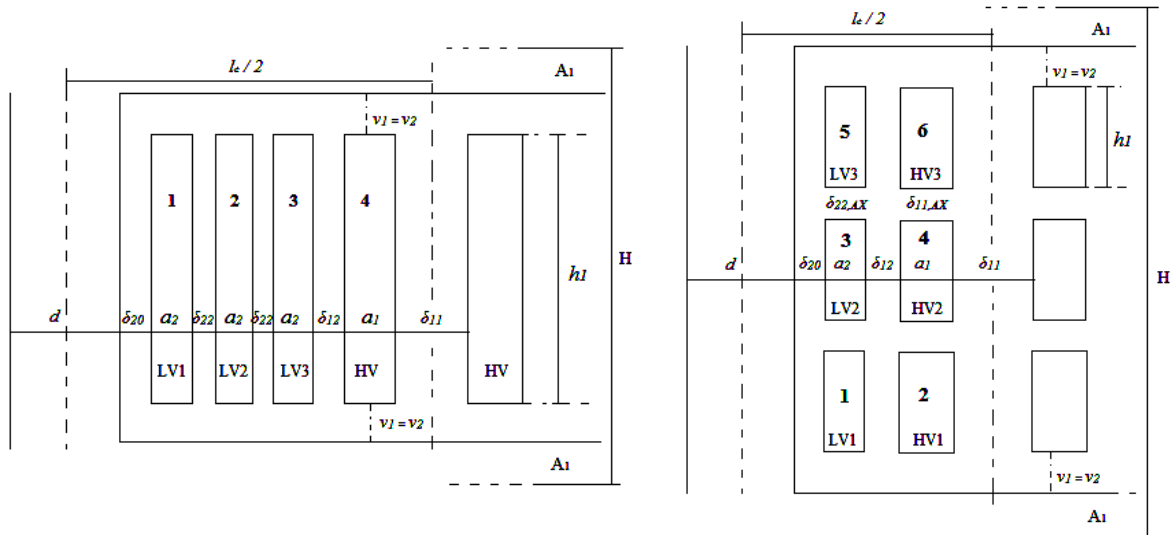
Figure 35 Cross section: four winding transformer (left) and six winding transformer (right)

Table 10 Solution 2: Six coil transformer winding design summary

	Symbol	HV coil	LV coil	Unit
Winding rated apparent power	$S_{1n,\,2n}$	333.33	333.33	kVA
Type of winding		wire	helix	
Number of turns	$N_{1,2}$	1299	30	
Induced voltage per turn	E_{turn}	7.827		V/turn
Number of conductor layers	N_l	15	3	
Disposition of elementary conductors	$N_{ax} \times N_{rad}$	/	2 x 2	
Dimensions of elementary conductor	$d_1 /\ p_e \times q_e$	1.9	7.1 x 5.3	mm
Cross section of bare conductor	$S_{cu1,2}$	2.84	145.85	mm^2
Working current density	$g_{1,2}$	3.39	3.30	A/mm^2
Elementary conductor insulation	$i_{10,20}$	0.112 enameled	0.5 paper	mm
Insulation between conductor layers		5 layers natron paper	0.25 mm DDP	
Top / bottom insulation rings height	h_{ir}	6	11	mm
Axial duct width	$\delta_{ad1,2}$	4	2 x 3	mm
Winding electric height	$h_{1,2,el}$	178	168	mm
Total winding height	$h_{1,2}$	190	190	mm
Total winding width	$a_{1,2}$	38	41	mm
Winding mass	$m_{1,2}$	34.77	30.72	kg

62

Table 11 Solution 2: Six coil transformer core design summary

	Symbol	Value	Units
Core diameter	d	173	mm
Net cross section area	$S_{fe,net}$	209.9	cm^2
Working flux density	B_m	1.68	T
Window height	H	680	mm
Column centres distance	l_c	385	mm
Lamination stack lengths	A_i	170 / 160 / 150 / 140 / 130 / 120 / 100 / 90 / 70	mm
Lamination stack widths	bi	16 / 16.85 / 10.2 / 7.70 / 6.30 / 5.25 / 8.30 / 3.30	mm
Total core length / height	$L_c x H_c$	940 x 1020	mm
Core mass	m_c	630.2	kg

Table 12 Solution 1 and 2: Transformer insulation distances summary

Distance [mm]	Symbol	Interval	4 coils	6 coils
Distance: column – LV winding	δ_{20}	4 - 6	4	5
Distance: LV-LV winding of the same phase	δ_{22}	10 – 14	14	/
Distance LV-HV winding	δ_{12}	14 – 17	14	14
Distance HV-HV winding of the same phase	$\delta_{11,ax}$	≥ 14	/	15
Distance HV-HV winding of different phases	δ_{11}	≥ 14	18	16
Distance LV winding - yoke	v_2	≥ 30	40	40
Distance HV winding - yoke	v_1	≥ 40	40	40

4.6 Four-coil vs. Six-coil design solution: basic comparison

Considering the transformer core in both design proposals, it is obvious that the four-coil solution will be more expensive because it has about 380 kg higher mass than the six-coil core. On the other hand, it will have lower losses per unit mass, since the operating flux density in the first case is significantly lower than in the second one.

Taking into account the fact that copper wires with small diameter are more expensive than the large ones, it is evident that the six-coil solution (d_l=1.9 mm) will cost much more than the four-coil one (d_l=3.35 mm). This is also inevitably imposed by the total amount of copper required for all the high voltage coils: 312 kg in case of six coils versus 232 kg in case

of four coils. Since the current density is chosen to be lower in the four-coil case, this solution is expected to have smaller per unit power losses than the six-coil.

On the other hand, the dimensions of the elementary plate conductors for the low voltage coils are almost the same in both cases. However, the six-coil solution needs about 74 kg more than four-coil solution (276 kg vs. 202 kg).

Having in mind the comparison made above, it is clear that manufacturing cost of six-coil transformer windings will be much higher than in the four-coil solution. This fact will generally determine the transformer price; although the core mass comparison implies an opposite conclusion. However, the choice is not straight-forward: transformer performances have to be evaluated as well as thermal validation before making a final decision.

5   Transformer model and parameters identification

5.1   Four coils transformer model

As explained in Chapter 2, an equivalent single-phase network of a four winding transformer can be established by identifying six independent impedances, which are obtained by six binary short-circuit tests, or calculated analytically based on the transformer geometry. The well-known Starr network presented in Figure 15 is reproduced here for convenience: it is built up of four impedances connected to the external terminals and other two doubled inside the network (Figure 36). The magnetizing branch is neglected.
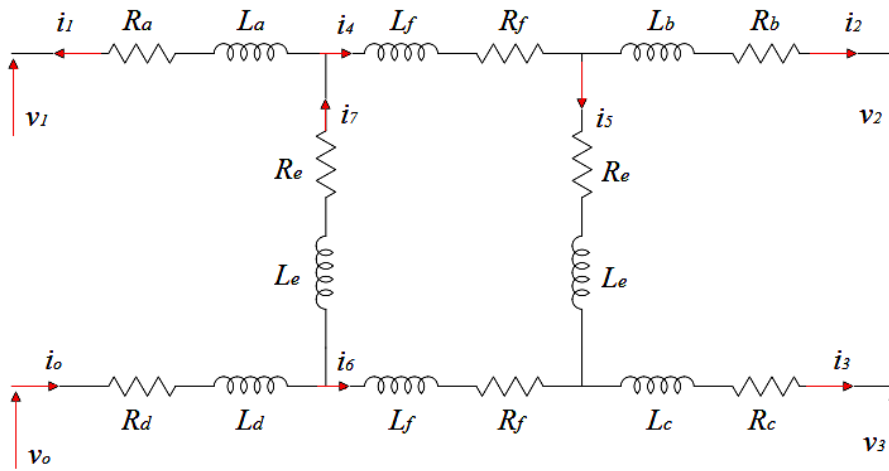
Figure 36 Equivalent Starr network for four winding transformer [52]

The procedure for calculating the parameters of this network (R_i, L_i, $i = a,b,c,d,e,f$) starts with the binary short-circuit impedances. As a first step, binary inductance L_{ij} between each two coils i and j can analytically be determined as:

$$L_{ij} = k_L p_{ij} c_{ij} K_{Rij}, \quad ij : 12, 13, 14, 23, 24, 34 \ , \tag{88}$$

where k_L is a common factor, p_{ij} is the average perimeter of the hollow between the observed coils, c_{ij} is the distance between coils electromagnetic centres and K_{Rij} is the Rogowski factor which models fringing effects. Each of these parameters can be calculated based on the transformer geometry as:

$$k_L = \mu_o \frac{N_2^2}{h_1} \ . \tag{89}$$

$$p_{ij} = 2 \cdot \pi \cdot r_{ij} = 2 \cdot \pi \cdot \left(\frac{D_{i,EXT}}{2} + \frac{\delta_{ij}}{2} \right) \tag{90}$$

$$c_{ij} = \delta_{ij} + \frac{a_i + a_j}{3}. \tag{91}$$

$$K_{R,ij}\left(\sigma_{R,ij}\right) = 1 - \frac{1}{\sigma_{R,ij}}\left(1 - e^{-\sigma_{R,ij}}\right). \tag{92}$$

$$\sigma_{R,ij} = \frac{\pi h}{2\delta_{ij} + a_i + a_j}. \tag{93}$$

$$p_i = 2 \cdot \pi \cdot r_i, \tag{94}$$

where δ_{ij} is the radial distance between the coils, r_i is the distance between the column centre and the middle of the ith coil, r_{ij} is the distance between the column centre and the midpoint of the hollow between coils i and j, a_i and a_j are the coils widths, h_1 is the total height of the coil, N_2 is the number of low voltage turns, $D_{i,EXT}$ is the external diameter of the ith coil. Detailed expressions are given in the Appendix 3 and the final values of the binary inductances are shown in Table 13.

On the other hand, binary short-circuit resistances are used for modelling the main ohmic losses as well as the additional losses in the copper windings. These additional losses are due to skin effect which affects not only the supplied and the short-circuited coil during binary short-circuit test, but also all the other open-ended coils which are immersed in ac leakage field (due to eddy currents). By employing additional loss coefficient k_a these losses are taken into account and the binary resistances can be obtained as:

$$R_{ij} = k_{a,i}R_{\Omega,i} + \sum_{k \neq i,j} k_{ap,k}R_{\Omega,k} + k_{a,j}R_{\Omega,j}, \tag{95}$$

where $R_{\Omega,i}$ is dc resistance of the ith coil and $k_{ap,k}$ is additional loss factor of the kth coil which is open-ended during the binary test and positioned between the coils i and j. Further explanation and detailed expressions can be found in the Appendix 3 and the results are presented in Table 13.

Table 13 Binary short-circuit inductances and resistances

L_{12} [μH]	L_{13} [μH]	L_{14} [μH]	L_{23} [μH]	L_{24} [μH]	L_{34} [μH]
19.014	42.175	72.660	22.472	57.536	36.082
R_{12} [mΩ]	R_{13} [mΩ]	R_{14} [mΩ]	R_{23} [mΩ]	R_{24} [mΩ]	R_{34} [mΩ]
4.277	4.792	3.558	4.992	3.758	3.934

A verification of the analytically calculated binary short-circuit inductances can be done in the Maxwell software by using the FEM method. When employing axisymmetric approach the computations are done with the stored energy in the windings and surrounding air volumes. The transformer geometry should be adapted so as to account for the yoke effect correctly, as shown in Figure 37. Main corrections done to the transformer cross section and the set up parameters are [64]:

- Only one phase is taken into account in order to shorten the computational time;

- The axial distance between the winding and the yoke on each side is increased two to three times;

- The column material is chosen to be pure iron with $\mu_{r,c} = 4000$, therefore the core non-linearity is neglected;

- The yoke is assumed to have relative permeability $\mu_{r,y} = 10^6$;

- Only the high voltage winding is excited by a unity current, which is enough to identify the inductances needed;

- The target energy error is set to be very small (0.05%) because the inductances values will differ in the last decimals;

- The number of turns of each winding is set to be equal to 1 and then obtained values are referred to the low voltage coil number of turns N_2.
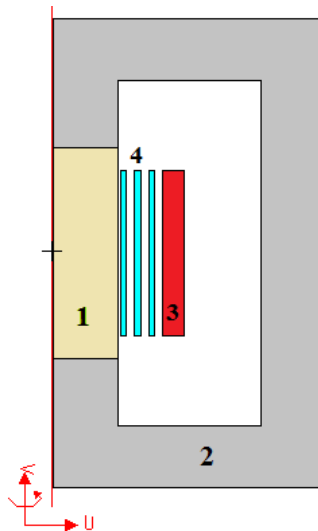
Figure 37 FEM axisymmetric model of the four coil transformer: 1-column, 2-yoke, 3-high voltage winding, 4-low voltage windings

After 25 iteration steps, the results obtained are comparable with the mathematically obtained ones, as shown in Table 14.

Table 14 Binary short-circuit inductances by FEM

L_{12} [μH]	L_{13} [μH]	L_{14} [μH]	L_{23} [μH]	L_{24} [μH]	L_{34} [μH]
17.92	43.52	69.12	20.48	51.20	30.75
ΔL_{12} [%]	ΔL_{13} [%]	ΔL_{14} [%]	ΔL_{23} [%]	ΔL_{24} [%]	ΔL_{34} [%]
-5.75	3.19	-4.87	-8.86	-11.01	-14.86

These discrepancies are due to the fact that each winding in the FEM simulation is taken to be made of solid copper material, i.e., the insulation between conductor layers and axial ducts are not considered.

Having obtained the binary short-circuit inductances and resistances, they are joined to form the binary impedances at mains frequency:

$$\overline{Z_{ij}} = R_{ij} + j\omega L_{ij} \ . \tag{96}$$

Next step is calculating the Starr network impedances from the binary short-circuit impedances by the following equations:

$$\overline{K_1} = \overline{Z_{13}} + \overline{Z_{24}} - \overline{Z_{12}} - \overline{Z_{34}} ; \quad \overline{K_2} = \overline{Z_{13}} + \overline{Z_{24}} - \overline{Z_{14}} - \overline{Z_{23}} \tag{97}$$

$$\overline{Z_e} = \sqrt{\overline{K_1}\,\overline{K_2}} + \overline{K_1} \ . \tag{98}$$

$$\overline{Z_f} = \sqrt{\overline{K_1}\,\overline{K_2}} + \overline{K_2} \ . \tag{99}$$

$$\overline{Z_a} = \frac{1}{2}\left(\overline{Z_{12}} + \overline{Z_{14}} - \overline{Z_{24}} - \frac{\overline{Z_e}\,\overline{Z_f}}{\overline{Z_e} + \overline{Z_f}} \right). \tag{100}$$

$$\overline{Z_b} = \frac{1}{2}\left(\overline{Z_{12}} + \overline{Z_{23}} - \overline{Z_{12}} - \frac{\overline{Z_e}\,\overline{Z_f}}{\overline{Z_e} + \overline{Z_f}} \right). \tag{101}$$

$$\overline{Z_c} = \frac{1}{2}\left(\overline{Z_{23}} + \overline{Z_{34}} - \overline{Z_{24}} - \frac{\overline{Z_e}\,\overline{Z_f}}{\overline{Z_e} + \overline{Z_f}} \right). \tag{102}$$

$$\overline{Z_d} = \frac{1}{2}\left(\overline{Z_{34}} + \overline{Z_{14}} - \overline{Z_{13}} - \frac{\overline{Z_e}\,\overline{Z_f}}{\overline{Z_e} + \overline{Z_f}} \right). \tag{103}$$

Each of the Starr network impedances consists of real and imaginary part, which can be separated in order to identify the equivalent parameters (resistances and inductances) of the network shown in Figure 36. The parameter values are given in Table 15.

$$R_i = \Re e\{\overline{Z_i}\}; \quad L_i = \frac{\Im m\{\overline{Z_i}\}}{2\pi f}, \quad i = a,b,c,d,e,f. \tag{104}$$

Table 15 Equivalent Starr network inductances and resistances at mains frequency

$L_a\,[\mu\mathrm{H}]$	$L_b\,[\mu\mathrm{H}]$	$L_c\,[\mu\mathrm{H}]$	$L_d\,[\mu\mathrm{H}]$	$L_e\,[\mu\mathrm{H}]$	$L_f\,[\mu\mathrm{H}]$
9.922	4.089	-6.638	26.137	58.908	18.873
$R_a\,[\mathrm{m}\Omega]$	$R_b\,[\mathrm{m}\Omega]$	$R_c\,[\mathrm{m}\Omega]$	$R_d\,[\mathrm{m}\Omega]$	$R_e\,[\mathrm{m}\Omega]$	$R_f\,[\mathrm{m}\Omega]$
2.011	2.469	2.557	1.323	0.393	0.054

5.2 Four coils transformer: copper losses estimation

Assuming ideal sinusoidal transformer operation (only fundamental components of the voltages and currents are present) copper losses can be estimated by analyzing the equivalent network of Figure 36. Although eight currents are shown, not all of them are independent, but the following relationships hold:

$$i_7 = i_1 + i_4 \;. \tag{105}$$

$$i_5 = i_4 - i_2 \;. \tag{106}$$

$$i_o' = i_1 + i_2 + i_3 \tag{107}$$

$$i_6 = i_0 - i_7 = i_2 + i_3 - i_4 \tag{108}$$

Current i_4 can be expressed in terms of fundamental components from the equivalent network as a function of i_1, i_2 and i_3 by using the Kirchhoff's voltage low for the internal loop:

$$\overline{I_4} = \frac{1}{2} \cdot \frac{\left(\overline{Z_f} + \overline{Z_e}\right)\cdot \overline{I_2} + \overline{Z_f}\cdot\overline{I_3} - \overline{Z_e}\cdot\overline{I_1}}{\overline{Z_f} + \overline{Z_e}} \tag{109}$$

Referring to a single-phase system as shown in the Starr network, the vectors of variable state currents **i** and state voltage sources can be defined as:

$$\mathbf{i} = \begin{bmatrix} i_1 & i_2 & i_3 & i_4 \end{bmatrix}^T \tag{110}$$

$$\mathbf{v_{io}} = \left[\left(v_0^{'} - v_1 \right) \quad \left(v_0^{'} - v_2 \right) \quad \left(v_0^{'} - v_3 \right) \quad 0 \right]^T \tag{111}$$

The system of state equations in matrix form is:

$$\mathbf{v_{io}} = \mathbf{R_S} \cdot \mathbf{i} + \mathbf{L_S} \cdot \frac{d\mathbf{i}}{dt} \tag{112}$$

where the inductance and the resistance matrices are defined as:

$$\mathbf{L_S} = \begin{bmatrix} L_a + L_e + L_d & L_d & L_d & -L_e \\ L_d & L_b + L_e + L_f + L_d & L_f + L_d & L_e + L_f \\ L_d & L_f + L_d & L_c + L_f + L_d & L_f \\ -L_e & L_e + L_f & L_f & 2\left(L_e + L_f \right) \end{bmatrix} \tag{113}$$

$$\mathbf{R_S} = \begin{bmatrix} R_a + R_e + R_d & R_d & R_d & -R_e \\ R_d & R_b + R_e + R_f + R_d & R_f + R_d & R_e + R_f \\ R_d & R_f + R_d & R_c + R_f + R_d & R_f \\ -R_e & R_e + R_f & R_f & 2\left(R_e + R_f \right) \end{bmatrix} \tag{114}$$

Considering the fundamental components, Eq. (112) can be transformed in a phasor matrix equation:

$$\overline{\mathbf{V_0^{'}}} = \overline{\mathbf{Z_S}} \cdot \overline{\mathbf{I}} + \overline{\mathbf{V_i}} \tag{115}$$

where $\overline{\mathbf{V_0^{'}}}$ is the state vector of the source voltages referred to the low voltage side and it is defined as:

$$\overline{\mathbf{V_0^{'}}} = \left[V_0^{'} \quad V_0^{'} \quad V_0^{'} \quad 0 \right]^T \tag{116}$$

$$V_0^{'} = \frac{V_{1n}}{\sqrt{3}} \cdot \frac{N_2}{N_1} = 266.6 \text{ V} \tag{117}$$

The network impedance matrix $\overline{\mathbf{Z_S}}$ is defined at mains frequency as:

$$\overline{\mathbf{Z_S}} = \mathbf{R_S} + j\omega_1 \mathbf{L_S} = \begin{bmatrix} 3.727 + j29.835 & 1.323 + j8.211 & 1.323 + j8.211 & -0.393 - j18.507 \\ 1.323 + j8.211 & 4.239 + j33.931 & 1.377 + j14.140 & 0.447 + j24.436 \\ 1.323 + j8.211 & 1.377 + j14.140 & 3.934 + j12.055 & 0.054 + j5.929 \\ -0.393 - j18.507 & 0.447 + j24.436 & 0.054 + j5.929 & 0.894 + j48.871 \end{bmatrix} \tag{118}$$

A reference operating condition for the system should be identified: one possibility is to choose equal impedance (in module and phase) connected at each secondary terminal. This condition corresponds to assuming the same battery charging conditions on all the secondary

ports. Choosing the value of this load impedance is not a trivial issue, since the battery internal parameters depend on its state of charge, temperature, etc., and moreover, they are not constant during the charging process. Another possibility is to assume that all the secondary coils are loaded with rated current; however having in mind that balancing the load is not a necessary requirement. In this case the secondary currents are assumed to be equal in magnitude and phase:

$$\overline{I_1} = \overline{I_2} = \overline{I_3} = \overline{I_{sec,n}} = 481.12 \cdot e^{-j\varphi} \quad \text{A}, \tag{119}$$

where the phase angle of the secondary currents φ=arcos (PF) is equal to the phase angle of the primary current, which in turn equals the phase angle of the supply voltage. In this way a unity power factor is ensured. Also the primary transformer current in this conditions will equal its rated value. The system (115) can now be solved for the transformer output terminal voltages:

$$\begin{bmatrix} \overline{V_1} \\ \overline{V_2} \\ \overline{V_3} \\ 0 \end{bmatrix} = \begin{bmatrix} V_0^{'} \\ V_0^{'} \\ V_0^{'} \\ 0 \end{bmatrix} - \mathbf{Z_s} \cdot \begin{bmatrix} \overline{I_1} \\ \overline{I_2} \\ \overline{I_3} \\ \overline{I_4} \end{bmatrix} \tag{120}$$

By solving the Eq. (109), the following values for the secondary currents are obtained:

$$\overline{V_1} = 264.32 \cdot e^{-j4.36^0} \text{ V}; \quad \overline{V_2} = 264.93 \cdot e^{-j6.49^0} \text{ V}; \quad \overline{V_3} = 263.97 \cdot e^{-j3.75^0} \text{ V}. \tag{121}$$

These values will be useful for the later analysis of the transformer operation in non-sinusoidal conditions.

Total copper losses can now be estimated for sinusoidal conditions at mains frequency:

$$P_{Cu} = 3 \cdot \left(R_a I_1^2 + R_b I_2^2 + R_c I_3^2 + R_d I_0^2 + R_e I_5^2 + R_e I_7^2 + R_f I_4^2 + R_f I_6^2 \right) = 13.85 \text{ kW} \tag{122}$$

5.3 Six coils transformer model

In case of a six coil transformer, obtaining Starr equivalent network is a cumbersome and impractical task; therefore employing a mesh network which consists of 15 independent impedances as shown in Figure 16 (and reproduced for convenience here in Figure 38) can be analyzed. In order to calculate branch impedances of this network (Z_{ij}), which cannot be related to any physical parts of the transformer, binary short-circuit inductances and resistances are necessary to be measured or calculated analytically.
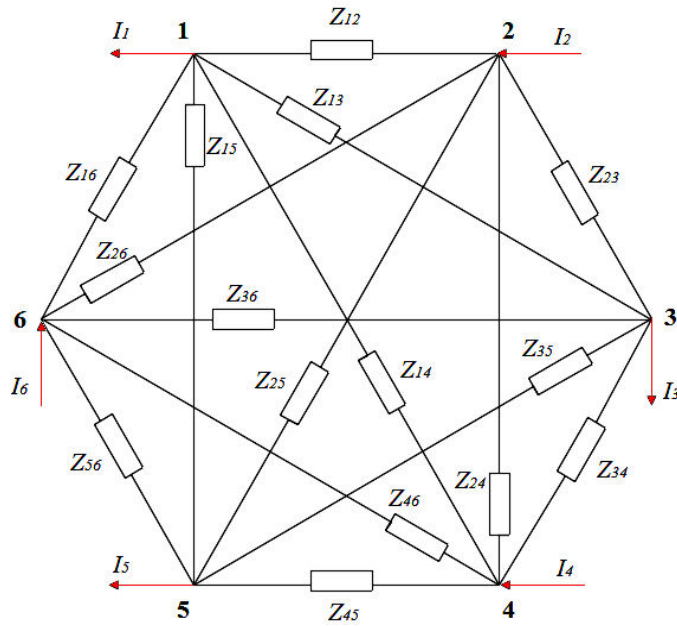
Figure 38 Equivalent mesh network of six winding transformer

As it is well-known, binary short-circuit inductances can be measured for each pair of coils *ij* in the following manner: winding *i* is excited with rated current while winding *j* is short-circuited and all the other coils are open-ended. Since experimental measurements are not possible to be performed in the transformer design phase, analytical approach has to be adopted. Calculating directly the binary short-circuit inductance for a pair of coils is very intricate, therefore a simplified procedure is followed, by subdividing the leakage flux in two components, axial and radial as shown in Figure 39. Their effects are taken into account by the inductances L_{ij}^r and L_{ij}^z which made up the binary short-circuit inductance [65].
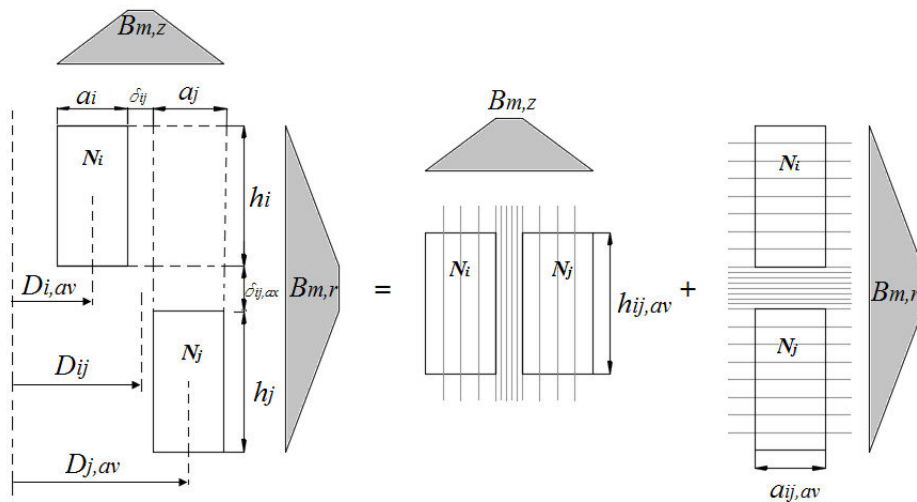
Figure 39 Flux density in radial and axial direction in the transformer window [65]

$$L_{ij} = \sqrt{\left(L_{ij}^z\right)^2 + \left(L_{ij}^r\right)^2} \qquad (123)$$

Assuming the coils are concentric with equal heights, the leakage flux has only one component in the axial direction. Therefore, the axial contribution L_{ij}^z to the binary short-circuit inductance is:

$$L_{ij}^z = \underbrace{\frac{\mu_o \pi N_o^2}{\left(h_i + h_j\right)/2}}_{K_{Rog}^z} \left(\frac{a_i D_{i,AV}}{3} + \delta_{ij} D_{ij,AV} + \frac{a_j D_{j,AV}}{3} \right) , \qquad (124)$$

where h_i and h_j are coils heights, $D_{i,AV}$ and $D_{j,AV}$ are coils average diameters, a_i and a_j are coils widths, $D_{ij,AV}$ is the diameter of the hollow between the coils, δ_{ij} is the radial distance between the coils, N_o is the reference number of turns. Referring to the six coil transformer, the coil pairs are obtained for: $i = 1, 3, 5$ and $j = 2, 4, 6$.

Assuming the windings have equal diameters, and the leakage flux has only one component in radial direction, L_{ij}^r can be calculated as:

$$L_{ij}^r = \underbrace{\frac{\mu_o \pi N_o^2 D_{ij,AV}}{\left(a_i + a_j\right)/2}}_{K_{Rog}^r} \left(\frac{a_i}{3} + \delta_{ij,ax} + \frac{a_j}{3} \right), \qquad (125)$$

where $\delta_{ij,ax}$ is the axial distance between the observed coils. Referring to the six coil transformer, the coil pairs are obtained for: $i = 1, 2$ and $j = 3, 4, 5, 6$; and for $i = 3, 4$ and $j = 5, 6$. Detailed expressions for calculating binary short-circuit inductances are given in Appendix 4 and the results are shown in Table 16.

Following the same procedure as in the case of four winding transformer for calculating the binary short-circuit resistances and taking into account additional copper losses by coefficient k_a is explained in Appendix 4 and the values obtained are given in Table 17.

Table 16 Six coil transformer binary short-circuit inductances at mains frequency

L_{12} [μH]	L_{13} [μH]	L_{14} [μH]	L_{15} [μH]	L_{16} [μH]	L_{23} [μH]	L_{24} [μH]	L_{25} [μH]	L_{26} [μH]
173.83	77.83	225.21	53.09	198.19	225.21	103.50	198.19	70.42
L_{34} [μH]	L_{35} [μH]	L_{36} [μH]	L_{45} [μH]	L_{46} [μH]	L_{56} [μH]			
173.83	77.83	225.21	225.21	103.50	173.83			

Table 17 Six coil transformer binary short-circuit resistances at mains frequency

R_{12} [mΩ]	R_{13} [mΩ]	R_{14} [mΩ]	R_{15} [mΩ]	R_{16} [mΩ]	R_{23} [mΩ]	R_{24} [mΩ]	R_{25} [mΩ]	R_{26} [mΩ]
8.999	7.735	8.999	7.735	8.999	8.999	10.263	8.999	10.263

R_{34} [mΩ]	R_{35} [mΩ]	R_{36} [mΩ]	R_{45} [mΩ]	R_{46} [mΩ]	R_{56} [mΩ]
8.999	7.735	8.999	8.999	10.263	8.999

From the previous values, binary short-circuit impedance between each two coils i and j can be calculated by Eq. (126). Due to the windings symmetry, it is evident that some of these binary impedances are equal.

$$\overline{Z_{sc,ij}} = R_{ij} + j\omega L_{ij}, \tag{126}$$

$$\overline{Z_{sc,12}} = \overline{Z_{sc,34}} = \overline{Z_{sc,56}}; \quad \overline{Z_{sc,13}} = \overline{Z_{sc,35}}; \quad \overline{Z_{sc,24}} = \overline{Z_{sc,26}};$$

$$\overline{Z_{sc,14}} = \overline{Z_{sc,23}} = \overline{Z_{sc,36}} = \overline{Z_{sc,45}}; \quad \overline{Z_{sc,16}} = \overline{Z_{sc,25}}. \tag{127}$$

As explained in 2.3 and referring to Figure 38, a full admittance matrix Y_N which contains the branch admittances between each pair of nodes of the mesh network can be created. Taking out the first row and column, which refer to primary coil supplied by the network, the system is reduced to 5th order:

$$\left[\overline{V}\right] = \left[\overline{Z}\right] \cdot \left[\overline{I}\right] = \left[\overline{Y}\right]^{-1} \cdot \left[\overline{I}\right], \tag{128}$$

where the matrix containing mesh network impedances has the following shape [18]:

$$\overline{Z} = \begin{bmatrix} a_{22} & a_{23} & a_{24} & a_{25} & a_{26} \\ a_{23} & a_{33} & a_{34} & a_{35} & a_{36} \\ a_{24} & a_{34} & a_{44} & a_{45} & a_{46} \\ a_{25} & a_{35} & a_{45} & a_{55} & a_{56} \\ a_{26} & a_{36} & a_{46} & a_{56} & a_{66} \end{bmatrix}, \tag{129}$$

General expressions for calculating its diagonal and off-diagonal elements from the binary short-circuit impedances are:

$$a_{ii} = \overline{Z_{sc,1i}},$$

$$a_{ij} = \frac{1}{2}\left(\overline{Z_{sc,1i}} + \overline{Z_{sc,1j}} - \overline{Z_{sc,ij}}\right). \tag{130}$$

Provided that the impedance matrix Z is invertible, $Y=Z^{-1}$ is the mesh network admittance matrix, with the following shape:

$$\overline{Y} = \left[\overline{Z}\right]^{-1} = \begin{bmatrix} b_{22} & b_{23} & b_{24} & b_{25} & b_{26} \\ b_{23} & b_{33} & b_{34} & b_{35} & b_{36} \\ b_{24} & b_{34} & b_{44} & b_{45} & b_{46} \\ b_{25} & b_{35} & b_{45} & b_{55} & b_{56} \\ b_{26} & b_{36} & b_{46} & b_{56} & b_{66} \end{bmatrix}.$$
(131)

Therefore, mesh network impedance between nodes i and j is calculated by using Y-matrix elements as:

$$\overline{Z_{ij}} = -\frac{1}{b_{ij}}, \quad \text{for } i \neq 1, j \neq 1; \qquad \overline{Z_{1i}} = \frac{1}{b_{ii} + \sum_{\substack{j \neq 1, j \neq i, \\ i \neq 1}} b_{ij}}.$$
(132)

Detailed expressions can be found in the Appendix 4. The parameters of mesh network at mains frequency obtained analytically by this method are given in Table 18 (in mΩ), and the mesh resistances and inductances can be separated as well. Their values are given in Table 19 and Table 19.

Table 18 Six coil transformer mesh network impedances at mains frequency

$\overline{Z_{12}} = 26.878 + j23.098$	$\overline{Z_{13}} = 17.639 + j27.961$
$\overline{Z_{14}} = -54.122 - j41.384$	$\overline{Z_{15}} = 13.354 + j20.558$
$\overline{Z_{16}} = -100.93 - j25.364$	$\overline{Z_{23}} = -53.619 + j41.417$
$\overline{Z_{24}} = 24.521 + j37.820$	$\overline{Z_{25}} = \overline{Z_{16}}$
$\overline{Z_{26}} = 18.201 + j27.469$	$\overline{Z_{34}} = 19.823 + j20.892$
$\overline{Z_{35}} = \overline{Z_{13}}; \quad \overline{Z_{36}} = \overline{Z_{23}}$	$\overline{Z_{45}} = \overline{Z_{14}}; \quad \overline{Z_{46}} = \overline{Z_{24}}$
$\overline{Z_{56}} = \overline{Z_{12}}$	

Since primary coils 2, 4 and 6 are connected in parallel to the same supply grid, the same potential on these nodes is ensured; however it does not prevent from circulating currents between them.

Table 19 Six coil transformer mesh network resistances at mains frequency

R_{12} [mΩ]	R_{13} [mΩ]	R_{14} [mΩ]	R_{15} [mΩ]	R_{16} [mΩ]	R_{23} [mΩ]	R_{24} [mΩ]	R_{25} [mΩ]	R_{26} [mΩ]
26.878	17.639	-54.122	13.354	-100.925	-53.619	24.521	-100.925	18.201
R_{34} [mΩ]	R_{35} [mΩ]	R_{36} [mΩ]	R_{45} [mΩ]	R_{46} [mΩ]	R_{56} [mΩ]			
19.823	17.639	-53.619	-54.122	24.521	26.878			

Table 20 Six coil transformer mesh network inductances at mains frequency

L_{12} [μH]	L_{13} [μH]	L_{14} [μH]	L_{15} [μH]	L_{16} [μH]	L_{23} [μH]	L_{24} [μH]	L_{25} [μH]	L_{26} [μH]
73.523	89.003	-131.730	65.439	-80.345	-131.836	120.386	-80.345	87.436

L_{34} [μH]	L_{35} [μH]	L_{36} [μH]	L_{45} [μH]	L_{46} [μH]	L_{56} [μH]
66.500	89.003	-131.836	-131.836	120.386	73.523

Having negative values of the resistances and inductances in the mesh network is not an oddity since they cannot be assigned to any physical parts of the transformer. In order to calculate the copper losses at mains frequency, all the branch currents should be determined. The network is solved by node potential method taking node 2 as a reference. The admittance matrix has the following shape:

$$
\overline{\mathbf{Y}_{\mathbf{S}}} = \begin{bmatrix} Y_{11} & -Y_{13} & -Y_{14} & -Y_{15} & -Y_{16} \\ -Y_{13} & Y_{33} & -Y_{34} & -Y_{35} & -Y_{36} \\ -Y_{14} & -Y_{34} & Y_{44} & -Y_{45} & -Y_{46} \\ -Y_{15} & -Y_{35} & -Y_{45} & Y_{55} & -Y_{56} \\ -Y_{16} & -Y_{36} & -Y_{46} & -Y_{56} & Y_{66} \end{bmatrix}
\tag{133}
$$

where its elements are calculated as:

$$
\overline{Y_{ij}} = \frac{1}{\overline{Z_{ij}}}; \quad \overline{Y_{ii}} = \sum_j \frac{1}{\overline{Z_{ij}}}
\tag{134}
$$

Having in mind that the transformer is supplied at nodes 2, 4 and 6 and node 2 was chosen as a reference one, the system equation in matrix form can be written as:

$$
\overline{\mathbf{I}} = \overline{\mathbf{Y}_{\mathbf{S}}} \cdot \overline{\mathbf{V}} \;\Rightarrow\; \overline{\mathbf{V}} = \overline{\mathbf{Y}_{\mathbf{S}}^{-1}} \cdot \overline{\mathbf{I}}
\tag{135}
$$

$$
\begin{bmatrix} \overline{V_1} - \overline{V_2} \\ \overline{V_3} - \overline{V_2} \\ \overline{V_4} - \overline{V_2} \\ \overline{V_5} - \overline{V_2} \\ \overline{V_6} - \overline{V_2} \end{bmatrix} = \left[\overline{\mathbf{Z}_{\mathbf{S}}} \right] \cdot \begin{bmatrix} -\overline{I_1} \\ -\overline{I_3} \\ \overline{I_4} \\ -\overline{I_5} \\ \overline{I_6} \end{bmatrix}
\tag{136}
$$

The supply voltage referred to the low voltage side is:

$$
\overline{V_2'} = \overline{V_4'} = \overline{V_6'} = V_0' = \frac{V_{1n}}{\sqrt{3}} \cdot \frac{N_2}{N_1} = 266.67 \text{ V}
\tag{137}
$$

In order to solve the network and ensure coherent procedure with the four-coil transformer case, rated secondary currents will be assumed, all equal in magnitude and phase among them, and in phase with the primary currents as well, so as to impose a condition on unity power factor.

$$\overline{I_1} = \overline{I_3} = \overline{I_5} = \overline{I_{sec,n}} = 481.12 \cdot e^{j0} \text{ A} \tag{138}$$

$$\overline{I_2'} = \overline{I_4'} = \overline{I_6'} = \overline{I_{prim,n}'} = 416.55 \cdot e^{j0} \text{ A} \tag{139}$$

Equation (136) can now be written as:

$$\begin{bmatrix} \overline{V_1} \\ \overline{V_3} \\ 0 \\ \overline{V_5} \\ 0 \end{bmatrix} = \begin{bmatrix} \overline{Z_s} \end{bmatrix} \cdot \begin{bmatrix} -\overline{I_1} \\ -\overline{I_3} \\ \overline{I_4} \\ -\overline{I_5} \\ \overline{I_6} \end{bmatrix} + \begin{bmatrix} V_0' \\ V_0' \\ 0 \\ V_0' \\ 0 \end{bmatrix} \tag{140}$$

Solving the system results in obtaining the three unknown output terminal voltages:

$$\overline{V_1} = 270.43 \cdot e^{-j14.61^0} \text{ V} ; \quad \overline{V_3} = 270.80 \cdot e^{-j14.91^0} \text{ V} ; \quad \overline{V_5} = 270.61 \cdot e^{-j14.77^0} \text{ V} . \tag{141}$$

It can be noted that although the same currents flow through all the secondary windings, phase voltages at these nodes are not exactly equal. Now it is possible to calculate all the branch currents as:

$$\overline{I_{ij}} = \frac{\overline{V_i} - \overline{V_j}}{\overline{Z_{ij}}} \tag{142}$$

Total copper losses at mains frequency are:

$$P_{Cu} = 3 \cdot \left(R_{12} I_{12}^2 + R_{13} I_{13}^2 + ... + R_{56} I_{56}^2 \right) = 20.02 \text{ kW} \tag{143}$$

It is not surprising to obtain higher copper losses in sinusoidal conditions with respect to the four-coil case, due to the fact that the amount of copper used in the former case is significantly higher.

5.4 Core losses estimation

Another important part of the transformer design is estimation of the core losses at reference sinusoidal conditions, as well as at distorted waveforms operation. Considering no-load condition, specific core losses due to hysteresis and eddy currents can be evaluated

separately. Using the curves for core losses provided by the manufacturer (Figure 40) at two different frequencies (typically 50 Hz and 60 Hz), the specific losses per unit mass at variable frequency and at variable flux density peak value at sinusoidal conditions are calculated as:

$$p_{Fe,h}(B,f) = C_h \cdot \frac{f}{f_{ref}} \cdot \left(\frac{B}{B_{ref}}\right)^2 \tag{144}$$

$$p_{Fe,ec}(B,f) = C_{ec} \cdot \left(\frac{f}{f_{ref}}\right)^2 \cdot \left(\frac{B}{B_{ref}}\right)^2, \tag{145}$$

where C_h and C_{ec} are specific hysteresis and eddy current loss at the reference values for B_{ref} and f_{ref} (usually 1 T, 50 Hz) respectively. It should be noted that these expressions are valid only when the working frequency is low and minor hysteresis loops are neglected.

Total specific core losses per unit mass are sum of the hysteresis and eddy current losses:

$$p_{Fe}(B,f) = \left[C_h \cdot \frac{f}{f_{ref}} + C_{ec} \cdot \left(\frac{f}{f_{ref}}\right)^2\right] \cdot \left(\frac{B}{B_{ref}}\right)^2. \tag{146}$$

If $f = f_{ref}$ and $B = B_{ref}$, the total specific loss is known as loss figure (C_{Fe}) and can be read directly from the manufacturer's curve. By analyzing the properties of various lamination materials, it has been found that the hysteresis losses are about 2/3 of the total iron losses at reference frequency, i.e.:

$$C_{Fe} = C_h + C_{ec} \quad \Rightarrow \quad \frac{C_h}{C_{Fe}} = 0.6 \div 0.8. \tag{147}$$
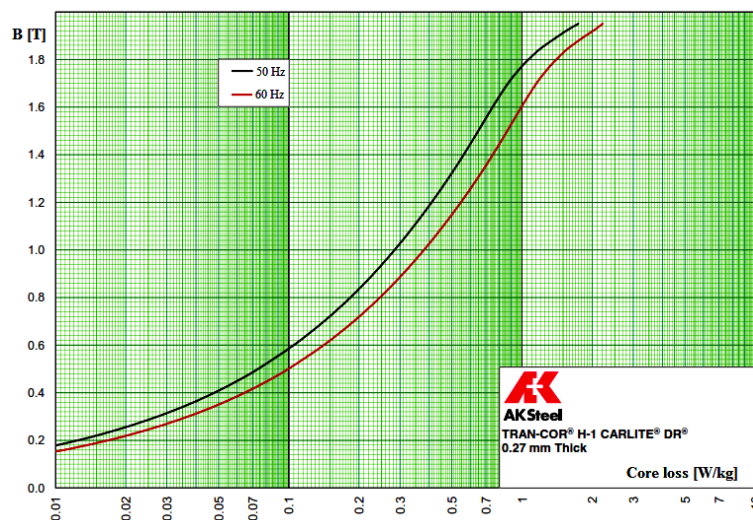
Figure 40 Specific core loss for H-1 Carlite 0.27 mm core laminations [63]

In order to calculate total core losses, an additional coefficient is introduced, $k_{a,tec}$, which takes into account the loss increase due to technological effects such as: non-uniform flux density distribution near the core joints, lamination burrs, material mechanical stress, etc. The value of this coefficient depends on the manufacturing process and on the laminations quality. A typical value can be assumed $k_{a,tec} \approx 1.15 - 1.20$. Therefore, total core losses are:

$$P_{Fe} = k_{a,tec} \cdot p_{Fe}(B, f) \cdot m_{core}. \tag{148}$$

Analyzing the core losses in Figure 40, the loss profile is $C_{Fe} = 0.28$ W/kg. By assuming the loss ratio to equal $C_h / C_{Fe} = 0.8$, it is found that specific losses are: $C_h = 0.224$ W/kg and $C_{ec} = 0.056$ W/kg. Therefore, total core loss estimation for both four and six coil transformers at rated sinusoidal conditions is shown in Table 21.

Table 21 Core losses estimation in sinusoidal conditions at mains frequency

	4 coils	**6 coils**	**Unit**
Operating flux density	1.657	1.680	T
Hysteresis core losses	0.6150	0.6322	W/kg
Eddy currents core losses	0.1538	0.1581	W/kg
Total core mass	1016	630.2	kg
Total core losses	**898.27**	**572.75**	**W**

Summing up the copper and the core losses calculated previously, the transformer efficiency can be estimated at rated sinusoidal conditions. For the four coil transformer it is $\eta=98.53\%$, and for the six coil its value is $\eta=97.94\%$, which is unacceptably low for transformer operation in ideal conditions. Having in mind the ease of obtaining the parameters of the equivalent network for both cases, although both the procedures are based on classical analytical approach and do not impose particular computational complexity, the four coil transformer is however superior and less prone to errors. Therefore, the four coil design proposal will be analyzed further in the following chapter.

6 Transformer performances estimation

In order to estimate more precisely the transformer performances in the specific application for EV dc charging stations, the proposed single-stage topology should be considered and the influence of the harmonic components to be taken into account. By analyzing the equivalent Starr network parameters as a function of the frequency several observations can be made:

- Leakage inductances estimated from the binary short-circuit impedances are not frequency dependent;
- Resistance values vary with the frequency as shown in Table 22 (always referring to the low voltage side):

Table 22 Starr network resistances as a function of the harmonic order

R_{ih} [mΩ]	R_{ah}	R_{bh}	R_{ch}	R_{dh}	R_{eh}	R_{fh}
$h = 0$	1.917	2.268	2.618	1.152	0	0
$h = 1$	2.011	2.469	2.557	1.323	0.393	0.054
$h = 10$	9.690	4.660	-2.363	16.711	32.530	4.472
$h = 100$	56.631	20.221	-28.053	253.001	219.954	30.309
$h = 1000$	176.70	63.44	-86.84	742.43	685.13	94.57

- Dc coil resistances $R_{a\Omega}$, $R_{b\Omega}$, $R_{c\Omega}$ and $R_{d\Omega}$ are given as R_{ah}, R_{bh}, R_{ch} and R_{dh};
- The ac resistances at fundamental frequency are very close to the dc values respectively: R_{a1}, R_{b1}, R_{d1} are slightly higher than $R_{a\Omega}$, $R_{b\Omega}$, $R_{d\Omega}$, while R_{c1} is slightly lower than $R_{c\Omega}$;
- The increasing trend of R_{a1}, R_{b1} can be observed further at higher frequencies, R_{d1} increases too, although much more rapidly, while R_{ch} changes its sign.

It can be shown that regardless of the significant increase in the Starr network resistances with the frequency increase, generally the network reactances will have dominant values. Therefore, in order to simplify the further analysis, without losing much on the solution accuracy, the values of the resistances at fundamental frequency R_{i1} will be considered.

In order to estimate the transformer performances taking into account the VSI boost rectifier influence on the secondary currents and considering the effects of multiple secondary windings, the following steps will be performed:

- Fourier decomposition of the converter input voltage (for each converter separately);
- Starr equivalent network harmonic impedances;

- Network harmonic currents and THD$_I$;
- Copper and core harmonic losses estimation;
- Transformer efficiency calculation.

The steps listed above are to be repeated for each harmonic separately, except the transformer efficiency which is estimated globally. Then by adding harmonic instantaneous current components, the currents waveforms in time domain will be obtained.

Considering a reference case of rated secondary currents transformer performances will be analyzed when different VSI boost converter control techniques are applied. This analysis is aimed at identifying the most suitable PWM technique in terms of transformer efficiency and the lowest harmonic distortion of the transformer primary current.

As it is well-known, converter switching action results in generation of high order harmonics, due to the high switching frequency in the order of kHz. Since this phenomenon is inevitable, there are some possibilities for suppressing specific harmonics and therefore decreasing the current total harmonic distortion. This is particularly interesting in the case of multiple secondary transformer windings, which feed separate VSI rectifiers.

Assuming the voltage drop caused by the connection inductance (due to the presence of cables which are connecting each transformer output terminal with the converter) is negligible, it can be considered that the voltage at the transformer output consists of fundamental component and high order harmonics [66]:

$$v_i(t) = m_{a,i} \frac{V_{dc,i}}{2} \sin(\omega_{1c} t) + v_{h,tot,i} \quad i = 1, 2, 3,$$ (149)

where m_a is the modulation ratio, ω_{1c} is the angular frequency of the fundamental component (equal to the angular frequency of the control sinusoidal signal, 50 Hz), $V_{dc,i}$ is the dc output voltage, $v_{h,tot,i}$ is the total high order harmonic content of the output voltage and i indicates the transformer secondary terminal. The typical PWM converter voltage spectrum can be determined as:

$$v_{h,tot,i}(t) = \frac{2V_{dc,i}}{\pi} \sum_{q=1,2,\ldots}^{\infty} \frac{1}{q} \cdot \left\{ \sum_{k=\pm1,\pm3,\ldots}^{\infty} J_k\left(\frac{qm_a\pi}{2}\right) \cdot \sin\left[(q+k)\frac{\pi}{2}\right] \sin\left[(qm_f + k)\omega_{1c}t\right] \right\},$$ (150)

where $J_k(x)$ is the value of the Bessel's function of first type of order k evaluated at x and m_f is the frequency modulation index.

The waveform of each voltage harmonic component of order h can be calculated as:

$$v_{h,i}(q,k) = A_{q,k} \sin\left[h\omega_{1c}(t - t_d)\right],$$

(151)

where $A_{q,k}$ is the harmonic amplitude, t_d is a time delay due to the phase shift between the output voltages as well as due to the phase-shift of the carrier signal with respect to the phase of another carrier signal taken as a reference. The harmonic amplitude is:

$$A_{q,k} = \frac{2V_{dc,i}}{\pi} \frac{1}{q} J_k\left(\frac{qm_a\pi}{2}\right) \cdot \sin\left[(q+k)\frac{\pi}{2}\right],$$

(152)

and the harmonic order is represented as a function of the frequency modulation index:

$$h = q \cdot m_f + k,$$

(153)

where $q + k$ has to be odd, therefore if $q = 1$, $k = \pm 2, \pm 4$; if $q = 2$, $k = \pm 1, \pm 5$, etc. Harmonic components $2 \cdot m_f \pm 3$ do not exist in case of three phase PWM converters due to the phase shift of 120° between the reference sinusoidal signals which are controlling the modulation of each converter leg, i.e., of each phase [67].

6.1 Carrier-phase shifting method

In case of n converters which are controlled simultaneously by sinusoidal PWM, it has been shown that improved performances in terms of cancelling harmonic components in the transformer input waveforms can be achieved if the so called carrier phase-shifting method is applied. It means that in case of a three phase system and bipolar switching, each converter is controlled by a triangular carrier signal shifted for T_{sw}/n with respect to its neighbouring converter. The same modulating (reference) signal is used, as shown in Figure 41.
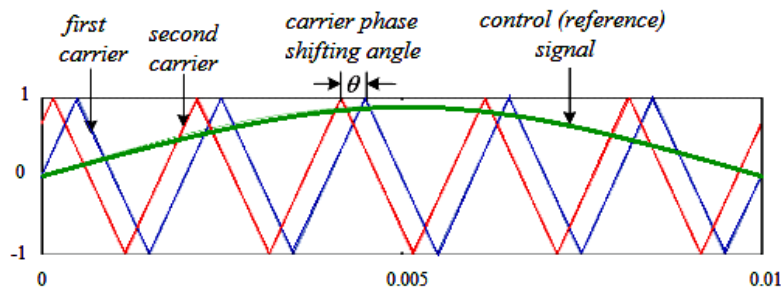
Figure 41 Principle of carrier phase-shifting method [68]

The phase shift between the carrier signals implies a displacement in the instantaneous secondary voltages, which in turn causes large current harmonics at m_f and its multiples. This phase shift in the formula (151) is represented as a contribution to the time delay t_d. A reasonable expectation when applying this method is to introduce larger distortion in the

secondary side currents with respect to the case of co-phased signals, but at the same time to lower the harmonic distortion of the primary current.

In the preliminary analysis it is assumed that no filter is inserted between the transformer output and the converter input. In fact, the need for such a filter depends on the analysis results. The ripples of the converter output dc voltage will be neglected, and the supply grid voltage is considered to be purely sinusoidal. It is referred to the low voltage side as:

$$v_o'(t) = V_o' \cdot \sin(\omega_{1c}t) = \frac{V_{1n}}{\sqrt{3}} \cdot \frac{N_2}{N_1} \cdot \sin(\omega_{1c}t). \tag{154}$$

Following the same procedure as in the case of sinusoidal conditions, the system state equation can be written in matrix form:

$$\mathbf{v_{io}} = \mathbf{R_S} \cdot \mathbf{i} + \mathbf{L_S} \cdot \frac{d\mathbf{i}}{dt}. \tag{155}$$

$$\begin{bmatrix} v_o' \\ v_o' \\ v_o' \\ 0 \end{bmatrix} = (\mathbf{R_S} + jh\omega_{1c}\mathbf{L_S}) \cdot \begin{bmatrix} i_{1h} \\ i_{2h} \\ i_{3h} \\ i_{4h} \end{bmatrix} + \begin{bmatrix} v_{1h} \\ v_{2h} \\ v_{3h} \\ 0 \end{bmatrix}, \tag{156}$$

where the transformer impedance matrix is defined in the same manner as Eq. (113) and (114) and the secondary voltages are calculated according to Eq. (149). Now by solving the Eq. (156) at each harmonic frequency, the waveforms of the transformer secondary currents can be obtained, and then also the primary current by using the Kirchhoff's law. It should be noted that the supply voltage $v_0' = 0$ except at mains frequency and for the transformer network resistances are taken their values at fundamental frequency.

A few variations of the modulation parameters are investigated and current harmonic distortion, copper losses and transformer efficiency are calculated for each case. Two frequency ratios are imposed, $m_f = 99$ and $m_f = 33$, corresponding to switching frequencies (equal to the carrier signal frequency) 4.95 kHz and 1.65 kHz respectively. The effect of the carrier phase shift is also tested, taking the carrier signals for each converter to be co-phased or phase-shifted by $T_{sw}/3$. The dc-link voltage is fixed at 800 V.

6.2 Case 1: $m_f = 99$, co-phased carrier signals

The fundamental and the main current harmonic values are shown in Table 23, as well as the total current harmonic distortion and total copper losses estimated when the three carrier

signals for each converter are in phase. Current waveforms are synthesized by summing up the sinusoidal harmonic components obtained by Fourier analysis and are shown in Figure 42 and Figure 43. Total copper losses at each harmonic frequency are given in Figure 44.

Table 23 Current fundamental and high order harmonics and copper losses in case of co-phased carrier signals and frequency ratio $m_f = 99$

Current	i_1	i_2	i_3	i_0'
$I_{fund,rms}$ [A]	481.12	481.12	481.12	1,443.36
$h = m_f - 2$ [%]	2.04	1.79	20.62	7.22
$h = m_f + 2$	1.96	1.71	19.80	6.94
$h = 2m_f - 1$	0.87	0.81	8.39	2.89
$h = 2m_f + 1$	0.86	0.80	8.31	2.87
THD_I [%]	3.31	2.93	33.04	11.54
$P_{Cu,tot}$ [kW]	14.16			
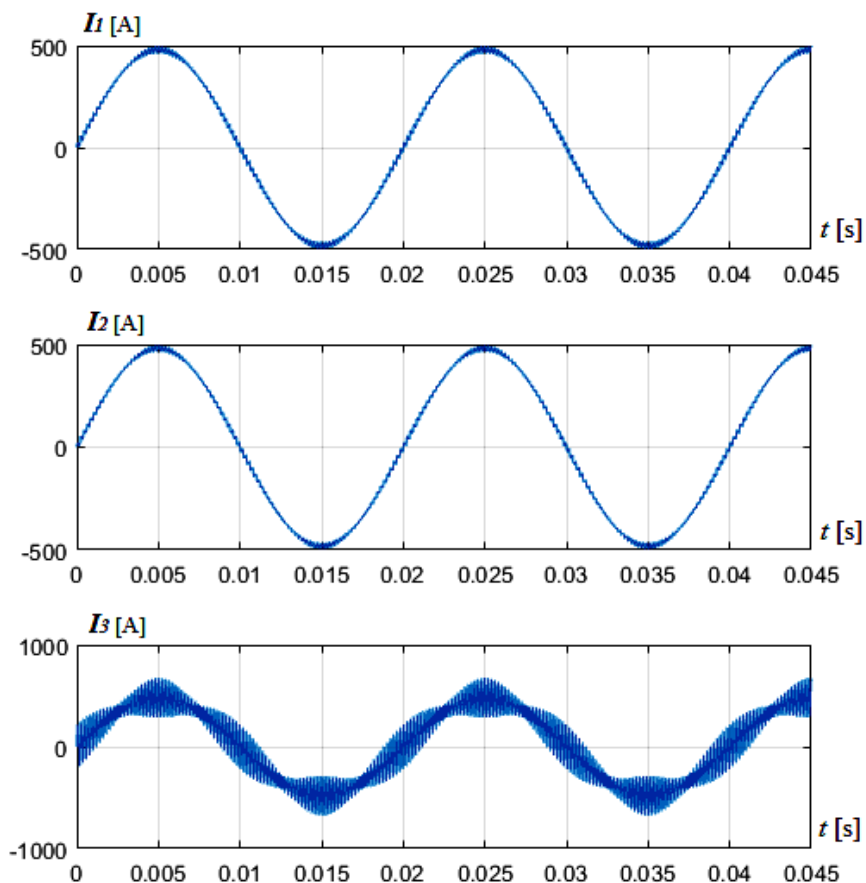
Figure 42 Secondary currents waveforms in case of co-phased carrier signals and $m_f = 99$

84
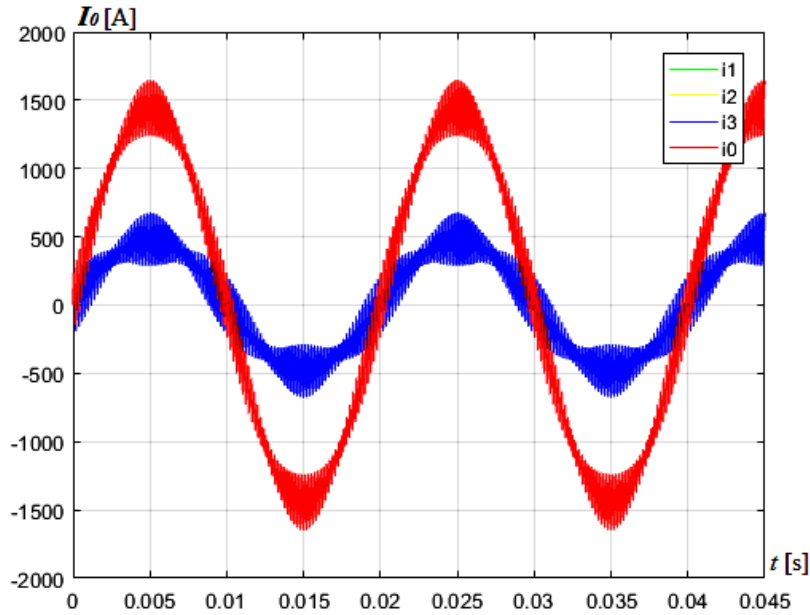
Figure 43 Primary and secondary currents waveforms in case of co-phased carrier signals and $m_f = 99$
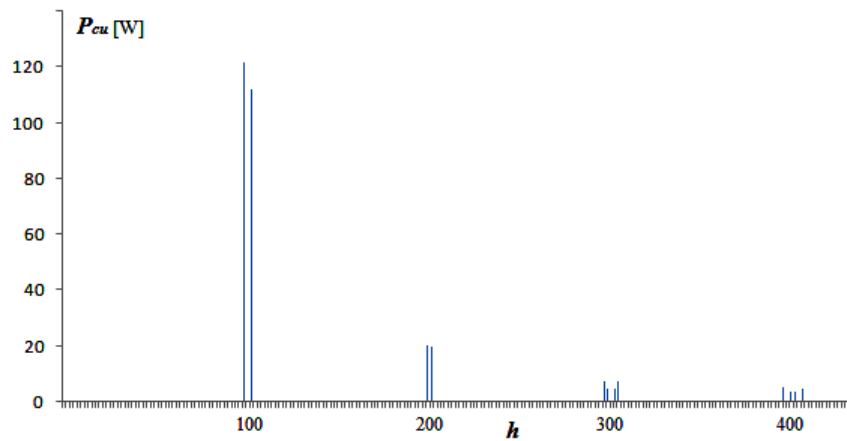
Figure 44 Total copper losses for high order harmonics ($h > 1$), co-phased carrier signals and $m_f = 99$

It can be noted that the current in the third low voltage winding has much higher total harmonic distortion than the other two secondary currents. This behaviour is not easy to be explained: since $\mathbf{R_S}$ and $\mathbf{L_S}$ matrices are full, each secondary current is influenced by the other two. The primary current has a significant distortion as well, which indicates that some measures have to be taken in order to reduce it, although it is already compliant with the standard IEC 1000-3-4 which limits the maximum THD to be 20%.

6.3 Case 2: $m_f = 99$, phase-shifted carrier signals

One of the possible alternatives is to shift the carrier signals as explained previously. In this case the results are summarized in Table 24 and the current waveforms are shown in Figure 45 and Figure 46 respectively. Total copper losses are given in Figure 47.

Table 24 Current fundamental and high order harmonics and copper losses in case of phase-shifted carrier signals and frequency ratio $m_f = 99$

Current	i_1	i_2	i_3	i_0'
$I_{fund,rms}$ [A]	481.12	481.12	481.12	1,443.36
$h = m_f - 2$ [%]	33.70	17.68	45.39	6.41
$h = m_f + 2$	32.37	16.99	43.59	6.16
$h = 2m_f - 1$	17.70	21.52	23.31	2.71
$h = 2m_f + 1$	17.52	21.31	23.07	2.69
THD_I [%]	57.89	53.56	77.83	10.54
$P_{Cu,tot}$ [kW]	16.57			
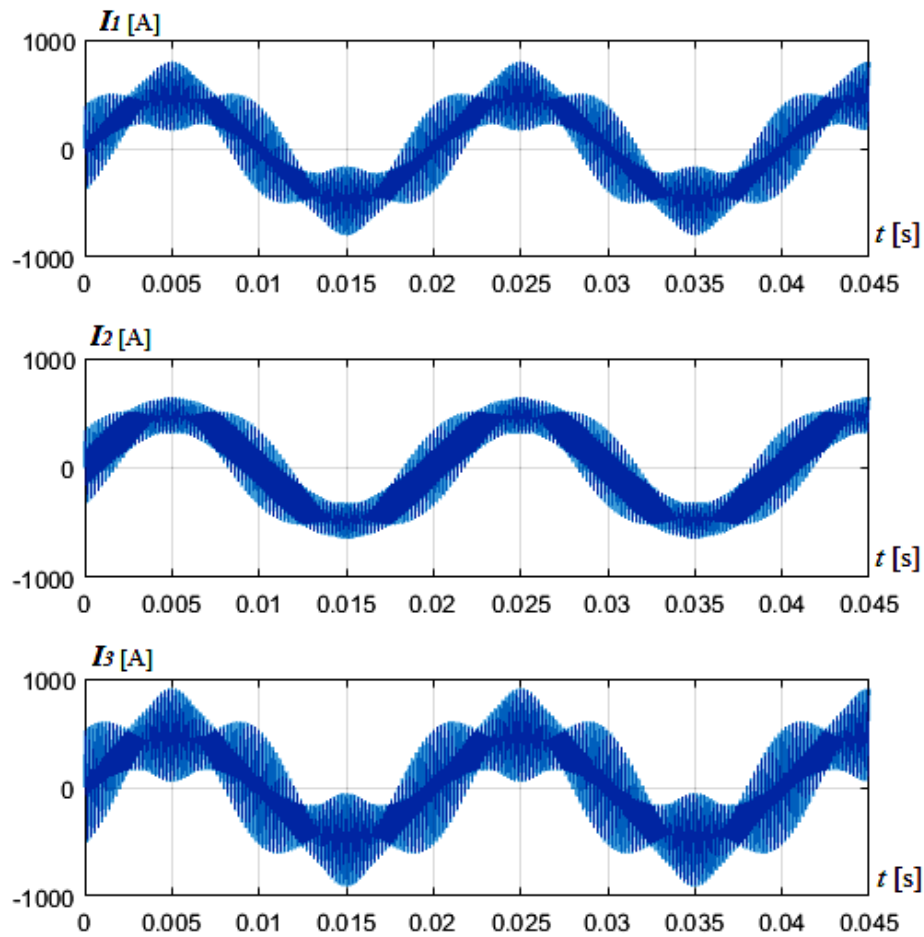
Figure 45 Secondary currents waveforms in case of phase-shifted carrier signals and $m_f = 99$
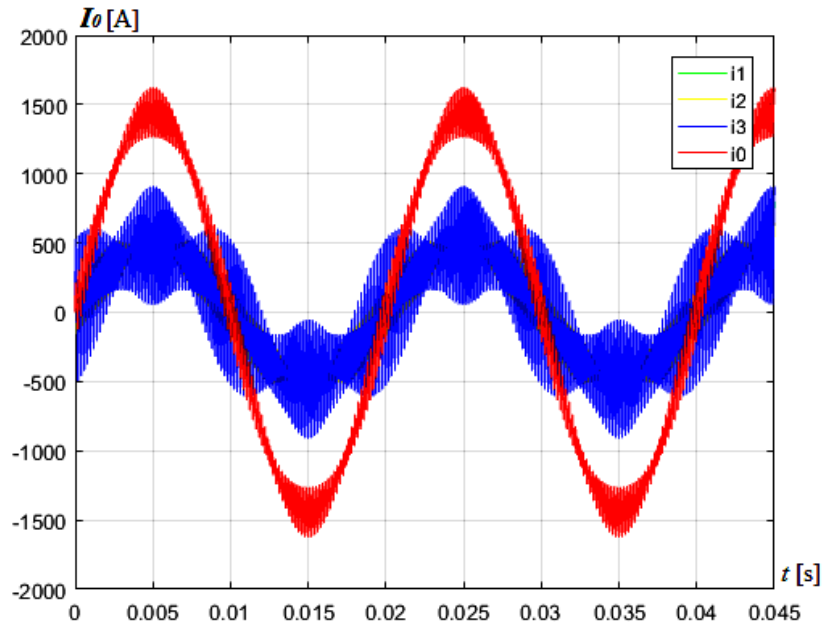
Figure 46 Primary and secondary currents waveforms in case of phase-shifted carrier signals and $m_f = 99$
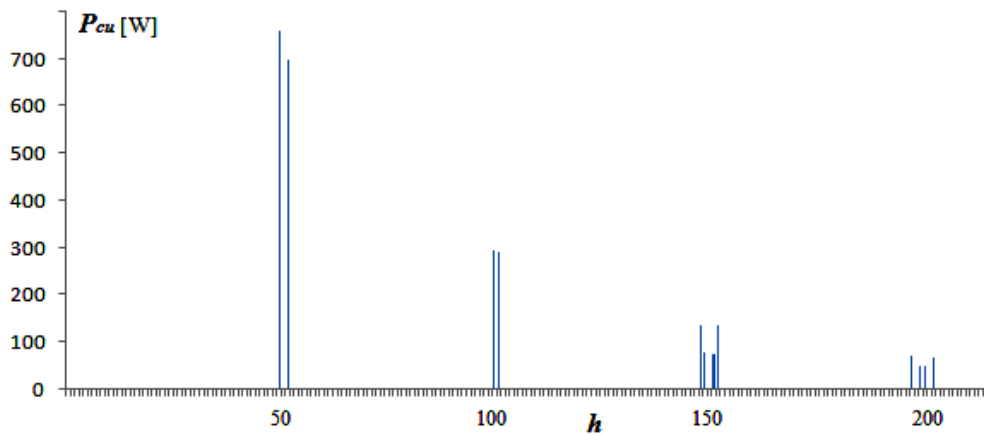
Figure 47 Total copper losses for high order harmonics ($h > 1$), phase-shifted carrier signals and $m_f = 99$

Several observations can be made when comparing the two cases of PWM control:

- Shifting the carrier signals leads to a decrease in the THD of the primary current drawn from the mains with respect to the case of in phase carrier signals;

- At the same time, shifting the carriers significantly increases the THD of all the secondary currents, which in turn increases the total copper losses in the transformer;

- Lower THD of the primary current i_0' is visible in the waveform at time instants close to the zero crossings, but the ripples at the current maximum and minimum seem to remain almost unchanged.

6.4 Case 3: $m_f = 33$, co-phased carrier signals

Power losses in the converters in both the previous cases will be high, due to the high switching frequency. Therefore, in the next analysis the switching frequency is lowered to 1.65 kHz. Current harmonic components' values are given in Table 25. The waveforms are shown in Figure 48 and Figure 49, and the copper losses at each harmonic frequency are presented in Figure 50.

Table 25 Current fundamental and high order harmonics and copper losses in case of co-phased carrier signals and frequency ratio $m_f = 33$

Current	i_1	i_2	i_3	$i_0{}'$
$I_{fund,rms}$ [A]	481.12	481.12	481.12	1,443.36
$h = m_f - 2$ [%]	6.35	5.83	64.48	22.59
$h = m_f + 2$	5.63	5.13	57.11	20.01
$h = 2m_f - 1$	2.64	2.49	25.43	8.77
$h = 2m_f + 1$	2.56	2.42	24.68	8.51
THD_I [%]	9.89	9.09	99.37	34.71
$P_{Cu,tot}$ [kW]	16.67			
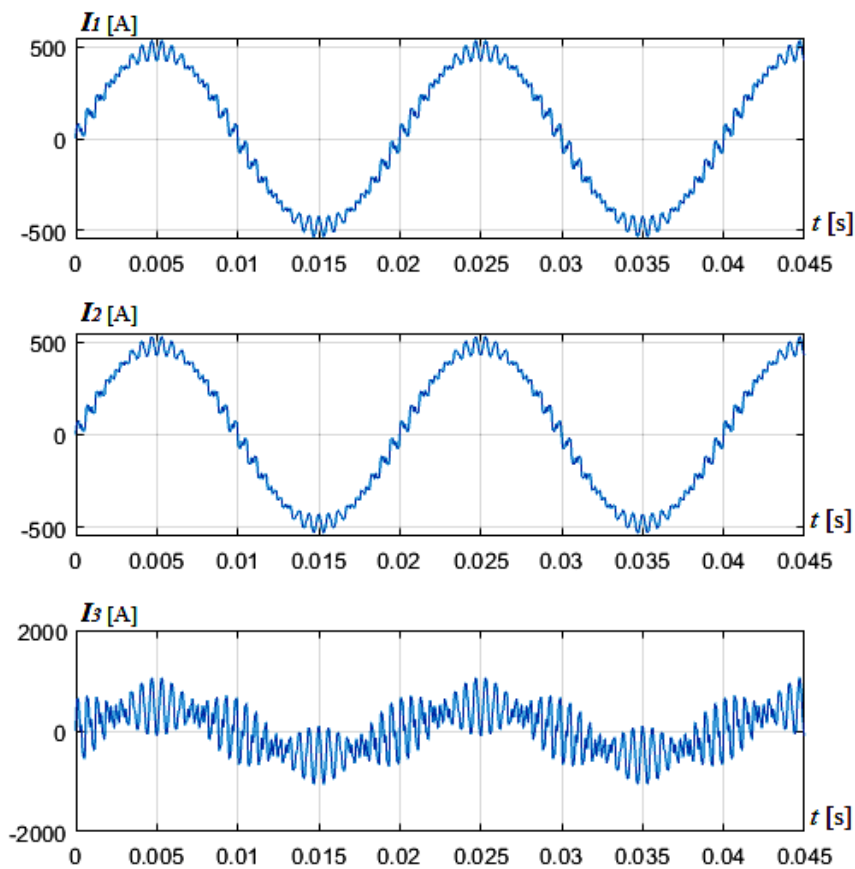
Figure 48 Secondary currents waveforms in case of co-phased carrier signals and $m_f = 33$
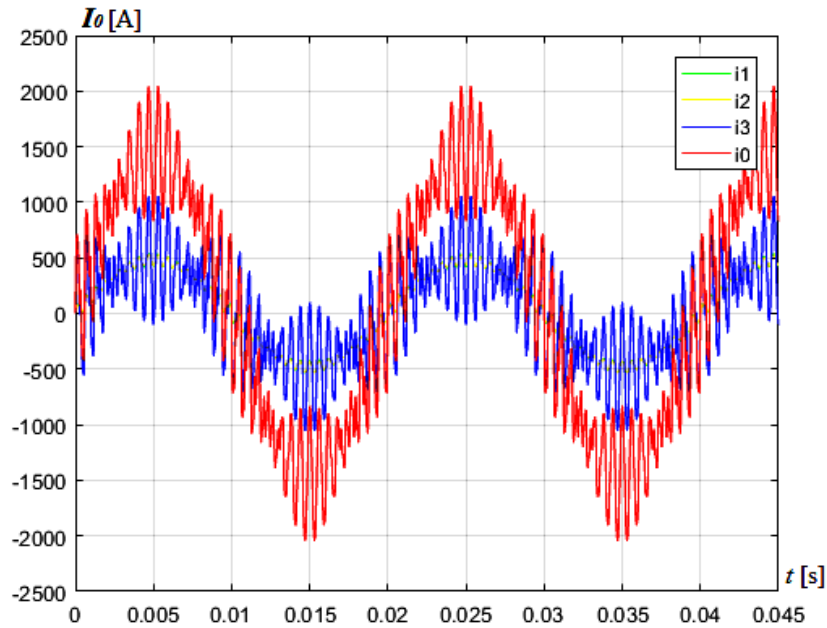
Figure 49 Primary and secondary currents waveforms in case of co-phased carrier signals and $m_f = 33$
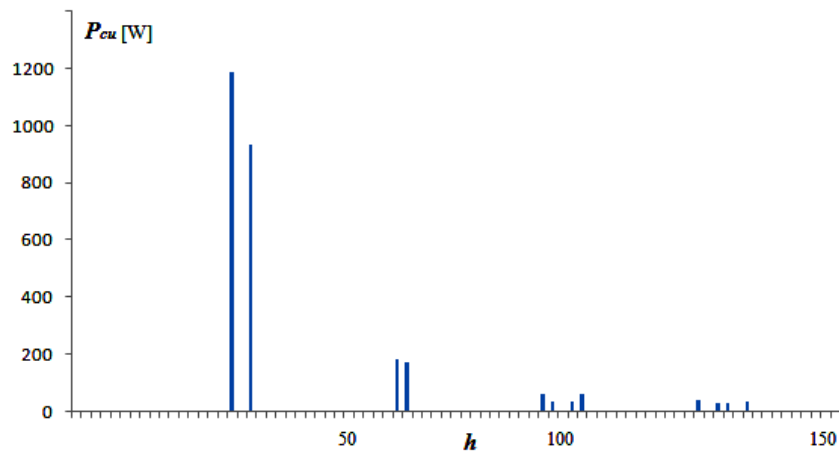
Figure 50 Total copper losses for high order harmonics ($h > 1$), co-phased carrier signals and $m_f = 33$

- Lowering the switching frequency results in higher THD of the secondary currents (comparing the cases 1 and 3 when carrier signals are in phase); however the THD of i_1 and i_2 is much lower than the case of phase-shifted carriers and higher frequency, which is not valid for i_3;

- Current i_3 shows a significant level of harmonic distortion;

- Total harmonic distortion of the primary current is the highest of all these cases, and has unacceptable value (34.71%);

- Considering the previous remarks, displacing the carrier signals will result in slightly smaller primary current ripples (THD$_{i0}$=31.81%); however its value is still too high;

89

- Total core losses are the highest as well, due to the very large harmonic components of the secondary current in the third winding;

- Lowering the switching frequency is not advantageous from the mains point of view, because the THD of the currents, especially of the one drawn from the gird is particularly high and will create voltage problems as well. On the other hand, high switching frequency generates high switching losses in the converters and may imply head dissipation problems.

6.5 Case 4: $m_f = 99$, non-balanced load, phase-shifted carrier signals

From the previous analysis it becomes evident that high switching frequency results in low copper losses and low primary current total harmonic distortion. Assuming rated currents in all the secondary coils was taken as a reference case in the previous analyses; however it is not expected to occur often in practice. It is reasonable to expect imbalance in the secondary currents, which depends on the battery characteristics and their *SOC*. An example of this type is presented here: rated currents are assumed in two of the secondary coils, while $0.75 \cdot I_{sec,n}$ in the third one. All the secondary currents are in phase, as well as in phase with the supply voltage, so that a unity power factor is ensured. The switching frequency is 4.95 kHz and carrier signals are phase-shifted by $T_{sw}/3$. The fundamental and main harmonic values are given in Table 26, current waveforms are shown in Figure 51 and Figure 52 and total copper losses are presented in Figure 53.

Table 26 Current fundamental and high order harmonics and copper losses in case of phase-shifted carrier signals, imbalanced load and frequency ratio $m_f = 99$

Current	i_1	i_2	i_3	$i_0{}'$
$I_{fund,rms}$ [A]	481.12	481.12	360.84	1,323.08
$h = m_f - 2$ [%]	33.63	17.57	60.68	7.02
$h = m_f + 2$	32.30	16.88	58.27	6.74
$h = 2m_f - 1$	17.66	21.49	31.00	2.95
$h = 2m_f + 1$	17.49	21.28	30.69	2.92
THD$_I$ [%]	57.80	53.47	103.89	11.52
$P_{Cu,tot}$ [kW]	14.43			

A comparison between case 2 when all the secondary currents equal their rated values and this case of load unbalance can be made. The carrier signals are always phase-shifted.

- THD of the currents i_1 and i_2, whose fundamental values equal the rated currents are almost the same as in the case 2 (balanced load);

- THD of the current i_3 is much higher than in the case of balanced load (103.89% and 77.83% respectively). This is due to the fact that the fundamental component has lower value than the rated;

- THD of the primary current is higher than case 2, due to the higher distortion of the secondary currents;

- Total copper losses are lower due to the fact that the load of one secondary winding is lower than its rated value.
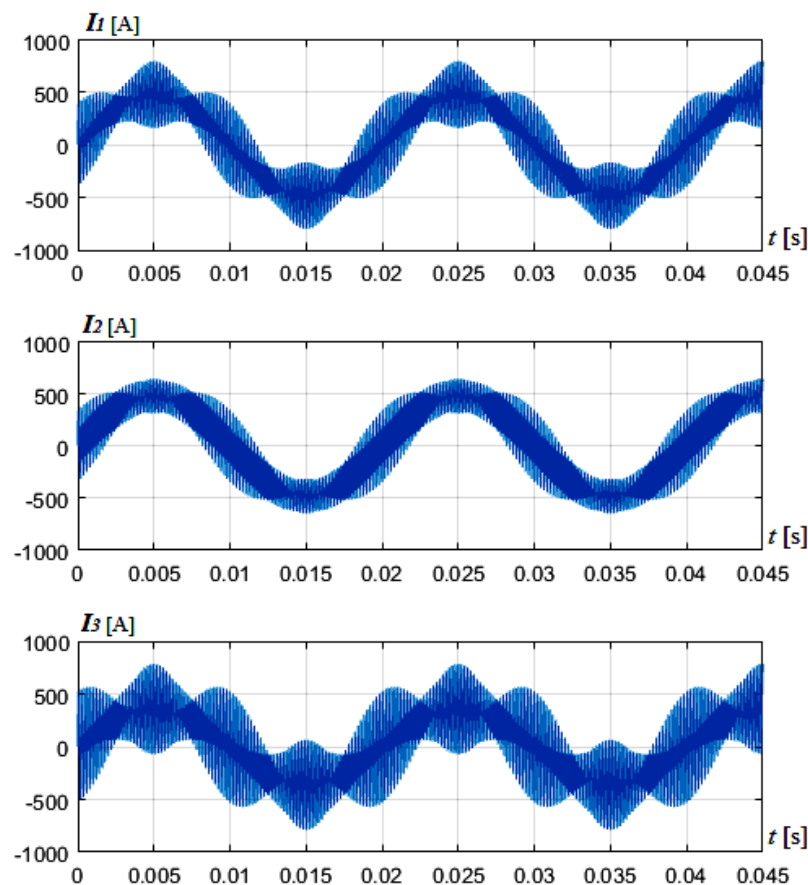
Figure 51 Secondary currents waveforms in case of phase-shifted carrier signals, unbalanced load and
$m_f = 99$
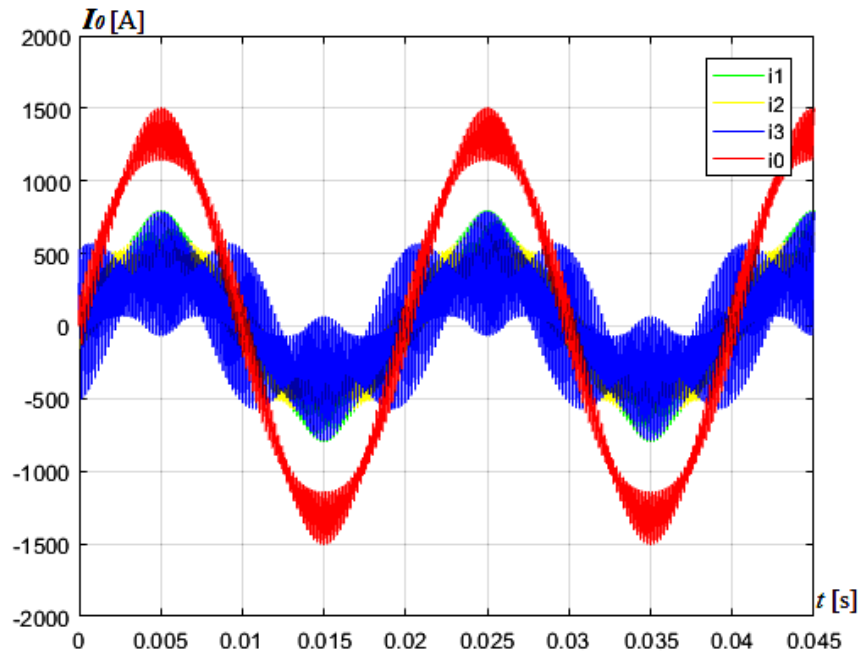
Figure 52 Primary and secondary currents waveforms in case of phase-shifted carrier signals, unbalanced load and $m_f = 99$
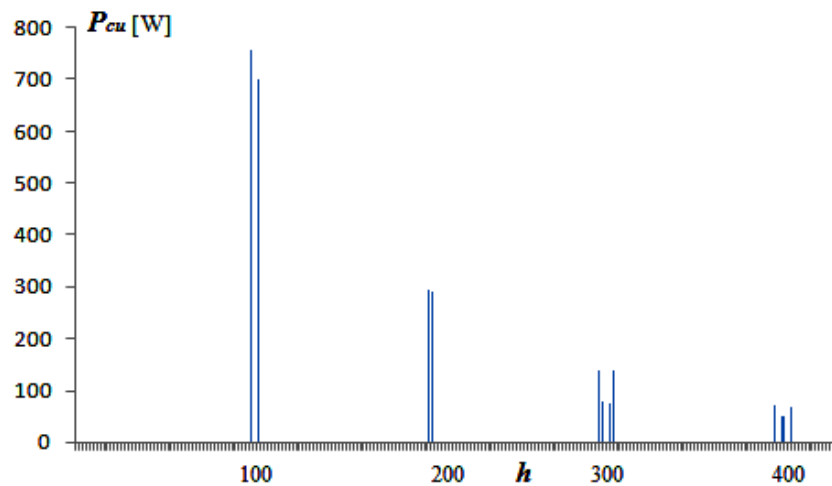
Figure 53 Total copper losses for high order harmonics ($h > 1$), phase-shifted carrier signals, imbalanced load and $m_f = 99$

6.6 Core losses in distorted operating conditions

In non-sinusoidal operating conditions the core losses are expected to be higher than the reference sinusoidal case. In principle it is possible to calculate eddy current losses for each harmonic by Eq. (145) and sum them up. However, high order harmonics modify the flux density distribution, causing it to be non-uniform in the lamination width any longer. This effect can be accounted for by classical reduction factor k_{Fe} [69]:

$$k_{Fe}(hf_1) = \frac{3}{\xi_{Fe}(hf_1)} \cdot \frac{\sinh\left(\xi_{Fe}(hf_1)\right) - \sin\left(\xi_{Fe}(hf_1)\right)}{\cosh\left(\xi_{Fe}(hf_1)\right) - \cos\left(\xi_{Fe}(hf_1)\right)}, \tag{157}$$

where the auxiliary variable ξ_{Fe} and the penetration depth p_d are calculated as:

$$\xi_{Fe}(hf_1) = \frac{d_{lam}}{p_d(hf_1)}, \quad p_d(hf_1) = \sqrt{\frac{\rho_{Fe}}{\pi \cdot \mu_{Fe} \cdot h \cdot f_1}}, \tag{158}$$

where d_{lam} is the lamination width and ρ_{Fe} is the iron specific resistance. The coefficient k_{Fe} equals 1 at the mains frequency and tends to zero as the harmonic order increases.

Specific eddy current losses in distorted conditions can be estimated by multiplying the specific losses at fundamental frequency (Eq. (145)) by the additional loss coefficient $k_{a,ec}$:

$$p_{Fe,ec,dist} = k_{a,ec} \cdot p_{Fe,ec}(B_1, f_1). \tag{159}$$

$$k_{a,ec} = 1 + \sum_{h=2}^{\infty} h^2 \cdot \left(\frac{B_h}{B_1}\right)^2 \cdot k_{Fe}(h \cdot f_1), \tag{160}$$

where B_h is the peak value of the flux density for harmonic h, calculated for a general $b(t)$ waveform by Fourier transform. It can be calculated by using the converter input root-mean square voltage value as:

$$B_h = \frac{\sqrt{2}}{\omega_{1c} N_2 S_{Fe,net}} \cdot \frac{V_{i,h,rms}}{h}, \tag{161}$$

where $S_{Fe,net}$ is the core net cross section area and N_2 is the number of turns of the low voltage winding. It should be noted that core losses are evaluated at no load conditions; therefore it is enough to take into account only one VSI boost rectifier.

On the other hand, the specific hysteresis losses depend on the instantaneous peak value B only, regardless of the $b(t)$ waveform, when the minor loops are neglected. Considering that B should be almost equal to the fundamental peak value B_1, it can be concluded that hysteresis losses in distorted conditions are the same as in sinusoidal operation.

Regarding the different switching frequencies discussed previously, the reduction coefficient for core losses can be calculated by using Eq. (157). As shown in Figure 54, its value is equal to 1 at industrial frequency and tends to zero as the harmonic order increases.
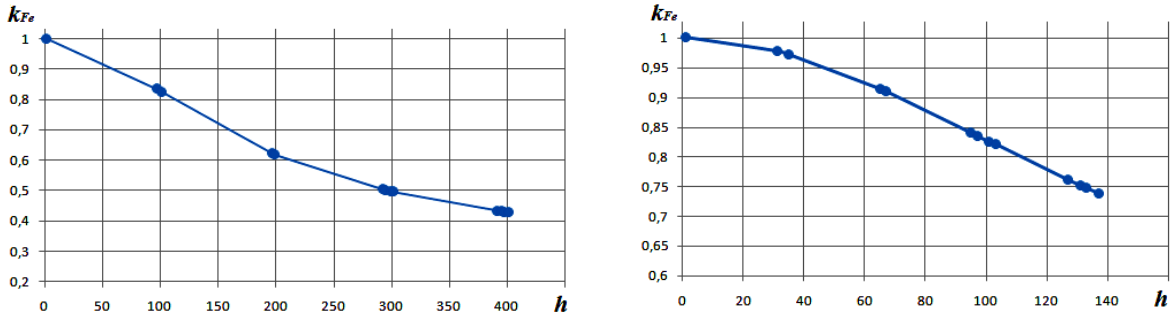
Figure 54 Corrective coefficient for core losses at high frequencies : $m_f = 99$ **(left) and** $m_f = 33$ **(right)**

Based on the peak flux density and the corrective coefficient calculated at each harmonic frequency, the core additional eddy current loss coefficient $k_{a,ec}$ and total core losses can be estimated. From the results summarized in Table 27, it can be noticed that due to the additional eddy currents in the core its losses increase for 22.18% and 32.18% respectively, depending on the switching frequency.

Combining the results for the estimated copper and core losses in distorted conditions, transformer efficiency can be found. As shown in Table 28, when the rated currents flow through the secondary windings, the most efficient operating condition would be achieved when the carrier signals are co-phased and the switching frequency is 4.95 kHz. However, the values in all the cases considered are generally very close to each other.

Table 27 Core losses estimation at harmonic conditions

$k_{a,ec(mf=99)}$	$k_{a,ec(mf=33)}$
2.1092	2.6091
$P_{Fe(mf=99)}$ [W]	$P_{Fe(mf=33)}$ [W]
1,097.5	1,187.3
ΔP_{Fe} [%]	ΔP_{Fe} [%]
22.18	32.18

Table 28 Transformer efficiency estimation

Case #	Description	Efficiency [%]
0	Sinusoidal ideal conditions	98.53
1	$m_f = 99$, co-phased	98.47
2	$m_f = 99$, phase-shifted	98.23
3	$m_f = 33$, co-phased	98.21
4	$m_f = 99$, phase-shifted, unbalanced	98.31

7 Transformer design temperature validation

7.1 Basic transformer temperature calculations

During normal transformer operation, heat is generated inside its components due to the total power losses, leading to a temperature increase above the ambient temperature. In order to ensure reliable operation of the transformer, temperature rise of any part at rated load should not be higher than the limiting value. Since different materials are used in transformer construction (copper, iron, insulating materials, etc.), it is essential to perform temperature analysis in advance and make design corrections if necessary. All the expressions for the temperature rise can be derived approximately on the basis of the theory of heating an ideal solid body [57].

Although obtaining accurate values is a difficult task, in this chapter a brief temperature calculation is presented in order to validate the designs proposed previously. The procedure followed to determine temperature rise is explained in details in Appendix 5, based on [56]. General temperature distribution profile is shown in Figure 55. Assuming rated load conditions on all the secondary windings, the results obtained are summarized in Table 29.
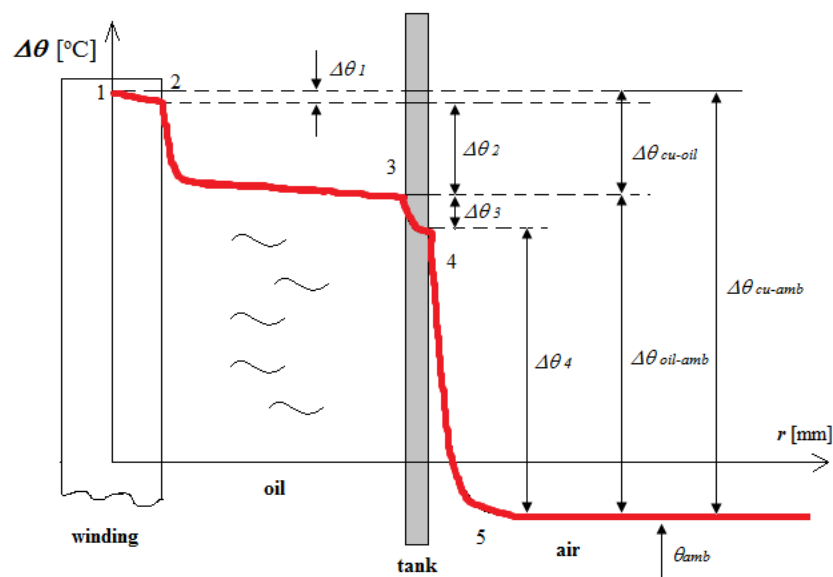
Figure 55 Temperature distribution profile in a transformer [56]

It can be noted that temperature rise of the winding over oil temperature could be a possible problem in both designs proposed. However, the reference value is recommended in transformer design literature, not imposed by standards. This possible threat point can be overcome by increasing the number or the width of axial ducts, especially in the low voltage

coils (as it was done here in the case of six winding transformer: two axial ducts were designated between conductor layers). Another possible improvement could be increasing the number or the dimensions of transformer ribs. The final design is approved as long as the maximum oil temperature rise over the ambient and copper total temperature rise over the ambient temperature are below the standardized limits.

Table 29 Estimation of transformer temperature rise in rated conditions

Temperature rise	Symbol	4 windings design	6 windings design	Max. allowed value [70]
Winding total temperature rise over oil temperature	$\Delta\theta_{Cu\text{-}oil}$	24	29	≈ 20
Transformer tank temperature rise over the ambient temperature	$\Delta\theta_4$	37	30	≈ 40
Transformer oil maximum temperature rise over the ambient temperature	$\Delta\theta_{oil\text{-}amb}$	48	39	60
Copper total temperature rise over the ambient temperature	$\Delta\theta_{Cu\text{-}amb}$	62	62	65

7.2 Transformer thermal validation in sinusoidal balanced conditions

One of the most important parameters in determining the transformer loading capability is the winding hot spot temperature, which is located at the radial centre on the top of the windings on the insulation internal side. Transformer temperature model is based on the fact that increase in the load current causes increase in the power losses and in the temperatures of the top oil and of the windings [71].

In order to determine the hot spot temperature more precisely, it is recommended to use so called dynamic rating. It is defined as the maximum loading that the transformer can acceptably sustain under time-varying load and / or environmental conditions [72]. Top oil temperature rise over ambient temperature ($\Delta\theta_{TO}$) and hot spot temperature rise over top oil temperature ($\Delta\theta_{HK}$) in the transient interval when the load changes from one steady state to another are described by exponential functions analogous to a charging and discharging RC circuit. These functions are obtained as solutions to the differential equations describing the equivalent thermal model of the transformer [70]:

$$T_{TO}\frac{d(\Delta\theta_{TO})}{dt} = -\Delta\theta_{TO} + \Delta\theta_{TO}(u) .$$

(162)

$$T_{HS} \frac{d(\Delta\theta_{HK})}{dt} = -\Delta\theta_{HK} + \Delta\theta_{HS}(u) \, , \tag{163}$$

where $\Delta\theta_{TO}(u)$ is steady-state (ultimate) top oil temperature rise over the ambient in case of load K, $\Delta\theta_{HS}(u)$ is the steady-state (ultimate) hot spot temperature rise over the top oil temperature in case of load K, T_{TO} and T_{HS} are oil and hot spot time constants respectively.

According to the IEC 60076-7 Standard, for distribution transformers with ONAN type of cooling, the hot spot temperature at any load K is the sum of the ambient temperature, top oil temperature rise over the ambient and the winding temperature rise over top oil [70]:

$$\theta_{HS} = \theta_a + \Delta\theta_{TO}(t) + \Delta\theta_{HK}(t) \, . \tag{164}$$

At any load condition K, the top oil temperature rise is an exponential function of time:

$$\Delta\theta_{TO}(t) = \left[\Delta\theta_{TO}(u) - \Delta\theta_{TO}(i)\right] \cdot \left[1 - e^{-t/T_{TO}}\right] + \Delta\theta_{TO}(i) \, , \tag{165}$$

where $\Delta\theta_{TO}(i)$ is the initial top oil temperature rise. The steady-state temperature rise of the top oil for any load K is given by:

$$\Delta\theta_{TO}(u) = \Delta\theta_{TOR} \cdot \left(\frac{1 + R \cdot K^2}{1 + R}\right)^x \, , \tag{166}$$

where R is ratio between power losses in rated conditions and no-load in p.u., x is exponent for calculating the top oil temperature rise over the ambient temperature in load conditions different than the rated ones and $\Delta\theta_{TOR}$ is top oil temperature rise over the ambient temperature in case of rated load.

The difference between the hot spot temperature and the top oil temperature, $\Delta\theta_{HK}(t)$, is calculated as:

$$\Delta\theta_{HK}(t) = \left[\Delta\theta_{HK}(u) - \Delta\theta_{HK}(i)\right] \cdot \left[1 - e^{-t/T_{HS}}\right] + \Delta\theta_{HK}(i) \, , \tag{167}$$

where $\Delta\theta_{HK}(i)$ is the initial hot spot temperature rise over the top oil temperature. In the same manner, the final hot spot temperature rise is determined by:

$$\Delta\theta_{HK}(u) = \Delta\theta_{HKR} \cdot [K]^y \, , \tag{168}$$

where y is coefficient for calculating the hot spot temperature rise over the top oil temperature in load conditions different than the rated ones and $\Delta\theta_{HKR}$ is hot spot temperature rise over the top oil temperature in case of rated conditions.

Time constants of the transformer oil and the hot spot can be calculated as:

$$T_{TO} = 60 \cdot \frac{C_{th,oil} \cdot \Delta\theta_{TOR}}{q_{total}} \quad . \tag{169}$$

$$T_{HS} = 2{,}75 \cdot \frac{\Delta\theta_{HSR}}{(1 + P_{EC}) \cdot g^2} \quad , \tag{170}$$

where q_{total} are total power losses in the transformer, g is the average current density considering rated conditions, P_{EC} are eddy current losses in p.u.. Oil thermal coefficient is determined by using the total oil mass M_o [kg]:

$$C_{th,oil} = 0{,}48 \cdot M_o \quad . \tag{171}$$

According to the IEEE Std. C57.110-1998, power losses in the windings due to eddy currents in oil-immersed distribution transformers are 33% of the total stray losses (P_{TSL}) and are calculated as [73]:

$$P_{EC} = 0{,}33 \cdot P_{TSL} = 0{,}33 \cdot \left(P_{LL} - P_{DC} \right) = 0{,}33 \cdot \left[P_{LL} - 1{,}5 \cdot \left(I_{1R}^2 \cdot R_1 + I_{2R}^2 \cdot R_2 \right) \right] , \tag{172}$$

where P_{LL} are measured power losses in short-circuit conditions, P_{DC} are Ohmic power losses in the windings, I_{1R} and I_{2R} are primary and secondary rated current respectively, R_1 and R_2 are dc resistances of the primary and secondary winding respectively. The same expression can be modified for multi-winding transformer taking into account the Ohmic resistances of each secondary winding and always referring the currents and the resistances to one side:

$$P_{EC} = 0{,}33 \cdot P_{TSL} = 0{,}33 \cdot \left\{ P_{LL} - 1{,}5 \cdot \left[I_{1R}^2 \cdot R_{HV1} + I_{2R}^2 \cdot \left(R_{LV1} + R_{LV2} + R_{LV3} \right) \right] \right\} . \tag{173}$$

7.3 Transformer thermal validation in case of nonsinusoidal nonlinear load

The existing loading guides for oil-immersed transformers are based on the conservative assumptions for constant daily load and average daily or monthly ambient temperatures. In order to determine the transformer temperature profile more accurately, it is necessary to take into account the variation of the load and ambient temperature in short time intervals. In case of multi-winding transformer, it is even more precise to consider each coil separately, because the loads of the secondary windings may not be balanced and therefore it will cause different temperature rise. However, in determining the top oil temperature it is recommended to use the equivalent load, since it takes into account the imbalance introduced by each winding.

As explained previously, employing any kind of rectifier on the secondary transformer side will cause distortion of the secondary currents, which are in turn reflected in the primary current waveforms. In case of well known harmonic spectrum of each secondary current, it

can be assumed that the same spectrum is valid for the entire daily load cycle. Taking into account these secondary current harmonics, an equivalent load for each winding can be calculated.

As input data to the algorithm for calculating hot spot temperature, apart from the transformer nameplate data and some of the constructional data (summarized in Table 30), the following information are also needed:

- K_{LV1}, K_{LV2}, K_{LV3} – daily load currents cycles [p.u.] for each secondary coil (Figure 56)
- θ_a – daily ambient temperature in [°C] (Figure 57)
- $I_{h,LV1}$, $I_{h,LV2}$, $I_{h,LV3}$ – current harmonic components of each secondary coil [p.u.]. (Figure 58)
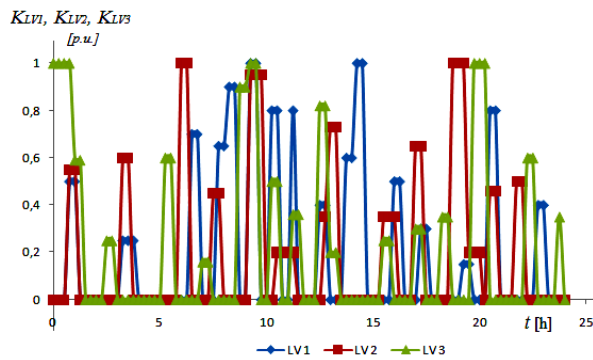
Figure 56 Daily load cycles for three secondary windings
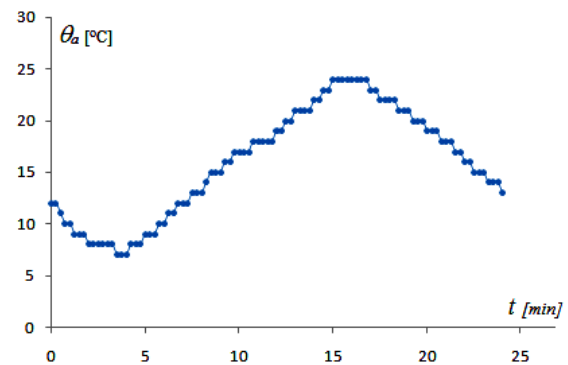
Figure 57 Daily ambient temperature
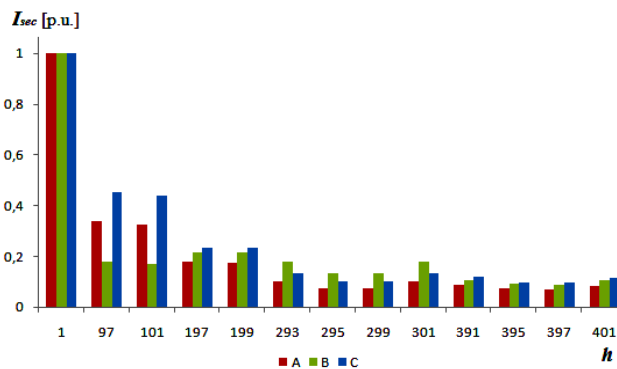
Figure 58 Secondary currents harmonic spectrum for m_f = 99 and phase-shifted carrier signals

It should be noted that daily load cycles exhibit step changes and discontinuities which will decrease remaining useful life of the transformer. In different surveys peak load has been found to occur at certain hours: 11am, 12am, 22pm and 23pm. The daily cycle repeats each seven days (considering peoples' needs and habits during work-days and weekends). An increase in the load is expected in summer and winter with respect to spring and autumn [74], [75].

Table 30 Nameplate and constructional data of the four coil multi-winding transformer

Rated apparent power	S_{1n} = 1000	S_{2n} = 333.33	kVA
Rated line currents	I_{1n} = 28.87	I_{2n} = 481.12	A
Ohmic resistances of the windings	R_{HV1} = 1.1521	R_{LV1} = 1.9175 R_{LV1} = 2.2676 R_{LV1} = 2.6176	mΩ
Total oil mass	M_o = 480		kg
Calculated losses at no-load and at short-circuit	P_{NL} = 898	P_{LL}=13,850	W
Current density in the secondary winding	g_2 = 3.28		A/mm^2
Eddy current and other stray losses	P_{EC} = 2,900	P_{OSL} = 5,887	W
Oil and winding exponent	x = 0.8	y = 1.6	/
Oil and winding time constant	T_{TO} = 83.77	T_{HS} = 16.48	min

The procedure for calculating hot spot temperature at each time interval (assuming that it is constant during this time interval), considering the daily load diagram consists of the following steps (adapted from [76] - [78]):

- The influence of each current harmonic component, from h=0 to h=h_{max}, on the load of the coil itself is taken into account by the harmonic load coefficient:

$$K_{h,LV1} = \frac{I_{h,LV1}}{I_{2n}} K_{LV1}; \; K_{h,LV2} = \frac{I_{h,LV2}}{I_{2n}} K_{LV2}; \; K_{h,LV3} = \frac{I_{h,LV3}}{I_{2n}} K_{LV3} \; . \tag{174}$$

- Coil equivalent load coefficient of each secondary winding, considering all the harmonics, is calculated as shown in Eq. (175) for each of the secondary coils:

$$K_{LV1,eq}^2 = \frac{\sum_{h=1}^{h\max} K_{h,LV1}^2 + P_{EC} \cdot \sum_{h=1}^{h\max} K_{h,LV1}^2 \cdot h^2}{1 + P_{EC}} \; . \tag{175}$$

- Ultimate hot spot temperature rise over the ambient temperature for the time interval considered, for each secondary coil is calculated by modifying Eq. (168) as:

$$\Delta\theta_{HS,LV1}(u) = \Delta\theta_{HSR} \cdot \left[K_{LV1,eq}^2\right]^{y/2} \; . \tag{176}$$

- Actual hot spot temperature rise over the ambient which is reached at the end of the time interval considered for each coil is calculated by the modified Eq. (167):

$$\Delta\theta_{HS,LV1}(t) = \left[\Delta\theta_{HS,LV1}(u) - \Delta\theta_{HS,LV1}(i)\right] \cdot \left[1 - e^{-t/T_{HS}}\right] + \Delta\theta_{HS,LV1}(t - \Delta t) \; . \tag{177}$$

- Now the effects of all the secondary loads with respect to the harmonic order are calculated (for h=0 to h=h_{max}):

$$K_{h,eq} = \sqrt{\frac{1}{3}\left(K_{h,LV1}^2 + K_{h,LV3}^2 + K_{h,LV3}^2\right)} \quad . \tag{178}$$

- Due to the presence of nonlinear and imbalanced load, the component in Eq. (166) which contains the load coefficient K is replaced with the expression on the right side of Eq. (179):

$$\left[\frac{1 + R \cdot K^2}{1 + R}\right] = \frac{P_{NL} + \left(P_{DC}\sum_{h=1}^{h\,max}K_{h,eq}^2 + P_{EC}\sum_{h=1}^{h\,max}K_{h,eq}^2 h^2 + P_{OSL}\sum_{h=1}^{h\,max}K_{h,eq}^2 h^{0,8}\right)}{P_{NL} + P_{LL}} = K_{TOT} \tag{179}$$

where P_{NL} are the no-load power losses and P_{OSL} are other stray losses in constructional components different from windings, which can be determined as [73]:

$$P_{DC} = 1,5 \cdot \left[I_{1R}^2 \cdot R_{HV1} + I_{2R}^2 \cdot \left(R_{LV1} + R_{LV2} + R_{LV3}\right)\right] \quad . \tag{180}$$

$$P_{OSL} = P_{TSL} - P_{EC} = P_{LL} - P_{DC} \quad . \tag{181}$$

- Final top oil temperature rise over the ambient temperature at the time interval considered is:

$$\Delta\theta_{TO}(u) = \Delta\theta_{TOR} \cdot K_{TOT}^x \tag{182}$$

- Now the actual top oil temperature rise can be calculated by using Eq. (165).
- Hot spot temperature for each secondary coil is calculated by Eq. (164):

$$\theta_{HS,LV1} = \theta_a + \Delta\theta_{TO}(t) + \Delta\theta_{HS,LV1}(t) \quad . \tag{183}$$

- Finally, the average hot spot temperature at the time interval considered is:

$$\theta_{HS,av} = \frac{1}{3}\left(\theta_{HS,LV1} + \theta_{HS,LV2} + \theta_{HS,LV3}\right) \quad . \tag{184}$$

Winding time constant can be neglected because its value is very low and it has a very limited influence on the hot spot temperature. Initial top oil temperature rise is $\Delta\theta_{TO}(i)=12\ ^{\circ}$C and initial hot spot temperature rise is $\Delta\theta_{HS}(i)=0\ ^{\circ}$C. Recommended and maximum allowed values for the relevant temperatures are given in Table 31. The results obtained following the procedure as explained are shown in Figure 59 and Figure 60. It can be seen that both top oil temperature rise and hot spot temperature are within the standard limits during the entire daily load cycle. Although the assumed daily load is only hypothetical, this analysis can still be considered as a confirmation of the transformer design form temperature point of view.

Table 31 Reference (R) and maximum allowable (MA) temperatures according to IEC Standards [70]

	Reference values		IEC [^{o}C]
R	Ambient temperature	θ_a	20
MA	Top oil temperature rise over ambient temperature	$\Delta\theta_{TOR}$	55
MA	Hot spot temperature rise over top oil temperature	$\Delta\theta_{HKR}$	23
MA	Hot spot temperature rise over ambient temperature	$\Delta\theta_{HSR}$	78
MA	Hot spot temperature	θ_{HS}	98
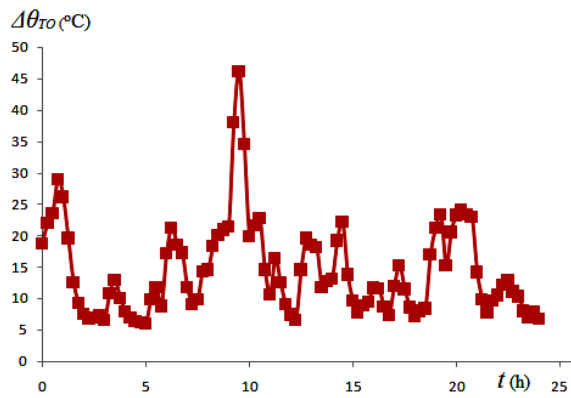
Figure 59 Daily top oil temperature rise over ambient temperature
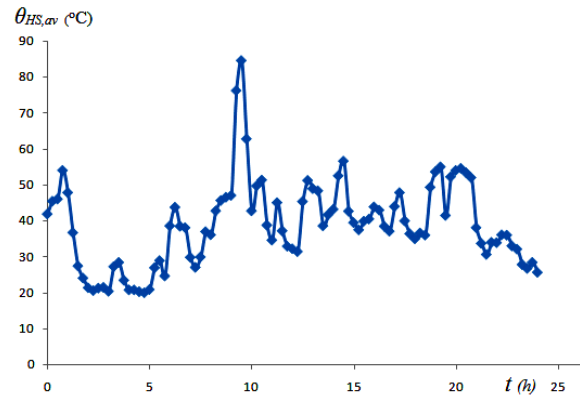
Figure 60 Daily hot spot temperature

Conclusions and future work

In this master thesis a multi-winding transformer for dc electric vehicles charging station was discussed. After reviewing briefly the basic principles of two-winding transformer operation, a multi-winding transformer was described in terms of advantages and disadvantages and application areas. As a study case was chosen a dc fast electric vehicle charging station and various charging levels, battery types and charging techniques were described. In order to supply a dc current form the transformer output terminal to the vehicle's battery, a power converter system is necessary. Two power rectifying topologies were presented: one involving a three-phase diode bridge and step-up/down converter, while the other one consisting of voltage source inverter boost-rectifier. Both configurations were compared in terms of components choice, control techniques and current harmonic content. Since the single-stage VSI-boost rectifier topology was found to be superior due to the absence of low-order harmonics in the transformer output currents, close to unity power factor and higher reliability, it was considered latter in details.

Based on the European patent for multi-winding transformer EV charging station and the Japanese protocol CHAdeMO which deals with fast dc charging, transformer basic requirements were identified and sizing criteria were established. By following a simple design procedure, two different coil dispositions were proposed: four and six coil transformers, having concentric and stacked coils respectively. The former one has three concentric secondary windings, each supplying a separate outlet and one winding connected to the mains. The latter one consists of axially placed three pairs of low and high voltage coils, where all the primary coils are connected in parallel to the mains. Both designs were compared with respect to the amount of material (steel and copper) needed, which is an indication of the production costs, and the four coil transformer was obviously superior.

For each transformer an equivalent network was obtained analytically, by using their constructional parameters. In the case of four coil transformer so called Starr network was identified, which is well-known in the literature, while in the case of six coil design a mesh network was obtained through a slightly more complicated mathematical procedure. In both cases the equivalent network was used to estimate the copper losses in the transformers, as well as the core losses. Considering that the four coil design showed better performances in ideal rated sinusoidal conditions, it was further analyzed in distorted operation.

Accounting for the effects of multiple secondary coils, each supplying a different EV, transformer performances were estimated in non-sinusoidal conditions. A few various PWM control strategies for the VSI boost rectifiers were analyzed: operation at different switching frequencies (4.95 kHz and 1.65 kHz), carrier signals imposed to be in phase and phase-shifted by $T_{sw}/3$ and lastly, a case when the load is unbalanced was discussed. For each case current waveforms were obtained by synthesizing Fourier series sinusoidal components. Some of the main findings are:

- Displacing the carrier signals for each VSI for $T_{sw}/3$ increases the THD of all the secondary currents, while at the same time reduces the THD of the primary current drawn from the mains;

- Copper losses are lower when the carrier signals are co-phased and therefore the transformer efficiency is the highest;

- Core losses decrease with increasing the switching frequency, but at the same time converter losses will increase;

- Unbalanced load on the secondary windings will cause increase in the THD, both in the primary and the secondary currents;

- Increasing the distances between the transformer windings will increase the self- and mutual inductances, therefore the current harmonic content will be lower. However, the winding resistances will increase as well, which leads to higher copper losses;

- There has to be a trade-off between the transformer performances (in the sense of losses and efficiency) and the converter performances (in terms of losses and waveforms quality).

Finally, a brief temperature analysis was conducted in order to verify that the proposed transformer design will satisfy the standard temperature requirements, even in the case of load unbalance.

The main contributions in this work are:

- The application of multi-winding transformer in EV dc charging stations is a recently proposed innovation, and therefore the existing literature is quite scarce. The researchers mainly deal with the power conversion system, not with the transformer itself, although its performances depend on the conversion system components and control technique choice;

- Different transformer designs were compared in terms of materials cost and performances estimation, which is useful in making a final decision of which type to be employed;

- Estimating the copper losses in multi-winding transformers represented by mesh network is not a trivial task: here an example on six coil transformer was given;

- Different PWM techniques were discussed in order to identify the most suitable one for the particular application in EV dc charging stations;

- Transformer model identification and losses estimation was done by following classical mathematical approach, which is not very complex to be implemented in Matlab or other commercial software. Therefore the procedure is suitable for engineers working in transformer manufacturing industry to perform fast calculations and will help them to obtain satisfactory results;

- Thermal validation procedure previously established for unbalanced load on two-winding transformers was adapted for a case of unbalanced secondary loads on a multi-winding transformer.

The future work on the same topic may include:

- Time domain simulation of the same system topology in order to validate the results obtained analytically in phasor domain;

- Scaled prototype of the four coil transformer so as to verify its performances;

- Another possible coils disposition to be analyzed for the same application;

- Variations of the power conversion system and results comparison;

- Improving the transformer design by employing some of the optimization techniques;

- Discussion on different insulation materials in distorted operating conditions as well as defining the distances between the transformer coils in a more precise way;

- Detailed estimation of the system reliability with different coils dispositions.

Appendix 1: Transformer with concentric coils design procedure

1. Transformer rated data

Rated apparent power of the primary winding	S_{1n}	1000	kVA
Rated apparent power on the secondary winding	S_{2n}	333.33	kVA
Rated primary voltage	V_{1n}	20	kV
Rated secondary voltage	V_{2n}	0.4	kV
Vector group		Yy	
Rated frequency	f_n	50	Hz

2. Basic input data:

Rated primary current	$I_{1n} = \dfrac{S_{1n}}{\sqrt{3}V_{1n}}$	28.87	A
Rated primary phase current	$I_{1nf} = I_{1n}$	28.87	A
Rated secondary current	$I_{2n} = \dfrac{S_{2n}}{\sqrt{3}V_{2n}}$	481.12	A
Rated secondary phase current	$I_{2nf} = I_{2n}$	481.12	A
Rated primary phase voltage	$V_{1nf} = V_{1n}$	20,000	V
Rated secondary phase voltage	$V_{2nf} = \dfrac{V_{2n}}{\sqrt{3}}$	231	V
Coefficient of induced voltage per turn	$K = 0.37 - 0.45$	0.4427	
Induced voltage per turn	$E_{turn} = K\sqrt{S_{1n}}$	14.0	V/turn
Number of primary turns	$N_1 = \dfrac{V_{2n}}{\sqrt{3}E_{turn}}$	693	turns
Number of secondary turns	$N_2 = \dfrac{V_{1n}}{V_{2n}}$	16	turns

3. High voltage winding design

Recommended current density	$g_{1,r} = 2.6 - 3.8$	3	A/mm^2
Recommended conductor area	$S_{cu1,r} = \dfrac{I_{1nf}}{g_1}$	9.62	mm^2
Recommended conductor diameter	$d_{1,r} = \sqrt{\dfrac{4S_{cu1}}{\pi}}$	3.5	mm
Accepted diameter of bare conductor	d_1 – catalogue choice	3.35	mm

Wire insulation	i_{10} – catalogue value (enameled copper wire)	0.129	mm
Diameter of isolated conductor	$d_{1,is} = d_1 + i_{10}$	3.479	mm
Accepted bare conductor area	$S_{cu1} = \dfrac{\pi d_1^2}{4}$	8.81	mm²
Accepted insulated conductor area	$S_{cu1,is} = \dfrac{\pi d_{1,is}^2}{4}$	9.51	mm²
Working current density	$g_1 = \dfrac{I_{1nf}}{S_{cu1}}$	3.28	A/mm²
Number of coils	Nc	1	
Number of turns per coil	$N_{t/c} = \dfrac{N_1}{N_c}$	693	
Number of layers in radial direction	$N_l = 7 - 19$	9	
Recommended number of turns in a layer	$N_{t/l,r} = \dfrac{N_{t/c}}{N_l}$	77	
Accepted number of turns in a layer	$N_{t/l}$ – rounded on the next integer value	77	
Width of the insulation paper between layers	d_{np} – catalogue; natron paper	0.05	mm
Width of interlayer insulation	$\delta_{is,r} = \dfrac{2N_{t/l}E_{turn}}{9000}$	0.48	mm
Rounded width of interlayer insulation	δ_{is}	0.30	mm
Number of insulation paper layers between two conductor layers (radially)	$N_{ip} = \dfrac{\delta_{is}}{d_{np}}$	6	
Distance between two neighbouring conductors	$d_{bc} = 0.01 - 0.04$ – due to manufacturing	0.04	mm
Axial duct width	$\delta_{ad1} = 4 - 6$	5	mm
Insulation paper top/bottom rings	$h_{ir} = 15 - 30$	24	mm
Winding electrical height	$h_{1,el} = d_{1,is}N_{t/l} + (N_{t/l} - 1)d_{bc}$	271	mm
High voltage winding total height	$h_1 = h_{1,el} + 2h_{ir}$	295	mm
High voltage winding total width	$a_1 = N_l d_{1,is} + (N_l - 1)N_{ip}d_{np} + \delta_{ad1}$	39	mm
Distance between HV winding – yoke	$v_1 \geq 40$	40	mm
Column height	$H = h_1 + 2v_1$	375	mm

4. Low voltage winding design

Assumed current density	$g_{2,r} = 2.6 - 3.8$	3	A/mm^2
Recommended conductor area	$S_{cu2,r} = \dfrac{I_{2nf}}{g_2}$	160.37	A/mm^2
Number of elementary conductors	$N_c = 1, 2, 4, 6.$	4	
Disposition of elementary conductors	$N_{ax} \times N_{rad}$	2 x 2	
Recommended area of elementary conductor	$S_{cu2,el,r} = \dfrac{S_{cu2,r}}{N_c}$	40.09	mm^2
Distance between LV winding – yoke	$v_{2,r} \geq 30$	30	mm
Available winding height	$H_{2,av} = H - 2v_{2,r}$	315	mm
Number of layers	$N_l = 1$ or 2.	1	
Number of turns per layer	$N_{t/l} = \dfrac{N_2}{N_l}$	16	
Recommended height of isolated package of elementary conductors	$p_{is,r} = \dfrac{H_{2,av}}{N_{t/l} + 1}$	18.53	mm
Isolation of elementary conductor	$i_{20} = 0.5 - 0.6$ – paper insulation	0.5	mm
Recommended height of elementary conductor	$p_{e,r} = \dfrac{p_{is,r} - N_{ax}i_{20}}{N_{ax}}$	8.76	mm
Adopted height of elementary conductor	p_e – catalogue choice	7.5	mm
Recommended width of elementary conductor	$q_{e,r} = \dfrac{S_{cu2,r}}{p_e}$	4.86	mm
Adopted width of elementary conductor	q_e – catalogue choice	5.0	mm
Height of insulated package	$p_{is} = (p_e + i_{20})N_{ax}$	16	mm
Width of insulated package	$q_{is} = (q_e + i_{20})N_{rad}$	11	mm
Coefficient of area reduction	k = 0.96-0.99 – due to curvatures on the angles	0.9771	
Area of bare package	$S_{cu2} = kN_c p_e q_e$	146.56	mm^2
Working current density	$g_2 = \dfrac{I_{2nf}}{S_{cu2}}$	3.28	A/mm^2
Distance between neighbouring conductors	$d_{bc} = 0.01 - 0.04$, due to manufacturing	0.04	mm
Insulation paper top/bottom ring	h_{ir} – presspaper	11	mm
Electric winding height	$h_{2,el} = (N_{c/l} + 1)p_{is} + N_{c/l}d_{bc}$	273	mm
Low voltage winding total height	$h_2 = h_{2,el} + 2h_{ir}$	295	mm

Low voltage winding total width	$a_2 = N_l q_{is}$	11	mm
Real distance between LV winding - yoke	$v_2 = H - h_2$	40	mm

5. Core design

Induced voltage per turn	E_{turn}	14.0	V/turn
Recommended flux density	$B_m = 1.6 - 1.8$	1.66	T
Stacking coefficient	$K_{fe} = 0.945 - 0.980$	0.957	
Recommended core gross cross section area	$S_{fe,gross,r} = \dfrac{E_{turn} 10^2}{2.22 B_m K_{fe}}$	396.97	cm^2
Geometrical coefficient	$\alpha(n) = 0.63 - 0.945$ – depends on the number of core steps (from 1 to 11 steps)	0.95	
Diameter of the column circumference	$d = \sqrt{\dfrac{4 S_{fe,gross,r}}{\pi \alpha}} 100$	231	mm
Recommended core net cross section area	$S_{fe,net,r} = \alpha S_{fe,gross,r}$	377.12	cm^2
Length of the core laminations	The length of 1st step is chosen based on core diameter, the others are decreasing by 10 or 20 mm respectively 220 / 210 / 200 / 190 / 180 / 170 / 160 / 140 / 120 / 100 / 70		mm
Width of core laminations	$b_i = \sqrt{d^2 - A_i^2} - \sum_{j=1}^{i-1} b_j$ 70.45 / 25.8 / 19.35 / 15.8 / 13.4 / 11.6 / 10.2 / 17 / 13.65 / 10.85 / 12		mm
Core gross cross section area	$S_{fe,gross} = \sum_{i=1}^{n} A_i b_i 10^{-2}$	397.6	cm^2
Core net cross section area	$S_{fe,net} = K_{fe} S_{fe,gross}$	380.5	cm^2
Distance: column – LV winding	$\delta_{20} = 4 - 6$	4	mm
Distance: LV-LV winding of the same phase	$\delta_{22} = 10 - 14$	14	mm
Distance LV-HV winding	$\delta_{12} = 14 - 17$	14	mm
Distance HV-HV winding of different phases	$\delta_{11} \geq 14$	18	mm
Column centres distance	$l_c = d + 2a_1 + 6a_2 + 2(\delta_{20} + \delta_{12}) + 4\delta_{22} + \delta_{11}$	485	mm
Total core length	$L_c = 2l_c + A_1$	1190	mm
Total core height	$H_c = H + 2A_1$	815	mm
Iron per unit mass	γ_{fe}	7650	kg/m^3

Calculated core mass	$m_{c,calc} = [3H + 4l_c + 2 \cdot 0.86 A_1] S_{fe,gross} 0.97 \gamma_{fe} 10^{-7}$	1016	kg
Working flux density	$B_m = \dfrac{E_{turn} 10^4}{4.44 f S_{fe,net}}$	1.657	T

6. Winding data and copper losses

Copper specific mass	γ_{Cu}	8960	kg/m³
Copper specific resistance at 20oC	ρ_{Cu}	1.68·10⁻⁵	Ωmm
LV winding 1 internal diameter	$D_{1,INT} = d + 2\delta_{20}$	239	mm
LV winding 1 external diameter	$D_{1,EXT} = D_{1,INT} + 2a_2$	261	mm
LV winding 1 average diameter	$D_{1,AV} = D_{1,INT} + a_2$	250	mm
Average turn length of LV winding 1	$l_{1,AV} = \pi D_{1,AV}$	785	mm
Length of the LV winding 1 connections to the bushings	$l_{con1} = 1,000 - 1,400$	1,200	mm
Total length of conductor for LV winding 1	$L_{1,TOT} = N_2 l_{1,AV} + l_{con1}$	13,760	mm
LV winding 1 copper mass	$m_{Cu,1} = 1.05 \gamma_{Cu} L_{1,TOT} S_{Cu,2} 10^{-9}$	19.05	kg
LV winding 2 internal diameter	$D_{2,INT} = D_{1,EXT} + 2\delta_{22}$	289	mm
LV winding 2 external diameter	$D_{2,EXT} = D_{2,INT} + 2a_2$	311	mm
LV winding 2 average diameter	$D_{2,AV} = D_{2,INT} + a_2$	300	mm
Average turn length of LV winding 2	$l_{2,AV} = \pi D_{2,AV}$	942	mm
Length of the LV winding 2 connections to the bushings	$l_{con2} = 1,000 - 1,400$	1,200	mm
Total length of conductor for LV winding 2	$L_{2,TOT} = N_2 l_{2,AV} + l_{con2}$	16,272	mm
LV winding 2 copper mass	$m_{Cu,2} = 1.05 \gamma_{Cu} L_{2,TOT} S_{Cu,2} 10^{-9}$	22.52	kg
LV winding 3 internal diameter	$D_{3,INT} = D_{2,EXT} + 2\delta_{22}$	339	mm
LV winding 3 external diameter	$D_{3,EXT} = D_{3,INT} + 2a_2$	361	mm
LV winding 3 average diameter	$D_{3,AV} = D_{3,INT} + a_2$	350	mm
Average turn length of LV winding 3	$l_{3,AV} = \pi D_{3,AV}$	1,099	mm
Length of the LV winding 3 connections to the bushings	$l_{con3} = 1,000 - 1,400$	1,200	mm
Total length of conductor for LV winding 3	$L_{3,TOT} = N_2 l_{3,AV} + l_{con3}$	18,784	mm
LV winding 3 copper mass	$m_{Cu,3} = 1.05 \gamma_{Cu} L_{3,TOT} S_{Cu,2} 10^{-9}$	26.0	kg
HV winding internal diameter	$D_{4,INT} = D_{3,EXT} + 2\delta_{12}$	389	mm

HV winding external diameter	$D_{4,EXT} = D_{4,INT} + 2a_1$	467	mm
HV winding average diameter	$D_{4,AV} = D_{4,INT} + a_1$	428	mm
Average turn length of HV winding	$l_{4,AV} = \pi D_{4,AV}$	1,344.6	mm
Length of the HV winding connections to the bushings	$l_{con4} = 300 - 800$	500	mm
Total length of conductor for HV winding	$L_{4,TOT} = N_1 l_{4,AV} + l_{con4}$	932,308.2	mm
HV winding copper mass	$m_{Cu,4} = 1.05 \gamma_{Cu} L_{4,TOT} S_{Cu,1} 10^{-9}$	77.23	kg

Appendix 2: Transformer with stacked coils design procedure

1. Transformer rated data

Rated apparent power of the primary winding	S_{1n}	333.33	kVA
Rated apparent power on the secondary winding	S_{2n}	333.33	kVA
Rated primary voltage	V_{1n}	20	kV
Rated secondary voltage	V_{2n}	0.4	kV
Vector group		Yy	
Rated frequency	f_n	50	Hz

2. Basic input data

Rated primary current	$I_{1n} = \dfrac{S_{1n}}{\sqrt{3}V_{1n}}$	9.62	A
Rated primary phase current	$I_{1nf} = I_{1n}$	9.62	A
Rated secondary current	$I_{2n} = \dfrac{S_{2n}}{\sqrt{3}V_{2n}}$	481.12	A
Rated secondary phase current	$I_{2nf} = I_{2n}$	481.12	A
Rated primary phase voltage	$V_{1nf} = V_{1n}$	20,000	V
Rated secondary phase voltage	$V_{2nf} = \dfrac{V_{2n}}{\sqrt{3}}$	231	V
Coefficient of induced voltage per turn	$K = 0.37 - 0.45$	0.4287	
Induced voltage per turn	$E_{turn} = K\sqrt{S_{1n}}$	7.827	V/turn
Number of secondary turns	$N_2 = \dfrac{V_{2n}}{\sqrt{3}E_{turn}}$	1299	turns
Number of primary turns	$N_1 = \dfrac{V_{1n}}{V_{2n}}$	30	turns

3. High voltage winding design

Recommended current density	$g_{1,r} = 2.6 - 3.8$	3.4	A/mm^2
Recommended conductor area	$S_{cu1,r} = \dfrac{I_{1nf}}{g_1}$	2.83	mm^2
Recommended conductor diameter	$d_{1,r} = \sqrt{\dfrac{4S_{cu1}}{\pi}}$	1.9	mm
Accepted diameter of bare conductor	d_1 – catalogue choice	1.9	mm

Wire insulation	i_{10} – catalogue value (enameled copper wire)	0.112	mm
Diameter of isolated conductor	$d_{1,is} = d_1 + i_{10}$	2.012	mm
Accepted bare conductor area	$S_{cu1} = \dfrac{\pi d_1^2}{4}$	2.84	mm^2
Accepted insulated conductor area	$S_{cu1,is} = \dfrac{\pi d_{1,is}^2}{4}$	3.18	mm^2
Working current density	$g_1 = \dfrac{I_{1nf}}{S_{cu1}}$	3.39	A/mm^2
Number of coils	Nc	1	
Number of turns per coil	$N_{t/c} = \dfrac{N_1}{N_c}$	1299	
Number of layers in radial direction	$N_l = 7 - 19$	15	
Recommended number of turns in a layer	$N_{t/l,r} = \dfrac{N_{t/c}}{N_l}$	86.6	
Accepted number of turns in a layer	$N_{t/l}$ – rounded on the next integer value	87	
Width of the insulation paper between layers	d_{np} – catalogue; natron paper	0.05	mm
Width of interlayer insulation	$\delta_{is,r} = \dfrac{2N_{t/l}E_{turn}}{9000}$	0.30	mm
Rounded width of interlayer insulation	δ_{is}	0.25	mm
Number of insulation paper layers between two conductor layers (radially)	$N_{ip} = \dfrac{\delta_{is}}{d_{np}}$	5	
Distance between two neighbouring conductors	$d_{bc} = 0.01 - 0.04$ – due to manufacturing	0.03	mm
Axial duct width	$\delta_{ad1} = 4 - 6$	4	mm
Insulation paper top/bottom rings	$h_{ir} = 5 - 30$	6	mm
Winding electrical height	$h_{1,el} = d_{1,is}N_{t/l} + (N_{t/l} - 1)d_{bc}$	178	mm
High voltage winding total height	$h_1 = h_{1,el} + 2h_{ir}$	190	mm
High voltage winding total width	$a_1 = N_l d_{1,is} + (N_l - 1)N_{ip}d_{np} + \delta_{ad1}$	38	mm
Distance between HV winding – yoke	$v_1 \geq 40$	40	mm
Axial distance HV-HV winding of the same phase*	$\delta_{11,AX} \geq 14$	15	mm
Column height	$H = 3h_1 + 2\delta_{11,AX} + 2v_1$	680	mm

*The axial distance between two HV windings of the same phase is chosen following the recommendations for the radial distance between the HV windings of two different phases, i.e., $\delta_{11} \geq 14$ mm.

4. Low voltage winding design

Assumed current density	$g_{2,r} = 2.6 - 3.8$	3.4	A/mm^2
Recommended conductor area	$S_{cu2,r} = \dfrac{I_{2nf}}{g_2}$	141.51	A/mm^2
Number of elementary conductors	$N_c = 1, 2, 4, 6.$	4	
Disposition of elementary conductors	$N_{ax} \times N_{rad}$	2 x 2	
Recommended area of elementary conductor	$S_{cu2,el,r} = \dfrac{S_{cu2,r}}{N_c}$	35.38	mm^2
Distance between LV winding – yoke	$v_{2,r} \geq 30$	30	mm
Available winding height	$H_{2,av} = \left(H - 2v_{2,r} - 2\delta_{22,AX}\right)/3$	196.67	mm
Number of layers	$N_l = 1, 2$ or 3.	3	
Number of turns per layer	$N_{t/l} = \dfrac{N_2}{N_l}$	10	
Recommended height of isolated package of elementary conductors	$p_{is,r} = \dfrac{H_{2,av}}{N_{t/l} + 1}$	17.879	mm
Isolation of elementary conductor	$i_{20} = 0.5 - 0.6$ – paper insulation	0.5	mm
Recommended height of elementary conductor	$p_{e,r} = \dfrac{p_{is,r} - N_{ax}i_{20}}{N_{ax}}$	8.439	mm
Adopted height of elementary conductor	p_e – catalogue choice	7.1	mm
Recommended width of elementary conductor	$q_{e,r} = \dfrac{S_{cu2,r}}{p_e}$	4.983	mm
Adopted width of elementary conductor	q_e – catalogue choice	5.3	mm
Height of insulated package	$p_{is} = (p_e + i_{20})N_{ax}$	15.2	mm
Width of insulated package	$q_{is} = (q_e + i_{20})N_{rad}$	11.6	mm
Coefficient of area reduction	$k = 0.96\text{-}0.99$ – due to curvatures on the angles	0.9688	
Area of bare package	$S_{cu2} = kN_c p_e q_e$	145.84	mm^2
Working current density	$g_2 = \dfrac{I_{2nf}}{S_{cu2}}$	3.3	A/mm^2
Distance between neighbouring conductors	$d_{bc} = 0.01 - 0.04$, due to manufacturing	0.04	mm
Insulation paper top/bottom ring	h_{ir} – presspaper	11	mm
Electric winding height	$h_{2,el} = \left(N_{c/l} + 1\right)p_{is} + N_{c/l}d_{bc}$	168	mm
Low voltage winding total height	$h_2 = h_{2,el} + 2h_{ir}$	190	mm

Width of interlayer insulation	$\delta_{is,r} = \dfrac{2N_{t/l}E_{turn}}{9000}$	0.035	mm
Rounded width of interlayer insulation	δ_{is} – 1 layer of diamond dotted presspaper	0.25	mm
Number of insulation paper layers between two conductor layers (radially)	$N_{ip} = \dfrac{\delta_{is}}{d_{np}}$	1	
Axial duct width	$\delta_{ad2} = 3 - 6$ (1 duct after each conductor layer, 2 ducts in total)	3	mm
Low voltage winding total width	$a_2 = N_l q_{is} + (N_l - 1)\delta_{iz} + 2\delta_{ad2}$	41	mm
Axial distance LV-LV winding of different phases[*]	$\delta_{22,AX} \geq 14$	15	mm
Real distance between LV winding - yoke	$v_2 = \left(H - 3h_2 - 2\delta_{22,AX}\right)/2$	40	mm

* The axial distance between two LV windings of different phases is taken to be equal to the axial distance of two HV windings of the same phase, in order to align axially the pairs HV-LV winding.

5. Core design

Induced voltage per turn	E_{turn}	7.827	V/turn
Recommended flux density	$B_m = 1.6 - 1.8$	1.65	T
Stacking coefficient	$K_{fe} = 0.945 - 0.980$	0.957	
Recommended core gross cross section area	$S_{fe,gross,r} = \dfrac{E_{turn}10^2}{2.22 B_m K_{fe}}$	223.28	cm^2
Geometrical coefficient	$\alpha(n) = 0.63 - 0.945$ – depends on the number of core steps (from 1 to 11 steps)	0.95	
Diameter of the column circumference	$d = \sqrt{\dfrac{4S_{fe,gross,r}}{\pi\alpha}}\,100$	173	mm
Recommended core net cross section area	$S_{fe,net,r} = \alpha S_{fe,gross,r}$	212.12	cm^2
Length of the core laminations	The length of 1st step is chosen based on core diameter, the others are decreasing by 10 or 20 mm respectively 170 / 160 / 150 / 140 / 130 / 120 / 100 / 90 / 70		mm
Width of core laminations	$b_i = \sqrt{d^2 - A_i^2} - \sum\limits_{j=1}^{i-1} b_j$ 32 / 33.7 / 20.4 / 15.4 / 12.5 / 10.5 / 16.5 / 6.5 / 10.5		mm
Core gross cross section area	$S_{fe,gross} = \sum\limits_{i=1}^{n} A_i b_i 10^{-2}$	219.32	cm^2
Core net cross section area	$S_{fe,net} = K_{fe} S_{fe,gross}$	209.9	cm^2
Distance: column – LV winding	$\delta_{20} = 4 - 6$	5	mm

Distance LV-HV winding	$\delta_{12} = 14 - 17$ (pressboard insulation cylinder of 2 mm width in between)	14	mm
Distance HV-HV winding of different phases	$\delta_{11} \geq 14$	15	mm
Column centres distance	$l_c = d + 2a_1 + 2a_2 + 2\delta_{20} + 2\delta_{12} + \delta_{11}$	385	mm
Total core length	$L_c = 2l_c + A_1$	940	mm
Total core height	$H_c = H + 2A_1$	1020	mm
Iron per unit mass	γ_{fe}	7650	kg/m³
Calculated core mass	$m_{c,calc} = \left[3H + 4l_c + 2 \cdot 0.86A_1\right]S_{fe,gross}0.97\gamma_{fe}10^{-7}$	630.2	kg
Working flux density	$B_m = \dfrac{E_{turn}10^4}{4.44\,fS_{fe,net}}$	1.68	T

6. Insulation distances recommendations and choices

Distance [mm]	Symbol	Interval	Choice
Radial distance: column – LV winding	δ_{20}	4 - 6	5
Radial distance LV-HV winding	δ_{12}	14 – 17	14
Radial distance HV-HV winding of different phases	δ_{11}	≥ 14	15
Axial distance: LV-LV winding of different phases	$\delta_{22,AX}$	10 – 14	15
Axial distance: HV-HV winding of the same phase	$\delta_{11,AX}$	≥ 14	15
Axial distance LV winding - yoke	v_2	≥ 30	40
Axial distance HV winding - yoke	v_1	≥ 40	40

7. Winding data and copper losses

Copper specific mass	γ_{Cu}	8960	kg/m³
Copper specific resistance at 20oC	ρ_{Cu}	$1.68 \cdot 10^{-5}$	Ωmm
LV winding internal diameter	$D_{2,INT} = d + 2\delta_{20}$	183	mm
LV winding external diameter	$D_{2,EXT} = D_{2,INT} + 2a_2$	265	mm
LV winding average diameter	$D_{2,AV} = D_{2,INT} + a_2$	224	mm
Average turn length of LV winding 1	$l_{2,AV} = \pi D_{2,AV}$	703.36	mm
Length of the LV winding connections to the bushings	$l_{con2} = 1,000 - 1,400$	1,200	mm
Total length of conductor for LV winding 1	$L_{2,TOT} = N_2 l_{2,AV} + l_{con2}$	22,300	mm
LV winding copper mass	$m_{Cu,2} = 1.05\gamma_{Cu}L_{2,TOT}S_{Cu,2}10^{-9}$	30.72	kg
HV winding internal diameter	$D_{1,INT} = D_{2,EXT} + 2\delta_{12}$	281	mm

HV winding external diameter	$D_{1,EXT} = D_{1,INT} + 2a_1$	357	mm
HV winding average diameter	$D_{1,AV} = D_{1,INT} + a_1$	319	mm
Average turn length of HV winding	$l_{1,AV} = \pi D_{1,AV}$	1001.66	mm
Length of the HV winding connections to the bushings	$l_{con1} = 300 - 800$	500	mm
Total length of conductor for HV winding	$L_{1,TOT} = N_1 l_{1,AV} + l_{con1}$	1,301,656	mm
HV winding copper mass	$m_{Cu,1} = 1.05 \gamma_{Cu} L_{1,TOT} S_{Cu,1} 10^{-9}$	34.77	kg

Appendix 3: Four coil transformer binary short-circuit impedances

1. Binary short-circuit inductance L_{ij} when coil i is supplied and coil j is short-circuited can be calculated using the equation [52]:

$$L_{ij} = k_L p_{ij} c_{ij} K_{Rij} ,$$

where k_L is a common factor, p_{ij} is the average perimeter of the hollow between the observed coils, c_{ij} is distance between electromagnetic centres and K_{Rij} is the Rogowski factor.

In case of four winding transformer, with concentric disposition of the coils and referring to the geometry shown in Figure 35, the following expressions should be used for calculating the binary inductances:

- Common coefficient $k_L = \mu_o \dfrac{N_2^2}{h_1}$

- Distance between electromagnetic centres [mm]:

$c_{12} = \delta_{22} + \dfrac{a_2 + a_2}{3}$	$c_{13} = \delta_{22} + a_2 + \delta_{22} + \dfrac{a_2 + a_2}{3}$
$c_{14} = \delta_{22} + a_2 + \delta_{22} + a_2 + \delta_{21} + \dfrac{a_1 + a_2}{3}$	$c_{23} = \delta_{22} + \dfrac{a_2 + a_2}{3}$
$c_{24} = \delta_{22} + a_2 + \delta_{12} + \dfrac{a_1 + a_2}{3}$	$c_{34} = \delta_{12} + \dfrac{a_2 + a_1}{3}$

- Rogowski coefficient: $K_R(\sigma_R) = 1 - \dfrac{1}{\sigma_R}\left(1 - e^{-\sigma_R}\right)$

$\sigma_{R12} = \dfrac{\pi h_1}{2\delta_{22} + a_2 + a_2}$	$\sigma_{R13} = \dfrac{\pi h_1}{2(\delta_{22} + a_2 + \delta_{22}) + a_2 + a_2}$
$\sigma_{R14} = \dfrac{\pi h_1}{2(\delta_{22} + a_2 + \delta_{22} + a_2 + \delta_{12}) + a_2 + a_1}$	$\sigma_{R23} = \dfrac{\pi h_1}{2\delta_{22} + a_2 + a_2}$
$\sigma_{R24} = \dfrac{\pi h_1}{2(\delta_{22} + a_2 + \delta_{12}) + a_1 + a_2}$	$\sigma_{R34} = \dfrac{\pi h_1}{2\delta_{12} + a_2 + a_1}$

- Average perimeter [mm]:

$p_{12} = 2\pi r_{12} = 2\pi\left(\dfrac{d}{2} + \delta_{20} + \dfrac{a_2}{2} + \dfrac{\delta_{22}}{2}\right)$	$p_{13} = 2\pi r_{13} = 2\pi\left(r_{12} + \dfrac{a_2 + \delta_{22}}{2}\right)$

$p_{14} = 2\,\pi\,r_{14} = 2\pi\left(r_{13} + \dfrac{a_2 + \delta_{12}}{2}\right)$	$p_{23} = 2\,\pi\,r_{23} = 2\pi\left(\dfrac{d}{2} + \delta_{20} + a_2 + \delta_{22} + a_2 + \dfrac{\delta_{22}}{2}\right)$
$p_{24} = 2\,\pi\,r_{24} = 2\pi\left(r_{23} + \dfrac{a_2 + \delta_{12}}{2}\right)$	$p_{34} = 2\,\pi\,r_{34} = 2\pi\left(r_{24} + \dfrac{\delta_{22} + a_2}{2}\right)$

Using the previous expressions, following results are obtained:

c_{12} [mm]	c_{13} [mm]	c_{14} [mm]	c_{23} [mm]	c_{24} [mm]	c_{34} [mm]
21.33	46.33	80.66	21.33	55.66	30.66
p_{12} [mm]	p_{13} [mm]	p_{14} [mm]	p_{23} [mm]	p_{24} [mm]	p_{34} [mm]
863.94	942.48	1021.02	1021.02	1099.56	1178.10
σ_{12}	σ_{13}	σ_{14}	σ_{23}	σ_{24}	σ_{34}
18.535	8.743	5.207	18.535	7.240	11.882
k_{R12}	k_{R13}	k_{R14}	k_{R23}	k_{R24}	k_{R34}
0.9460	0.8856	0.8090	0.9460	0.8620	0.9158
L_{12} [μH]	L_{13} [μH]	L_{14} [μH]	L_{23} [μH]	L_{24} [μH]	L_{34} [μH]
19.014	**42.175**	**72.660**	**22.472**	**57.536**	**36.082**

2. Binary short-circuit resistances take into account coil dc copper losses, as well as the additional losses occurring due to the skin effect (in the coils i and j, and in all the other open-ended coils which are placed between them).

- Ohmic resistance of the windings:

$$R_{i,\Omega}(75^o\,C) = \rho_{Cu}\left(75^o\,C\right)\frac{p_i \cdot N_i}{S_{Cu,i}}, \quad i = 1, 2, 3, 4,$$

where p_i is the average perimeter of the ith coil, N_i is the number of turns, $S_{Cu,i}$ is the cross section of elementary conductor and ρ_{Cu} is the specific copper resistance. As a normal transformer operating temperature is considered to be 75°C. The average coil perimeters can be calculated as:

$p_1 = 2\,\pi\,r_1 = 2\pi\left(\dfrac{d}{2} + \delta_{20} + \dfrac{a_2}{2}\right)$	$p_2 = 2\,\pi\,r_2 = 2\pi\left(r_1 + \delta_{22} + \dfrac{a_2 + a_2}{2}\right)$
$p_3 = 2\,\pi\,r_3 = 2\pi\left(r_2 + \delta_{22} + \dfrac{a_2 + a_2}{2}\right)$	$p_4 = 2\,\pi\,r_4 = 2\pi\left(r_3 + \delta_{12} + \dfrac{a_2 + a_1}{2}\right)$

- Additional copper losses are encountered for by the coefficient k_a with a general expression:

$$K_a = \varphi_a(\xi) + \frac{m^2 - 1}{3} \psi_a(\xi),$$

where m is the number of total elementary conductors in a radial direction, normal to the leakage flux, $\varphi_a(\xi)$ and $\psi_a(\xi)$ are functions of the auxiliary variable ξ; their meanings are explained in the following.

- Auxiliary variable ξ has a physical meaning of skin depth:

$$\xi_{LV}(f) = w_{LV} \sqrt{\pi \sigma_{Cu} f \mu_o \frac{h_r}{h_a}}$$

$$\xi_{HV}(f) = w_{HV} \sqrt{\pi \sigma_{Cu} f \mu_o \frac{h_r}{h_a}},$$

where the widths of the elementary conductors are $w_{LV} = q_e$ (elementary conductor radial length) and $w_{HV} = d$ (diameter of bare conductor). For each winding, h_{net} and h_{tot} are the copper net coil height and total coil height respectively.

- Auxiliary function $\varphi_a(\xi)$ takes into account the additional losses in an elementary conductor produced by the current in the conductor itself, thus assuming no current in all the other conductors. This is a self-produced effect which includes the main losses [69].

$$\varphi_a(\xi) = \xi \frac{\sinh(2\xi) + \sin(2\xi)}{\cosh(2\xi) - \cos(2\xi)}$$

- Auxiliary function $\psi_a(\xi)$ takes into account the losses in the kth elementary conductor produced by the leakage field generated by the currents in all the other conductors (form the 1st up to the $k\text{-}1^{th}$), thus assuming no current in the kth elementary conductor. This is a mutually produced effect which does not include the main losses.

$$\psi_a(\xi) = 2\xi \frac{\sinh(\xi) - \sin(\xi)}{\cosh(\xi) + \cos(\xi)}$$

- The coefficient $(m^2 - 1)/3$ takes into account all the mutual additional losses due to $\psi_a(\xi)$, i.e., the mutual additional losses in all the m elementary conductors.

Considering the four coil transformer designed here, the additional copper loss coefficients can be obtained as:

$$K_{ai} = \varphi_a(\xi_{LV}) + \frac{(N_{l,LV} N_{rad})^2 - 1}{3} \psi_a(\xi_{LV}), \quad i = 1,2,.3.$$

$$K_{a2p} = K_{a3p} = \left(N_{l,LV} N_{rad}\right)^2 \psi_a\left(\xi_{LV}\right)$$

$$K_{a4} = \varphi_a\left(\xi_{HV}\right) + \frac{\left(N_{l,HV}\right)^2 - 1}{3} \psi_a\left(\xi_{HV}\right),$$

where $N_{l,LV}$ and $N_{l,HV}$ are the number of conductor layers in radial direction of the low voltage and high voltage windings respectively.

Finally, the expressions for the binary short-circuit resistances are:

$$R_{12} = K_{a1} R_{1\Omega} + K_{a2} R_{2\Omega}$$

$$R_{13} = K_{a1} R_{1\Omega} + K_{a2p} R_{2\Omega} + K_{a3} R_{3\Omega}$$

$$R_{14} = K_{a1} R_{1\Omega} + K_{a2p} R_{2\Omega} + K_{a3p} R_{3\Omega} + K_{a4} R_{4\Omega}$$

$$R_{23} = K_{a2} R_{2\Omega} + K_{a3} R_{3\Omega}$$

$$R_{24} = K_{a2} R_{2\Omega} + K_{a3p} R_{3\Omega} + K_{a4} R_{4\Omega}$$

$$R_{34} = K_{a3} R_{3\Omega} + K_{a4} R_{4\Omega}$$

By using the previous analytical procedure, the following results are obtained:

Ohmic resistance R [mΩ]	$R_{1\Omega}$ = 1.9175	$R_{2\Omega}$ = 2.2676
	$R_{3\Omega}$ = 2.6176	R'$_{4\Omega}$ = 1.1521

	LV coil	HV coil
Auxiliary coefficient ξ	0.477848	0.318984
Auxiliary function $\varphi_a(\xi)$	1.004625	1.000920
Auxiliary function $\psi_a(\xi)$	0.017343	0.003450

Additional loss coefficients	
$K_{a1} = K_{a2} = K_{a3}$	1.02197
$K_{a2p} = K_{a3p}$	0.06937
K_{a4}	1.09291

Binary short-circuit resistances are:

R_{12} [mΩ]	R_{13} [mΩ]	R_{14} [mΩ]	R_{23} [mΩ]	R_{24} [mΩ]	R_{34} [mΩ]
4.277	4.792	3.558	4.992	3.758	3.934

Using the previous values, we can calculate: $\overline{Z_{ij}} = R_{ij} + j\omega L_{ij}$.

Appendix 4: Six coil transformer binary short-circuit impedances and mesh network branch impedances

1. Axial component of the binary short-circuit inductance can be calculated as [65], [79]:

$$L_{ij}^z = \underbrace{\frac{\mu_o \pi N_o^2}{(h_i + h_j)/2}}_{K_{Rog}^z} \left(\frac{a_i D_{i,AV}}{3} + \delta_{ij} D_{ij,AV} + \frac{a_j D_{j,AV}}{3} \right),$$

where h_i and h_j are coils heights, $D_{i,AV}$ and $D_{j,AV}$ are coils average diameters, a_i and a_j are coils widths, $D_{ij,AV}$ is the diameter of the hollow between the coils, δ_{ij} is the radial distance between the coils. The Rogowski factor can be evaluated as:

$$K_{Rog}^z = 1 - \frac{1 - e^{-\sigma_{R,ij}^z}}{\sigma_{R,ij}^z}, \text{ where } \sigma_{R,ij}^z = \frac{\pi(h_i + h_j)/2}{a_i + \delta_{ij} + a_j}.$$

Referring to the six coil transformer (Figure 35 right), the coil pairs are obtained for: $i = 1, 3, 5$ and $j = 2, 4, 6$. Since in the six-coil transformer design presented in this work the radial distance between the coil pairs is $\delta_{ij} = \delta_{12}$ and both low and high voltage windings have equal heights, the Rogowski coefficient which is related to the flux fringing the top and bottom of the coils (due to the axial flux component) is the same for all ij pairs:

$$\sigma_{R,ij}^z = \frac{\pi h_1}{a_2 + \delta_{12} + a_1} = 6.418307$$

$$K_{Rog}^z = 1 - \frac{1 - e^{-\sigma_{R,ij}^z}}{\sigma_{R,ij}^z} = 0.84445$$

$$L_{ij}^z = \frac{\mu_o \pi N_o^2 K_{Rog}^z}{h_1} \left(\frac{a_1 D_{1,AV}}{3} + \delta_{12} D_{12} + \frac{a_2 D_{2,AV}}{3} \right) = 173.833 \ \mu H$$

2. Radial component of the binary short-circuit inductance can be calculated as:

$$L_{ij}^r = \underbrace{\frac{\mu_o \pi N_o^2 D_{ij,AV}}{(a_i + a_j)/2}}_{K_{Rog}^r} \left(\frac{a_i}{3} + \delta_{ij,ax} + \frac{a_j}{3} \right),$$

where the Rogowski factor is evaluated as:

$$K_{Rog}^r = 1 - \frac{1 - e^{-\sigma_{R,ij}^r}}{\sigma_{R,ij}^r} \text{ and } \sigma_{R,ij}^r = \frac{\pi(a_i + a_j)/2}{h_i + \delta_{ij,ax} + h_j},$$

where $\delta_{ij,ax}$ is the axial distance between the observed coils. Referring to the six coil transformer, the coil pairs are obtained for: $i = 1, 2$ and $j = 3, 4, 5, 6$; and for $i = 3, 4$ and $j = 5$,

6. Detailed expressions for calculating the radial inductance component, referring to the geometry shown in Figure 35 are:

$\sigma^r_{R,13} = \dfrac{\pi a_2}{h_2 + \delta_{11,ax} + h_2}$	$\sigma^r_{R,14} = \dfrac{\pi(a_1 + a_2)/2}{h_2 + \delta_{11,ax} + h_1}$
$\sigma^r_{R,15} = \dfrac{\pi a_2}{h_2 + 2\delta_{11,ax} + h_2 + h_2}$	$\sigma^r_{R,16} = \dfrac{\pi(a_1 + a_2)/2}{h_2 + 2\delta_{11,ax} + h_2 + h_1}$
$\sigma^r_{R,24} = \dfrac{\pi a_1}{h_1 + \delta_{11,ax} + h_1}$	$\sigma^r_{R,26} = \dfrac{\pi a_1}{h_1 + 2\delta_{11,ax} + h_1 + h_1}$
$\sigma^r_{R,23} = \sigma^r_{R,14}$	$\sigma^r_{R,25} = \sigma^r_{R,16}$
$\sigma^r_{R,35} = \sigma^r_{R,13}$	$\sigma^r_{R,36} = \sigma^r_{R,14}$
$\sigma^r_{R,45} = \sigma^r_{R,23}$	$\sigma^r_{R,46} = \sigma^r_{R,24}$

$L^r_{13} = \dfrac{\mu_o \pi N_o^2 D_{2,AV} K^r_{R,13}}{a_2}\left(\dfrac{a_2}{3} + \dfrac{a_2}{3}\right)$	$L^r_{14} = \dfrac{\mu_o \pi N_o^2 D_{12,AV} K^r_{R,14}}{(a_1 + a_2)/2}\left(\dfrac{a_2}{3} + \delta_{12} + \dfrac{a_1}{3}\right)$
$L^r_{15} = \dfrac{\mu_o \pi N_o^2 D_{2,AV} K^r_{R,15}}{a_2}\left(\dfrac{a_2}{3} + \dfrac{a_2}{3}\right)$	$L^r_{16} = \dfrac{\mu_o \pi N_o^2 D_{12,AV} K^r_{R,16}}{(a_1 + a_2)/2}\left(\dfrac{a_2}{3} + \delta_{12} + \dfrac{a_1}{3}\right)$
$L^r_{24} = \dfrac{\mu_o \pi N_o^2 D_{1,AV} K^r_{R,24}}{a_1}\left(\dfrac{a_1}{3} + \dfrac{a_1}{3}\right)$	$L^r_{26} = \dfrac{\mu_o \pi N_o^2 D_{1,AV} K^r_{R,26}}{a_1}\left(\dfrac{a_1}{3} + \dfrac{a_1}{3}\right)$

Using the previous expressions, following results are obtained:

$\sigma^r_{R,13}$	$\sigma^r_{R,14}$	$\sigma^r_{R,15}$	$\sigma^r_{R,16}$	$\sigma^r_{R,24}$	$\sigma^r_{R,26}$
0.326089	0.314159	0.214675	0.206821	0.302229	0.198967
$K^r_{R,13}$	$K^r_{R,14}$	$K^r_{R,15}$	$K^r_{R,16}$	$K^r_{R,24}$	$K^r_{R,26}$
0.146678	0.141845	0.10005	0.096635	0.136975	0.093201
L^r_{13} [μH]	L^r_{14} [μH]	L^r_{15} [μH]	L^r_{16} [μH]	L^r_{24} [μH]	L^r_{26} [μH]
77.826	143.182	53.086	95.186	103.410	70.423

Finally, the binary short-circuit inductances, calculated as $L_{ij} = \sqrt{\left(L^z_{ij}\right)^2 + \left(L^r_{ij}\right)^2}$ are:

L_{12} [µH]	L_{13} [µH]	L_{14} [µH]	L_{15} [µH]	L_{16} [µH]	L_{23} [µH]	L_{24} [µH]	L_{25} [µH]	L_{26} [µH]
173.83	77.83	225.21	53.09	198.19	225.21	103.50	198.19	70.42
L_{34} [µH]	L_{35} [µH]	L_{36} [µH]	L_{45} [µH]	L_{46} [µH]	L_{56} [µH]			
173.83	77.83	225.21	225.21	103.50	173.83			

3. Following the same reasoning as in the case of four winding transformer, additional copper losses are taken into account by the coefficients k_a whose expressions for the high and low voltage coils are:

$$K_{a,HV,i} = \varphi_a(\xi_{HV}) + \frac{(N_{l,HV})^2 - 1}{3} \psi_a(\xi_{HV}), \ \ i = 2,4,6.$$

$$K_{a,LV,i} = \varphi_a(\xi_{LV}) + \frac{(N_{l,LV} \cdot N_{rad})^2 - 1}{3} \psi_a(\xi_{LV}), \ \ i = 1,3,5.$$

where $N_{l,LV}$ is the number of conductor layers in the low voltage coil, N_{rad} is the number of elementary conductors placed radially; the auxiliary variable ξ and the auxiliary functions $\varphi_a(\xi)$ and $\psi_a(\xi)$ are calculated in the same way as previously.

When all the six windings operate in load condition, the leakage field generated by all the windings produces skin effect and additional losses correspondingly in all the windings. A precise and rigorous analytical approach for calculating the binary short-circuit resistances in this case is not known in the relevant literature. Therefore, the six-coil disposition can be considered as axial stacked disposition of three two-winding systems which are roughly equally loaded. The leakage field in this case should be the same as the one generated by a two-winding disposition, repeated axially and the winding ac resistances can be simply estimated as:

$$R_{1,ac} = R_{3,ac} = R_{5,ac} = K_{a,LV} R_{\Omega,LV}$$

$$R_{2,ac} = R_{4,ac} = R_{6,ac} = K_{a,HV} R_{\Omega,HV}$$

The expressions for binary short-circuit resistances are:

$$R_{ij} = K_{ai} R_{i\Omega} + K_{aj} R_{j\Omega}$$

$$R_{13} = R_{15} = R_{35}; \quad R_{24} = R_{26} = R_{46};$$

$$R_{12} = R_{14} = R_{16} = R_{23} = R_{25} = R_{34} = R_{36} = R_{45} = R_{56}.$$

	LV coil	HV coil
Ohmic resistance R [mΩ] $i=1,3,5$; $j=2,4,6$.	$R_{i,\Omega} = 3.123$	$R'_{j,\Omega} = 4.993$
Auxiliary coefficient ξ	0.495112	0.182699
Auxiliary function $\varphi_a(\xi)$	1.005329	1.000099
Auxiliary function $\psi_a(\xi)$	0.019982	0.000371
Additional loss coefficient		
K_a	1.238451	1.027828

R_{12} [mΩ]	R_{13} [mΩ]	R_{14} [mΩ]	R_{15} [mΩ]	R_{16} [mΩ]	R_{23} [mΩ]	R_{24} [mΩ]	R_{25} [mΩ]	R_{26} [mΩ]
8.999	7.735	8.999	7.735	8.999	8.999	10.263	8.999	10.263
R_{34} [mΩ]	R_{35} [mΩ]	R_{36} [mΩ]	R_{45} [mΩ]	R_{46} [mΩ]	R_{56} [mΩ]			
8.999	7.735	8.999	8.999	10.263	8.999			

Using the previous values, we can calculate binary short-circuit impedance between coils i and j as:

$$\overline{Z_{sc,ij}} = R_{ij} + j\omega L_{ij} \ .$$

In order to obtain mesh network branch impedances from these binary short-circuit impedances, it is convenient to repeat the form of the Z matrix:

$$\overline{Z} = \begin{bmatrix} a_{22} & a_{23} & a_{24} & a_{25} & a_{26} \\ a_{23} & a_{33} & a_{34} & a_{35} & a_{36} \\ a_{24} & a_{34} & a_{44} & a_{45} & a_{46} \\ a_{25} & a_{35} & a_{45} & a_{55} & a_{56} \\ a_{26} & a_{36} & a_{46} & a_{56} & a_{66} \end{bmatrix},$$

where $a_{ii} = \overline{Z_{sc,1i}}$ and $a_{ij} = \frac{1}{2}\left(\overline{Z_{sc,1i}} + \overline{Z_{sc,1j}} - \overline{Z_{sc,ij}}\right)$, or the complete expressions:

$a_{22} = \overline{Z_{sc,12}}$; $a_{33} = \overline{Z_{sc,13}}$; $a_{44} = \overline{Z_{sc,14}}$; $a_{55} = \overline{Z_{sc,15}}$; $a_{66} = \overline{Z_{sc,16}}$	
$a_{23} = \frac{1}{2}\left(\overline{Z_{sc,12}} + \overline{Z_{sc,13}} - \overline{Z_{sc,23}}\right)$	$a_{24} = \frac{1}{2}\left(\overline{Z_{sc,12}} + \overline{Z_{sc,14}} - \overline{Z_{sc,24}}\right)$
$a_{25} = \frac{1}{2}\left(\overline{Z_{sc,12}} + \overline{Z_{sc,15}} - \overline{Z_{sc,25}}\right)$	$a_{26} = \frac{1}{2}\left(\overline{Z_{sc,12}} + \overline{Z_{sc,16}} - \overline{Z_{sc,26}}\right)$
$a_{34} = \frac{1}{2}\left(\overline{Z_{sc,13}} + \overline{Z_{sc,14}} - \overline{Z_{sc,34}}\right)$	$a_{35} = \frac{1}{2}\left(\overline{Z_{sc,13}} + \overline{Z_{sc,15}} - \overline{Z_{sc,35}}\right)$

$a_{36} = \dfrac{1}{2}\left(\overline{Z_{sc,13}} + \overline{Z_{sc,16}} - \overline{Z_{sc,36}}\right)$	$a_{45} = \dfrac{1}{2}\left(\overline{Z_{sc,14}} + \overline{Z_{sc,15}} - \overline{Z_{sc,45}}\right)$
$a_{46} = \dfrac{1}{2}\left(\overline{Z_{sc,14}} + \overline{Z_{sc,16}} - \overline{Z_{sc,46}}\right)$	$a_{56} = \dfrac{1}{2}\left(\overline{Z_{sc,15}} + \overline{Z_{sc,16}} - \overline{Z_{sc,56}}\right)$

By inverting this matrix *Z*, we obtain the branch admittance matrix *Y*:

$$\overline{Y} = \left[\overline{Z}\right]^{-1} = \begin{bmatrix} b_{22} & b_{23} & b_{24} & b_{25} & b_{26} \\ b_{23} & b_{33} & b_{34} & b_{35} & b_{36} \\ b_{24} & b_{34} & b_{44} & b_{45} & b_{46} \\ b_{25} & b_{35} & b_{45} & b_{55} & b_{56} \\ b_{26} & b_{36} & b_{46} & b_{56} & b_{66} \end{bmatrix},$$

where $\overline{Z_{ij}} = -\dfrac{1}{b_{ij}}$, for $i \neq 1$, $j \neq 1$; and $\overline{Z_{1i}} = \dfrac{1}{b_{ii} + \displaystyle\sum_{\substack{j \neq 1, j \neq i, \\ i \neq 1}} b_{ij}}$, or in details:

$\overline{Z_{23}} = -\dfrac{1}{b_{23}}$; $\overline{Z_{24}} = -\dfrac{1}{b_{24}}$	$\overline{Z_{25}} = -\dfrac{1}{b_{25}}$; $\overline{Z_{26}} = -\dfrac{1}{b_{26}}$
$\overline{Z_{34}} = -\dfrac{1}{b_{34}}$; $\overline{Z_{35}} = -\dfrac{1}{b_{35}}$; $\overline{Z_{36}} = -\dfrac{1}{b_{36}}$	$\overline{Z_{45}} = -\dfrac{1}{b_{45}}$; $\overline{Z_{56}} = -\dfrac{1}{b_{56}}$
$\overline{Z_{12}} = \dfrac{1}{b_{22} + b_{23} + b_{24} + b_{25} + b_{26}}$	$\overline{Z_{13}} = \dfrac{1}{b_{33} + b_{23} + b_{31} + b_{35} + b_{36}}$
$\overline{Z_{14}} = \dfrac{1}{b_{44} + b_{24} + b_{34} + b_{45} + b_{46}}$	$\overline{Z_{15}} = \dfrac{1}{b_{55} + b_{25} + b_{35} + b_{45} + b_{56}}$
$\overline{Z_{16}} = \dfrac{1}{b_{66} + b_{26} + b_{36} + b_{46} + b_{56}}$	

Appendix 5: Transformer temperature profile

Description	Formula	4 coils transformer		6 coils transformer		Unit
		LV	HV	LV	HV	
Average copper temperature rise over the winding external surface (typically this value is very small, lower than 2°C)	$\Delta\theta_1 = 0.119 \cdot q \cdot g^2 \cdot N_{lay}\dfrac{\delta_{is}}{2}$ q-bare conductor width δ_{is}-interlayer isolation g-current density N_{lay}-total number of insulation layers	1.6	1.9	0.43 0.43 0.43	0.81 0.81 0.81	°C
Cooling surface (oil convection)	$S_{conv} = 3 \cdot N\pi \cdot D_{av} \cdot h_{el}$ N-number of cooling surfaces. In case of axial duct, N=4 D_{av} – coil average diameter	1.29 1.54 1.80	4.37	2.13 2.13 2.13	2.14 2.14 2.14	m²
Oil convection coefficient	α = 60 - 80	75 60 70	70	70 60 70	70 60 70	W/(m²C)
Surface curvature coefficient	$k = 0.75 - 0.85$	0.75	0.85	0.8 0.75 0.8	0.8 0.75 0.8	
Temperature rise of the winding external surface over oil temperature	$\Delta\theta_2 = \dfrac{P_{Cu}}{k \cdot S_{conv} \cdot \alpha}$	18.76 23.1 18.04	20.1	21.83 27.16 21.83	21.90 27.26 21.90	°C
Winding total temperature rise over oil temperature $\Delta\theta_{Cu-oil} \leq 20^o C$	$\Delta\theta_{Cu-oil} = \Delta\theta_1 + \Delta\theta_2$	19 24 19	22	23 28 23	23 29 23	°C
Average oil temperature rise over transformer tank temperature	$\Delta\theta_3 = 3 - 5$	3	3	3	3	°C
Transformer tank convection coefficient	$\alpha_{conv} = 7 - 8$	7.5		7		W/(m²C)
Transformer tank radiation coefficient	$\alpha_{rad} = 6 - 7$	6.5		6		W/(m²C)
Transformer tank convection surface*	$S_{conv,t}$	43.087		31.242		m²
Transformer tank radiation surface	S_{rad}	8.960		8.068		m²
Transformer tank temperature rise over the ambient temperature	$\Delta\theta_4 = \dfrac{P_{tot}}{\alpha_{conv}S_{conv,t} + \alpha_{rad}S_{rad}}$	37		30		°C

Transformer oil total temperature rise over the ambient temperature	$\Delta\theta_{oil-amb} = \Delta\theta_3 + \Delta\theta_4$	40	33	°C
Transformer oil maximum temperature rise over the ambient temperature $\Delta\theta_{oil-amb,\max} \leq 60^o C$	$\Delta\theta_{oil-amb,\max} = \dfrac{\Delta\theta_{oil-amb}}{0.85}$	48	39	°C
Copper total temperature rise over the ambient temperature $\Delta\theta_{Cu-amb} \leq 65^o C$	$\Delta\theta_{Cu-amb} = \Delta\theta_{Cu-oil} + \Delta\theta_3 + \Delta\theta_4$	62	62	°C
Average ambient temperature	$\theta_a = 22^oC$	22	22	°C
Copper maximum temperature**	$\Delta\theta_{Cu,\max} = \theta_a + \Delta\theta_{Cu-amb}$	102	102	°C
Maximum oil temperature**	$\Delta\theta_{oil,\max} = \theta_a + \Delta\theta_{oil-amb,\max}$	88	79	°C

*In order to calculate tank surfaces which dissipate the heat, it is necessary to perform a brief tank design which is given as follows.
** Considering maximum ambient temperature of 40°C.

Description	Formula	4 coils	6 coils	Unit
Distance HV winding – tank in length	$n_2 \geq 30$	51.5	53.5	mm
Distance HV winding – tank in width	$n_1 \geq 50$ mm	91.5	89.5	mm
Distance yoke – tank bottom	$h_b \geq 40$ mm	40	40	mm
Distance yoke - tank top	$h_t \geq 150$ mm	200	200	mm
Transformer tank length	$A_t = 3D_{4,EXT} + 2\delta_{11} + 2n_1$	1,540	1,210	mm
Transformer tank width	$B_t = D_{4,EXT} + n_1 + n_2$	610	500	mm
Transformer tank height	$C_t = H_c + h_b + h_t$	1,055	1,260	mm
Recommended distance between tank bottom and rib	$h_{bot-rib} = h_b + A_1 + v_2$	300	455	mm
Adopted distance between tank bottom and rib	$h_{bot-rib}$	205	320	mm
Recommended distance between tank top and rib	$h_{top-rib} \approx 40-50$	40	40	mm
Transformer ribs height	$C_r = C_t - h_{bot-rib} - h_{top-rib}$	810	900	mm
Transformer ribs width (depends on the tank mechanical elasticity, which should be checked later on)	$B_r \geq 100$	200	170	mm
Distances on the tank side not covered with ribs	$a_n = 50-120; \ b_n = 50-120$	50; 40	80; 50	mm
Distance between two ribs axes	$a_r = 35-50$	35	35	mm

| Number of ribs on the longer side	$N_A = \dfrac{A_t - 2a_n}{a_r} + 1$	42	31	
Number of ribs on the shorter side	$N_B = \dfrac{B_t - 2b_n}{a_r} + 1$	16	12	
Ribs width	$d_r = 6 - 7$	6	6	mm
Transformer cover surface	$S_{top} = 0.75(A_t - 0.01)\cdot(B_t - 0.01)$	0.689	0.441	m²
Transformer longer side surface	$S_{1,t} = A_t \cdot C_t \cdot 10^{-6}$	1.625	1.525	m²
Transformer shorter side surface	$S_{2,t} = B_t \cdot C_t \cdot 10^{-6}$	0.644	0.167	m²
Total transformer free surface (without ribs) Note: these equations are valid when all the four transformer sides have ribs	$S_{free} = 2(S_{1,t} - N_A C_r d_r) +$ $2(S_{2,t} - N_B C_r d_r)$	3.973	3.845	m²
Total ribs surface	$S_{ribs} = [2B_r(C_r + d_r) + C_r d_r]\cdot$ $(N_A + N_B)\cdot 10^{-6}$	38.43	26.96	m²
Perimeter calculation	$L_a = (N_A - 1)a_r 10^{-3}$ $L_b = (N_B - 1)a_r 10^{-3}$ $L = 10^{-3}\sqrt{(B_r + a_n)^2 + (B_r + b_n)^2}$	1.435 0.525 0.347	1.05 0.385 0.333	m
Surface of the transformer ribs equivalent	$S_{r,eq} = [2(L_a + 2L_b) + 4L]\cdot C_r 10^{-3}$	4.30	3.78	m²
Total surface for cooling through convection	$S_{conv,t} = S_{top} + S_{free} + S_{ribs}$	43.087	31.242	m²
Total surface for cooling through radiation	$S_{rad} = S_{top} + S_{free} + S_{r,eq}$	8.960	8.068	m²
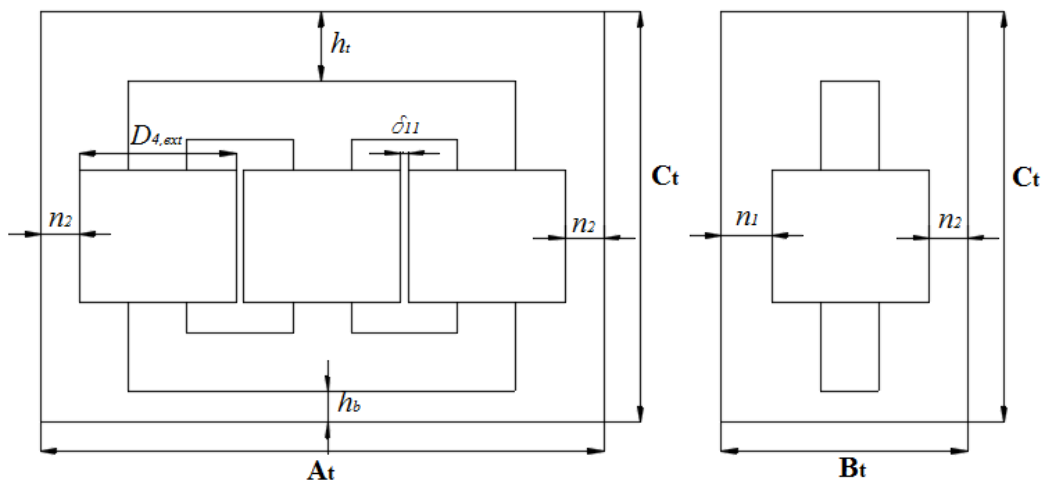
Figure 61 Transformer tank cross section

References

[1] Vecchio R.M., Poulin B., Feghali P.T., Shah D.M., Ahuja R., *Transformer Design Principles, with applications to core-form power transformers*, 2nd Ed., CRC Press, 2010.

[2] Jeszenszky, S., History of transformers, *IEEE Power Engineering Review*, December 1996, pp. 9-12.

[3] Baehr R., Transformer Technology State-of-the-Art and Trend of Future Development, *Electra*, No. 198, October, 2001, pp. 13-19.

[4] Kulkarni S.V., Khaparde S.A., *Transformer engineering: Design and Practice*; Marcel Dekker, Inc., 2004.

[5] Gupta A., Bais A.S., Global Transformer Market Share – Industry Forecast Report 2018-2024, *Global Marker Insights*, September 2018.

[6] Fitzgerald, A.E., Kingsley Jr. Ch., Umans D.S., *Electric Machinery*, 6th Ed, McGraw-Hill Hill, 2003.

[7] Irving M., Gottlieb P.E., *Practical Transformer Handbook*, 1st Ed., Newnes, Elsevier, 1998.

[8] Piotrovsky L. M., *Electrical machines*, 7th Ed., Energy, 1974 (in Russian)

[9] Kaliħ Ћ., Radosavljeviħ R., *Transformers*, 2nd Ed., Institutes for textbooks and didactic materials, Belgrade, 2001 (in Serbian).

[10] Harlow H. James, *Electric Power Transformer Engineering*, CRC Press LLC, 2004.

[11] Winders J. J. Jr., *Power Transformers: Principles and Applications*, Marcel Dekker, Inc., 2002.

[12] Hurley W.G., Wolfle W.H., *Transformers and Inductors for Power Electronics: Theory, Design and Applications*, John Wiley & Sons, Ltd., 2013.

[13] Majkovic Z., Damir Z., *Basic Transformer Theory*, Presentation on the course of Theory of Electrical Machines and Transformers at the Faculty of Electrotechnics and Information FER, Zagreb, Croatia, September, 2014 (in Croatian).

[14] Blume L. F., et. all., *Transformer Engineering: A Treatise on the Theory, Operation, and Application of Transformers*, 2nd Ed., John Wiley & Sons, Inc., 1951.

[15] Aicher L.C., A Useful Equivalent Circuit for a Five-Winding Transformer, *Transactions of the American Institute of Electrical Engineers*, Vol. 62, Issue 2, Feb. 1943, pp. 66-70.

[16] IEC 60076-8: *Power Transformers – Part 8: Application Guide*, Ed. 1, 1997.

[17] Shaarbafi K., *Transformer Modelling Guide*, Teshmont Consultants LP, Alberta, July, 2014.

[18] Hayek J. E., *Parameters Analysis of Multi-Winding Traction Transformers*, PhD thesis, University of Applied Sciences and Arts Western Switzerland, March, 2016.

[19] Rosa J., Calculation of Flux Linkages in Multiwinding transformers, *17th Annual IEEE Power Electronics Specialists conference*, 1986, pp. 639-644.

[20] Azizian D., Valilian M., Faiz J., A New Multi-Winding Traction Transformer Equivalent Circuit for Short-Circuit Performance Analysis, *International Transactions on Electrical Energy Systems*, John Wiley & Sons, Ltd., 2012, pp. 186-202.

[21] Esfandiari E., Mariun N.B., Multi-Winding Transformer Based Diode-Clamped Multi-Level Inverter, *IEEE Symposium on Industrial Electronics and Applications*, 2010, pp. 155-158.

[22] Daher S., Schmid J., Antunes L.M., Multilivel Inverter Topologies for Stand-Alone PV Systems, *IEEE Transactions on Industrial Electronics*, Vol. 55, No. 7, July 2008, pp. 2703-2712.

[23] Okyere P.K.F., A Multi-Winding Transformer Model for Predictive SMPS Design and Analysis, *IEEE 7th International Conference on Power Electronics*, October, 2007, pp. 1021-1026.

[24] Krishnamoorthy H.S., Enjeti P.N., Pitel I.J., Hawke J.T., New Medium-Voltage Adjustable Speed Drive Topologies with Medium-Frequency Transformer Isolation, *IEEE 7th International Power Electronics and Motion Control Conference*, June, 2012, pp. 814-819.

[25] *European Patent: Electric Vehicle Charging Station with Transformer Comprising Multiple Secondary Windings*, EP 3339084A1, Bul. 26/2018, June, 2018.

[26] Deutsches Windenergie – Institut GmbH, *Wind Turbine Grid Connection and Interaction*, 2001.

[27] Dericioglu C., et. all., A Review of Charging Technologies for Commercial Electric Vehicles, *International Journal of Advances on Automotive and Technology*, Vol. 2, No. 1, January 2018, pp. 61-70.

[28] Yilmaz M., Krein P. T., Review of Battery Charger Topologies, Charging Power Level, and Infrastructure for Plug-In Electric and Hybrid Vehicles, *IEEE Transactions on Power Electronics*, Vol. 28, No. 5, May 2013, pp. 2151-2169.

[29] Habib S., abbas F., Khan M. M., Assessment of Electric Vehicles Concerning Impacts, Charging Infrastructure with Unidirectional and Bidirectional Chargers, and Power Flow Comparison, *International Journal of Energy Research*, 2018, pp. 1-26.

[30] Mi C., Masrur M. A., Gao D. W., *Hybrid Electric Vehicles: Principles and Applications with Practical Perspectives*, John Wiley & Sons, Ltd, 2011.

[31] *SAE J1772_201001: Electric Vehicle and Plug in Hybrid Electric Vehicle Conductive Charge Coupler Standard*, 2010.

[32] *CHAdeMO announces 150kW protocol*, published on 01.06.2016, accessed on 06.08.2019, available at https://www.chademo.com/chademo-announces-150kw-protocol/

[33] *CHAdeMO Association and Protocol*, April 2019, accessed on 06.08.2019, available at https://www.chademo.com/wp2016/wp-content/uploads/2019/06/2019%20CHAdeMO_Brochure_web_corrected%2025%20June.pdf

[34] *CHAdeMO High Power Roadmap*, accessed on 29.07.2019, available on https://www.chademo.com/technology/high-power/ ,

[35] Dsumez S., Cook A., Khaligh A., Comprehensive Analysis of High Quality Power Converters for Level 3 Off-Board Chargers, *2011 IEEE Vehicle Power and Propulsion Conference*, Chicago, USA, September 2011.

[36] Compliance Testing to the IEC 1000-3-2 (EN 61000-3-2) and IEC 1000-3-3 (EN 6100-3-3) Standard – Application Note, *Agilent Technologies*, 2000.

[37] *IEEE Recommended Practices and Requirements for Harmonic Control in Electrical Power Systems*, IEEE Std. 519-1992, April 1993.

[38] Tao H., Zhang G., Zheng Z., Onboard Charging dc/dc Converter of Electric Vehicle Based on Synchronous Rectification and Characteristic Analysis, *Hindawi Journal of Advanced Transportation*, Vol. 2019, June 2019.

[39] Blaabjerg F., *Control of Power Electronic Converters and Systems*, Vol. 2, Elsevier Inc, 2018.

[40] Il-Oun L., Jun-Young L., A High-Power dc-dc Converter Topology for Battery Charging Applications, *Energies* 2017, Vol. 10, 871, June 2017.

[41] Chen M., Rincon-Mora G. A., Accurate Electrical Battery Model Capable of Predicting Runtime and I-V Performance, *IEEE Transactions on Energy Conversion*, Vol. 21, No. 2, June 2006, pp. 504-511.

[42] Rachid A., Fadil H. E., Giri F., Dual Stage CC-CV Charge Method for Controlling DC-DC Power Converter in BEV Charger, *19th IEEE Mediterranean Electrotechnical Conference*, Marrakech, 2018, pp. 74-79.

[43] Wirtz J., On-Board vs. Off Board Charging, Eaton Corporation, *Electrical Transportation Infrastructure*, 2011.

[44] Mohan N., Undeland T. M., Robbins W. P., Power *Electronics: Converters, Applications and Design*, 2nd Ed., John Wiley & Sons, Inc., New York, 1995.

[45] Chakraborty S., et. all., DC-DC Converter Topologies for Electric Vehicles, Plug-in Hybrid Electric Vehicles and Fast Charging Stations: State of the Art and Future Trends, *Energies* 2019, Vol. 12, 1569, April 2019, pp. 1-43.

[46] Manias S. N., *Power Electronics and Motor Drive Systems*, Elsevier Inc., 2017.

[47] Williams B. W., *Principles and Elements of Power Electronics: Devices, Drivers, Applications and Passive Components*, Barry W Williams, 2006.

[48] Bhat A. H., Agarwal P., A Comparative Evaluation of Three-Phase High Power Factor Boost Converters for Power Quality Improvement*, 2006 IEEE International Conference on Industrial Technology*, Mumbai, India, December 2006, pp. 546-551.

[49] Vilela S. D. M., et. all., Proposal of a Hysteresis Control Technique with Almost Constant Frequency Applied to the Three Phase Boost converter, *2003 IEEE International Symposium on Industrial Electronics*, Rio de Janeiro, Brazil, June 2003, pp. 980-987.

[50] Brenna M., Foiadelli F., Zaninelli D., *Electrical Railway Transportation Systems*, IEEE Pres, John Wiley & Sons, Inc., New Jersey, USA, 2018.

[51] *IEC 60076-1: Power Transformers – Part 1: General*, Ed. 2.1, 2000.

[52] Di Gerlando A., ElShawarby K., Foglia G. M., Perini R., Desing and Modeling of Multi-Winding Transformers Interfacing Inverters and Mains, *IEEE XIII International Conference on Electrical Machines*, 2018, pp. 656-661.

[53] Luo M., Dujic D., Allmeling J., Leakage Flux Modeling of Multiwinding Transformers for System-Level Simulations, *IEEE Transactions on Power Electronics*, Vol. 33, No. 3, March 2018, pp. 2471-2483.

[54] Tsili M. A., Amoralis E. I., Kladas A. G., Souflaris A. T., Optimal Design of Multi-Winding Transformer Using Combined FEM, Taguchi and Stochastic-Deterministic Approach, *IET Electric Power Applications*, Vol. 6, Iss. 7, April 2012, pp. 437-454.

[55] Dasgupta I., *Design of Transformers*, McGraw Hill Education (India), 2015.

[56] Krstović J., Radosavljević R., *Design of Distribution Transformers*, Akademska misao, Belgrade, 2009 (in Serbian).

[57] Mittle V. N., Mittal A., *Design of Electrical Machines*, N. C. Jain Standard Publishers Distributors, Delhi, 1998.

[58] Petroviħ V., *Manual to Transformer Design*, Gradjevinska knjiga, Belgrade, 1975 (in Serbian).

[59] Tihomirov P. M., *Transformer Design*, Energy, Moscow, 1976 (in Russian)

[60] Georkilakis P. S., *Spotlight on Modern Transformer Design*, Springer, 2009.

[61] *Enamelled Copper Wires Catalogue*, Hellenic Cables S.A., Greece.

[62] *Enamelled Winding Wires Catalogue*, Bemka, Istanbul, Turkey.

[63] *Tran-Cor H: Grain Oriented Electrical Steels*, AK Steel, Product Data Bulletin, Netherlands, 2013.

[64] Saravia E., Chaves M. L. R., Camacho J. R., Adjustments for a Three-Phase Distribution Transformer Two-Dimensional Representation with Finite Element Method, *Simposio Brasiliero de Sistemas Eletricos SBSE 2010* Conference paper, Brazil, May 2010.

[65] Azizian D., Vakilian M., Faiz J., Bigdeli M., Calculating Leakage Inductances of Split-Windings in Dry-Type Traction Transformers, *ECTI Transactions on Electrical Engineering, Electronics, and Communication*, Vol. 10, No. 1, February, 2012, pp. 99-106.

[66] Yang Z., Li S., Nan W., Zha X., High Frequency Harmonic Analysis and Suppression of Converters Paralleled by Multiwinding Transformer, *IEEE 2014 International Power Electronics and Application Conference and Exposition*, November 2014, Shanghai, China.

[67] Holmes D. G., McGrath B. P., Opportunities for Harmonic Cancellation with Carrier-Based PWM for Two-Level and Multilevel Cascaded Inverters, *IEEE Transactions on Industry Applications*, Vol. 37, Iss. 2, April 2001, pp. 574-582.

[68] Cao Y. I., Juang Y. H., Tang Z., Tan W., Research on Different Carrier Phase-Shifted Angle with Output Voltage Performance of Cascade Multilevel Inverter, *IEEE 6th International Power Electronics and Motion Control Conference*, May, 2009.

[69] Lammeraner J., Stafl M., *Eddy Currents*, Iliffe Books Ltd., 1966.

[70] *IEC Std. 60076-7:2005: Loading Guide for Oil-Immersed Power Transformers*, 2005.

[71] Najdenkoski K., Manov D., Transformer temperature model for determining its life-expectancy, *Proceedings of the 3rd Cigre Macedonia Conference*, Ohrid, 2001 (in Macedonian).

[72] Lachman M. F., Griffin P. J., Walter W., Wilson A., Real-Time Dynamic Loading and Thermal Diagnostics of Power Transformers, *IEEE Transactions on Power Delivery*, Vol. 18, No. 1, January 2003, pp. 142-148.

[73] *IEEE Std. C57.110-1998: IEEE Recommended Practice for Establishing Transformer Capability When Supplying Nonsinusoidal Load Currents*, 1998.

[74] Xie F. X., Huang M., Zhang W. G., Li J., Research on Electric Vehicle Charging Station Load Forecasting, *IEEE 2011 International Conference on Advanced Power System Automation and Protection*, Beijing, China, October 2011, pp. 2055-2060.

[75] Pasaoglu G., et. all., Projections for Electric Vehicle Load Profiles in Europe Based on Travel Survey Data, *JPC Scientific and Policy Reports*, 2013.

[76] Das B., Jalal T. S., McFadden F. S., Comparison and Extension of IEC Thermal Models for Dynamic Rating of Distribution Transformers, *2016 IEEE International Conference on Power System Technology*. Wollongong, Australia, 2016.

[77] Gouda O. E., Amer G. M., Salem W. A. A., Predicting Transformer Temperature Rise and Loss of in the Presence of Harmonic Load Currents, *Ain Shams Engineering Journal*, Ain Shams University, 2012.

[78] Pejovski D., Trajkovski D., Tripunoski Z., Najdenkoski K., Temperature Models for Calculation of Transformer Life at Nonlinear Load Conditions According to IEC and IEEE Standards, *Proceedings of the 10th Cigre Macedonia Conference*, Ohrid, 2017, pp. 1-12 (in Macedonian).

[79] Azizian D., Bigdeli M., Leakage Inductance Calculations in Different Geometries of Traction Transformers, *ECTI Transactions on Electrical Engineering, Electronics, and Communication*, Vol. 12, No. 2, August, 2014, pp. 28-34.